Dosimetry with a fluoroscopic electronic portal imaging device

ERASMUS UNIVERSITEIT ROTTERDAM

Dosimetry with a fluoroscopic electronic portal imaging device

Dosimetrie met een fluorescopisch megavolt afbeeldings systeem

PROEFSCHRIFT

ter verkrijging van de graad van doctor
aan de Erasmus Universiteit Rotterdam
op gezag van de Rector Magnificus
Prof. dr. P.W.C. Akkermans M.A.
en volgens het besluit van het college voor promoties.
De openbare verdediging zal plaatsvinden op
vrijdag 3 september 1999 om 16^{00} uur

door

Kasper Leonard Pasma

geboren te Nijmegen

Promotor:	Prof. dr. P.C. Levendag
Co-promotor:	Dr. B.J.M. Heijmen
Leden leescommissie:	Prof. dr. J.J. Broerse
	Prof. dr. ir. J.J.W. Lagendijk
	Prof. dr. ir. C.J. Snijders

The research descibed in this thesis was performed at the subdivision of Clinical Physics of the Radiotherapy Department at the Daniel den Hoed Cancer Center/University Hospital Rotterdam. This work was financially supported by the Dutch Cancer Society (Grant 94-848).

DUTCH CANCER SOCIETY

© Copyright: chapter 2: 1995 IOP Publishing Ltd
chapter 3: 1998 IOP Publishing Ltd
chapter 4: 1998 American Association of Physicists in Medicine
chapter 5: 1998 Elsevier Science Ireland Ltd
chapter 6: 1999 Elsevier Science Inc.
chapter 7: 1999 American Association of Physicists in Medicine
chapter 8: 1999 American Association of Physicists in Medicine

© K.L. Pasma, Rotterdam, 1999.

Department of Radiation Oncology, Subdivision of Clinical Physics
Daniel den Hoed Cancer Center/University Hospital Rotterdam
Groene Hilledijk 301
3075 EA Rotterdam
The Netherlands

E-mail: pasma@kfih.azr.nl
Phone: +31-10-4391491
Fax: +31-10-4391012

Printed by Ponsen & Looijen, Wageningen

Contents

Chapter 1

Introduction

1.1 Radiotherapy

Soon after the discovery of x-rays by Wilhelm Conrad Röntgen in 1895 [133] it was found that ionizing radiation could be used for the treatment of malignant diseases [53]. Nowadays, radiotherapy is with surgery and chemotherapy one of the three main modalities for treating patients with cancer. The aim of curative radiation therapy is to deliver as high a dose to diseased tissue as needed or as possible without causing unacceptable side effects to the patient. Radiotherapy is applied as teletherapy and as brachytherapy. In brachytherapy dose delivery is performed with radioactive sources that are put within diseased tissue. In teletherapy the treatment usually consists of irradiation of the patient from different directions with high energy photon and/or electron beams, generated with a linear accelerator. Beam directions are chosen such that the radiation damage to critical organs and healthy tissues is minimized. In conformal teletherapy the beams are shaped according to the geometrical projection of the target to further improve conformity of the high dose volume to the tumor volume. To optimize the biological effect of radiotherapy the total dose is usually given in several daily fractions. For very high total doses more than 35 fractions may be delivered.

Research in the last decade has shown that dose distributions can often be significantly improved by applying intensity modulated x-ray beams, calculated by means of inverse treatment planning techniques [15, 19, 20, 75, 76, 138, 166–168]. Using customized beam profiles, the high-dose region can often be conformed more closely to the target volume, reducing dose delivery to healthy tissues. Moreover, for some tumor sites, a more homogeneous dose distribution in the target volume can be obtained.

All (complex) procedures involved in the planning and execution of teletherapy treatments contribute to the overall uncertainty in the dose distributions. Verification is therefore mandatory. Treatment verification while the patient is irradiated can be split into geometrical and dosimetrical verification.

1.2 Geometrical treatment verification

Radiotherapy requires a geometrical representation of the patient anatomy and localization of the tumor, which may be obtained with a simulator, with computed tomography (CT) or with magnetic resonance imaging (MRI). Usually, available CT data are used to design a 3D

treatment plan with a computer treatment planning system (TPS) using individually customized beams. Two separate factors may result in the tumor not being in the desired 3D high dose volume produced by the treatment beams: setup errors and internal organ motion. The risk of these geometrical inaccuracies is underdosage of a part of the tumor and/or overdosage of surrounding tissues and organs.

Ideally, the position of the patient in the treatment beams is in agreement with the position determined in the treatment planning process using the CT data and/or with the position found at the simulator. Films or images acquired with an electronic portal imaging device (EPID, see figure 1.1) may be used to visually check the position of the bony structures relative to the field borders. To access and correct patient setup errors the bony structures visible in the film or EPID image are aligned with the corresponding structures in a simulator image or digitally reconstructed radiograph (DRR), calculated by the TPS using the planning CT data [8, 28–30]. Generally the strategy is to tolerate small random setup errors and to correct systematic setup errors [8], although it is possible to correct for both errors using on-line correction [36, 156]. In the last decade several EPIDs have been developed [34, 106, 151, 160, 164, 171]. Advantages with respect to film are that the digital images are directly available (necessary for on-line verification), that they can be processed to improve image quality and that they may be digitally stored.

In several studies it has been found that organs can move relative to each other significantly [4, 6, 7, 31, 87, 101, 102, 132, 152, 159, 163]. Melian *et al.* found prostate movements of up to 3 cm [101]. Webb describes four solutions to this problem [169]: (i) the use of implanted radio-opaque markers that can be imaged with an EPID using only a single or a few monitor units; the patient position can be adjusted accordingly, (ii) adding margins to the gros tumor volume (GTV) [73], (iii) regulating rectal and bladder filling and (iv) correlating the irradiation with the breathing cycle. Recently, Kroonwijk *et al.* (chapter 5) have demonstrated that for some patients internal prostate motion can be detected without the use of markers by comparing predicted portal dose images (PDIs), i.e. the dose distribution behind the patient in a plane normal to the beam axis, with PDIs measured with an EPID [84]. Off-axis differences between measured and predicted PDIs were caused by frequently occurring gas pockets inside the rectum of the patients during treatment or during acquisition of the planning CT scan. The detected gas pockets did sometimes extend into the GTV area as outlined in the planning CT scans, implying a shift of the anterior rectum wall and prostate in anterior direction. Other approaches for on-line localization of the tumor are the use of an on-line megavoltage CT acquired with an EPID [57, 67, 103, 107], tomotherapy [97] or ultrasound [153].

1.3 Dosimetric treatment verification

1.3.1 Accuracy required in radiotherapy dose delivery

In addition to geometrical precision, the treatment outcome also depends critically on the dose delivered to the target volume and healthy tissues. The relation between the dose and biological effect is described by dose-response curves for the tumor and the critical tissues. A higher dose will result in better tumor control, but the limiting factor is the normal tissue, that is also being irradiated. Often, dose-response curves are steep, therefore a small variation in dose may have a large effect on the probability of complications and on the probability of tumor control. Furthermore, a high dosimetrical accuracy is required to measure these curves

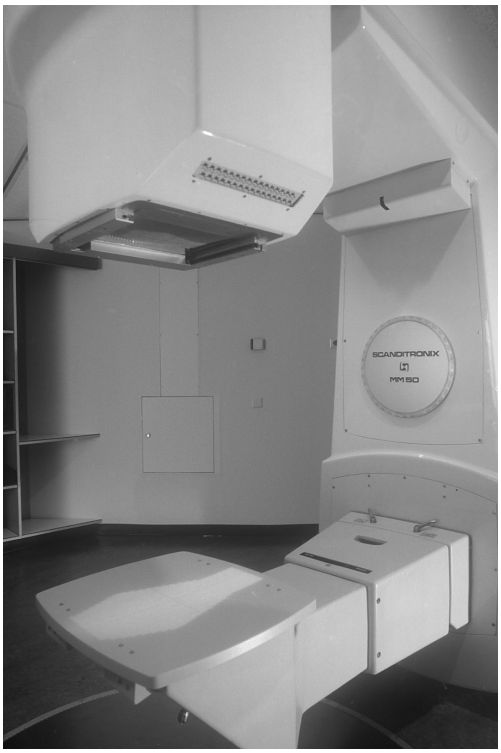

Figure 1.1. The Philips SRI-100 EPID mounted on one of the gantries of the MM50 racetrack microtron at the Daniel den Hoed Cancer Center.

in clinical practice.

Accuracy requirements for the radiation dose delivered to patients in radiotherapy treatments can, in principle, be determined from clinically measured dose response curves. Based on the clinical information available in 1975, an accuracy requirement of $\pm 5\%$ on the delivery of dose to a target volume in a patient, was recommended in ICRU Report 24 [72]. Goitein proposed to consider the 5% dose accuracy as 1.5 standard deviations [54]. Dutreix reports on two experiences at the Institute Gustave Roussy of clinical detection of systematic dosimetric errors [41]. The author emphasizes the need for overall precision in the tumor dose of $\pm 5\%$. Based on radiobiological models Brahme assessed the required accuracy in dose delivery as a function of the parameter γ, the normalized dose gradient of the dose response curve, $\gamma = D \cdot dP/dD$, with D the delivered dose and P the tumor control probability [17, 18]. He concluded that if γ is higher than 3, as is frequently the case in clinical practice, the uncertainty in the mean dose in the target volume should be less than 3% (1 SD) to achieve an absolute standard deviation in tumor control probability of less than 10%; the relative standard deviation in the mean dose in the target volume should be less than 5% when γ is less than 3. Mijnheer *et al.* proposed a requirement for the combined random and systematic uncertainty in the absorbed dose delivery of 3.5% (1 SD) [104]. This requirement is based on the relative

steepness of dose-effect curves for local tumor control and normal tissue damage.

1.3.2 In vivo dosimetry: clinical application and results

The overall accuracy in delivered dose in a radiotherapy treatment can only be assessed directly by means of *in vivo* dosimetry: measurement during treatment. The dose can be measured at the entrance and/or at the exit side of the patient.

Already in 1932 Sievert performed routinely patient dose measurements using small ionization chambers. In the 1960s and 1970s thermoluminescence dosimetry (TLD) was introduced for the determination of absorbed dose in routine therapy [23, 24, 134]. Rudén evaluated the use of TLD for *in vivo* dosimetry at Radiumhemmet. He reports an average deviation between measured entrance dose and prescribed dose of 0.6% for 619 measurements during 1 year in an open 6 MV beam. The spread in the observed deviations was 4.8% (1 SD). Between 10 and 20% of the entrance dose measurements exceeded the action level at Radiumhemmet ($\pm$5% for the open 6 MV beam, $\pm$7% for beams with wedges). The precision of an individual TLD reading was within $\pm$2% (1 SD). A systematic deviation of 4.4 ± 5.0% (1 SD) was found for patients treated with irregularly shaped beams where lead blocks were placed in the beam: too high a correction factor had been used for the attenuation of the radiation in the perspex sheet on which the lead blocks were placed; a change had been made from a thicker to a thinner sheet without giving notice to the planning department. Some severe errors in dose delivery at Radiumhemmet, detected by means of *in vivo* dosimetry, were possible because of the poor interlock system of one of the radiotherapy facilities.

In recent years, encouraged by the work of Rikner *et al.* [56, 128, 129], the use of semiconductor detectors for *in vivo* dosimetry has been investigated [1, 26, 42, 45–48, 68, 70, 86, 90–92, 105, 109, 110, 130]. The main advantage of semiconductor detectors over TLD detectors is the absence of a time delay between patient irradiation and availability of measurement results, allowing an immediate check of all treatment parameters when an error in dose delivery is detected. This eases identification of the sources of the error. Nilsson *et al.* report on entrance dose measurements by means of semiconductor detectors in 1918 treatment fields with high energy x-ray beams, involving 43 patients [109]. Frequency distributions of all measurements of the ratio measured absorbed dose to prescribed absorbed dose show standard deviations of 4.3% (6 MV, open fields), 6.4% (6 MV, wedge fields), 4.6% (21 MV, open fields) and 6.7% (21 MV, wedge fields). The increased standard deviation for wedge fields was attributed to the relatively large influence on detector response of detector positioning errors in wedge fields. The standard deviation for individual patients varied from 1% to almost 9%. Ciocca *et al.* determined midline doses from entrance and exit doses, measured by means of semiconductor detectors, for 38 treatment setups, involving 8 patients with breast cancer [26]. The mean values (in per cent) of the ratios measured absorbed dose to prescribed dose were the following: 96.6 ± 3.8% (N = 33; range: 90-104.2%) at the reference point, 96.8 ± 4.3% (N=48; range: 89.6-106%) at off-axis points in the central plane, 96.8 ± 7.6% (N=18, range: 89.1-112%) in off-axis planes. The systematic deviations between measured and prescribed dose were attributed to an incorrect estimation of the scatter dose contribution by the treatment planning system. These deviations have also been observed in phantom studies [82, 154]. Heukelom *et al.* performed entrance and exit dose measurements, using semiconductor detectors, during irradiation of 14 patients with breast cancer [70]. Measurements were repeated on each patient at least during 4 fractions. The reproducibility of the *in vivo* dose measurements was better than 2% (1 SD).

At the isocenter an average difference between measured and predicted dose of $-2.0 \pm 1.3\%$ was found. For some points behind the lung an average discrepancy of $6.4 \pm 2.5\%$ (1 SD) was found between measured and predicted dose. Positioning of the diodes was checked by means of an EPID. The performance of *in vivo* dosimetry added about 10 minutes to the regular patient irradiation time per fraction. Leunens *et al.* performed entrance dose measurements with semiconductor detectors on patients treated for head and neck and brain tumors [90]. A total number of 554 treatment setups were measured. The mean value of the ratio measured dose to expected dose was $97.8 \pm 2.8\%$. Deviations between measured and predicted dose, larger than 5%, were detected in 3% of the investigated treatment setups. The measurements on patients, treated with pancranial irradiation, proved the superiority with respect to precision in dose delivery of an isocentric technique over a fixed SSD technique. Combined entrance and exit dose measurements were performed with semiconductor detectors on 34 patients, treated for neck and oral cavity malignancies [91]. In this study, results were obtained for 230 treatment setups divided over 83 treatment fields. The mean midline dose-to-prescribed dose ratio was $97.2 \pm 3.0\%$. Underdosages of 5% or more at the midline were detected in 20.4% (47/230) of the measurements. Three important causes, leading to erroneous dose delivery were detected: (i) errors in patient contours, used for dose calculations, (ii) omittance of tissue inhomogeneities in dose calculations, (iii) omittance of scatter defects in dose calculations. Mitine *et al.* performed 261 entrance dose measurements in 34 treatment fields of 10 head and neck cancer patients in order to assess the value of a single *in vivo* dose measurements e.g. during the first treatment session [105]. For 8 of the 34 treatment fields the *in vivo* dose measurements at the first session demonstrated a discrepancy larger than 4% between measured and expected dose. All detected systematic errors (7) in dose delivery could already be identified during the first *in vivo* measurement. Leunens *et al.* performed 920 entrance dose measurements on 105 breast cancer patients [92]. They observed a striking difference in the rate of occurrence of large dose delivery errors between an old and a modern treatment unit. This difference was attributed to the availability at the new unit of a check-and-confirm system and of beam accessory devices in a fixed position in the beam and to a team of radiographers being responsible for the setups, instead of a single radiographer at the old unit. Noel *et al.* derived the target dose using entrance and exit dose measurements [110]. During 5 years, the target dose for 7519 patients was measured and 79 errors were detected, half of them could have induced a variation of over 10% in the dose delivered. Except for one all errors were of human origin.

The results of clinical studies demonstrate the value of *in vivo* dose measurements for quality assurance of radiotherapy treatments. However, these studies have also demonstrated weak points of presently applied equipment (TLD- and semiconductor-detectors) and methods:

i. TLD-detectors have the distinct drawback of an unavoidable time delay between measurement and availability of the measurement result. Consequently, a direct check of treatment parameters, when an error in dose delivery is detected, is not possible.

ii. Many correction factors have to be applied to convert semiconductor readings into dose values [68, 91, 109]. Due to the different behavior of various diodes, even from the same batch, it is necessary to determine the characteristics for each diode individually. Properties of diodes may change with accumulated absorbed dose.

iii. The method, proposed by Rizzotti *et al.* [130], which is generally applied for determination

of midline dose, using entrance and exit dose measurements [26, 70, 91, 130] has a limited accuracy when inhomogeneities are in the treatment fields.

iv. Placing a semiconductor on the skin of a patient leads to an increase in temperature and consequently in a change in sensitivity of the detector. A steady state is reached after 3-4 minutes with an increase in response of about 3% [56, 109].

v. Semiconductor-detectors as well as TLD-detectors act as build-up material and thus increase the skin dose [109, 134]. Nilsson *et al.* observed a skin dose of more than 90% of dose maximum for ^{60}Co, 6 MV and 21 MV beams. Diodes, used for entrance dose measurements, also attenuate the primary beam. This attenuation may still at 5 cm depth give a dose reduction of 5% over an area of 1 cm^2 [109]. Mitine *et al.* found a dose reduction due to the diode of 4% at a depth of 10 cm [105]. For a 6 MV photon beam, Sen *et al.* found an average dose reduction over a depth from d_{max} to 20 cm of 10% [136]. Both the increase in skin dose and the attenuation effect inhibit frequent performance of *in vivo* dose measurements.

vi. Much care has to be taken for the correct positioning of semiconductor detectors, especially when measurements are performed in wedge fields [90, 109]. Nilsson *et al.* observed larger standard deviations for wedge fields than for open fields [109]. The reason for the increased standard deviation is the difficulty in placing the diode in the proper position. The authors demonstrated that a 1.5 cm displacement of the diode in a wedge field may give rise to errors in measured dose of up to 14%, depending on wedge and beam energy.

vii. The treatment time increases due to the time needed to position the diode(s) on the patient. The increase in treatment time per session is reported to be 1-2 minutes if only the entrance dose is measured [88] and at most 10 minutes if both entrance and exit dose are measured [69]. This may be a reason that there are only a few studies with large numbers of patients [1, 86, 110].

viii. In order to determine midline doses, both entrance and exit dose measurements are performed. For a proper interpretation of these measurements a portal image for each treatment field may be needed to determine the actual positions of the detectors in the treatment field and their relative positions [46, 70, 105].

ix. For practical reasons only very limited numbers of detectors are used for simultaneous measurements in different spots of the treatment fields. Often only the entrance dose is measured, with the consequence that the actual tumor dose cannot be verified and that some errors due to the use of incorrect patient data, like patient contour errors, and due to inadequate algorithms in the treatment planning system are not detected. Due to the necessarily small number of detectors, full verification of treatments delivered with dynamic multileaf collimation is not possible.

1.3.3 Dosimetric application of EPIDs

Above mentioned drawbacks and shortcomings of the presently available techniques for *in vivo* dosimetry with TLDs and diodes can be avoided by using EPIDs:

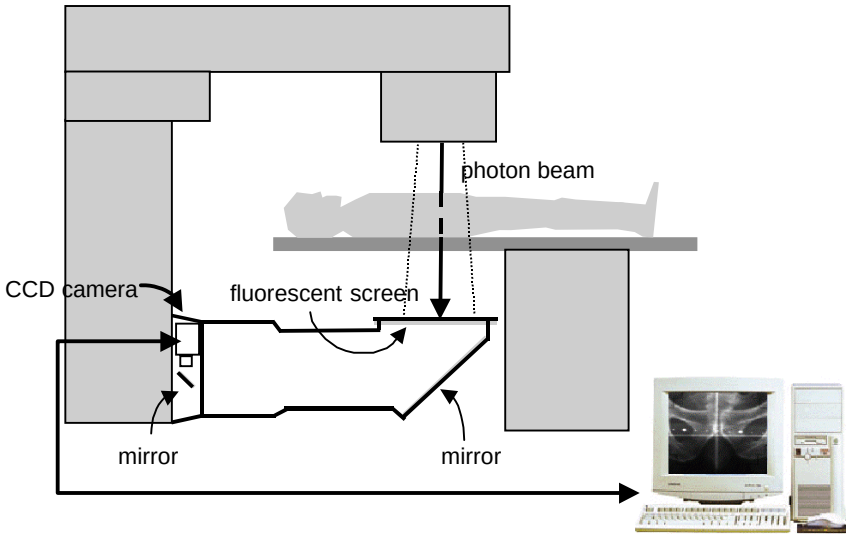

Figure 1.2. Schematic diagram of a fluoroscopic EPID. The detector screen is a stainless steel plate coated with a layer of gadolinium oxysulfide. X-ray photons which hit the detector screen generates visible light in the fluorescent layer, which is viewed by a CCD camera using two mirrors.

i. Dosimetric information is simultaneously obtained over the whole beam area and not only in a single or a few points.

ii. The same detector may be used for verification of patient positioning and of absolute dose delivery. Hence, introduction of patient dose delivery verification does not result in an increase in the regular treatment time per fraction.

iii. Detector positioning is not anymore an issue and dosimetric information can be directly related to patient positioning information.

iv. Physical contact between detector and patient is not needed.

1.4 Objectives of this study

The aim of the study was to develop techniques for dosimetric treatment verification using a fluoroscopic EPID. This type of EPID basically consists of a fluorescent screen, two mirrors and a CCD camera (figure 1.2). The x-ray photons which are not absorbed in the patient and hit the detector screen generate visible light in the fluorescent layer, that is monitored by the CCD camera. The five main objectives were:

i. To investigate the dosimetric characteristics of a fluoroscopic EPID and to develop a method to derive PDIs, from measured EPID images.

ii. To develop methods to predict PDIs, based on the planning CT data of the patient and the irradiation geometry, as determined in the treatment planning process.

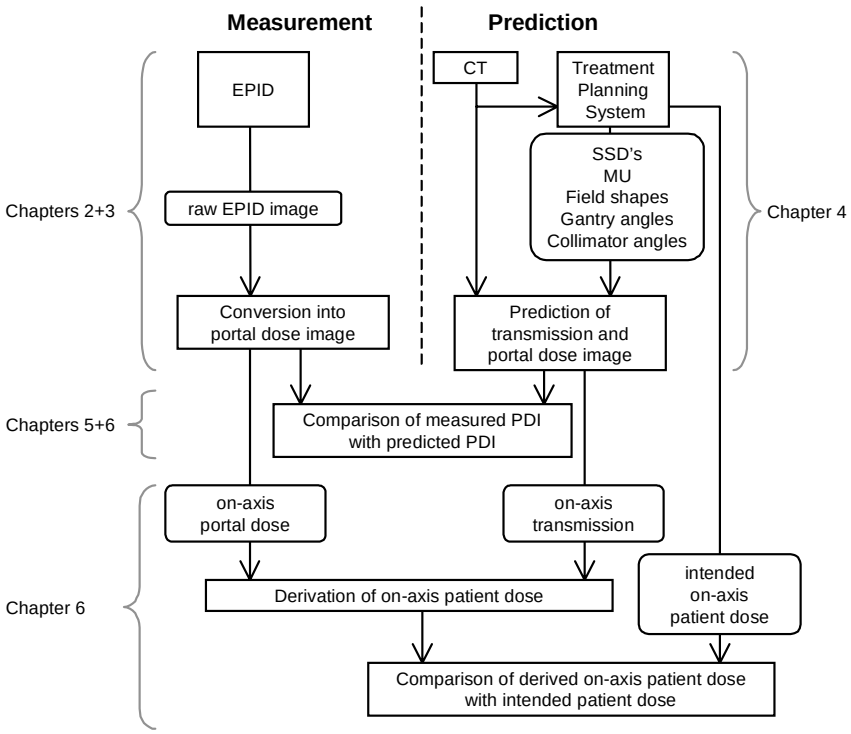

Figure 1.3. Outline of the implemented method for dosimetric treatment verification with an EPID with references to the corresponding chapters. Chapters 7 and 8 are not shown in this flow diagram, in these chapters the use of the EPID for checks of intensity modulated beams produced with compensators and DMLC before patient treatment is demonstrated.

iii. To develop a method for verification of the monitor unit calculation by deriving the on-axis patient dose at a depth of 5 cm from the portal dose measured with the EPID, which is compared with the intended dose derived from the relative dose distribution calculated by the TPS and the isocenter dose prescribed by the radiation oncologist.

iv. To evaluate the developed techniques of comparing predicted and measured PDIs and comparing prescribed and measured patient doses in clinical practice.

v. To develop techniques to verify intensity modulated beams produced with compensators and with dynamic multileaf collimation (DMLC) *before* patient treatment.

Figure 1.3 shows a flow diagram with the implemented method of dosimetric treatment verification with references to the corresponding chapters. In chapter 2 the physical characteristics of the fluoroscopic EPID relevant for dosimetric applications in a 6 MV photon beam are presented. The stability of the system and the response as function of size of the applied x-ray beam and absorber thickness have been investigated. In chapter 3 a method is presented to derive PDIs from measured EPID images. PDI measurements with the EPID are compared with ionization chamber measurements for anthropomorphic phantoms irradiated with open,

wedged and intensity modulated beams produced with dynamic multileaf collimation. In chapter 4 a method for prediction of PDIs in open (non wedged) beams is presented, using the planning CT data of the patient and the irradiation geometry, as determined in the treatment planning process. The first clinical evaluation for 10 prostate cancer patients, of the verification method based on comparing predicted and measured PDIs is presented in chapter 5. These comparisons cannot reveal an error in the MU calculation, since the calculated number of MU is both used for treatment (and thus affects the measured PDI) and for PDI prediction. Therefore an extension to this method is presented in chapter 6 that enables a verification of the MU calculation; the on-axis patient dose at a depth of 5 cm is derived from a portal dose measurement and compared with the intended patient dose, calculated using the relative dose distribution calculated by the TPS and the prescribed isocenter dose. The method was clinically evaluated for a group of 115 prostate cancer patients.

The developed techniques can also be used for checks of intensity modulated beams produced with compensators or dynamic multileaf collimation before patient treatment, as discussed in chapters 7 and 8, respectively. In chapter 9 the developed method for dosimetric treatment verification is evaluated and compared with other methods. Furthermore, the dosimetric characteristics of the fluoroscopic EPID are compared with those of an EPID system consisting of a matrix of liquid filled ionization chambers.

Chapter 2

Portal dose measurement in radiotherapy using an electronic portal imaging device

B.J.M. Heijmen, K.L. Pasma, M. Kroonwijk, V.G.M. Althof, J.C.J. de Boer,
A.G. Visser and H. Huizenga
Phys. Med. Biol. 40(11): 1943-1955, 1995.

Physical characteristics of a commercially available electronic portal imaging device (EPID), relevant to dosimetric applications in high energy photon beams, have been investigated. The EPID basically consists of a fluorescent screen, mirrors and a CCD camera. Image acquisition for portal dose measurement has been performed with a special procedure, written in the command language that comes with the system. The observed day-to-day variation in local EPID responses, i.e. measured grey scale value (EPID signal) per unit of delivered portal dose, is 0.4% (1 SD); day-to-day variations in *relative* EPID responses (e.g. normalised to the on-axis response) are within 0.2% (1 SD). Measured grey scale values are linearly proportional to transmitted portal doses with a proportionality constant which is independent of the thickness of a flat, waterequivalent absorber in the beam, but which does significantly depend on the size of the applied x-ray beam. It is shown that the observed increase in EPID response with increasing field size is mainly due to contributions to the EPID signals from scattered light: Visible photons produced by the x-ray beam in a point of the fluorescent screen do not only generate a grey scale value in the corresponding point of the EPID image, but do also lead (due to scatter from components of the EPID structure onto the CCD chip) to an increased grey scale value in all other points of the image. A point spread function, derived from measured data and describing the increase in EPID response at the beam axis due to off-axis irradiation of the fluorescent screen, has been successfully applied to connect portal doses with grey scale values measured with the EPID.

2.1 Introduction

Several studies on dosimetric applications of EPIDs have been performed: Kirby and Williams have evaluated the possibilities for the assessment of the field flatness of a treatment unit with a Philips SRI-100 EPID [81]. Dirkx *et al.* have, during a long period, indeed used an SRI-100 for daily quality control of the absolute output and field flatness of the 25 MV photon beam of an MM50 racetrack microtron; daily measurements were performed for four different gantry angles[39]. Evans *et al.* [51] and Yin *et al.* [174] have studied the use of an EPID for measurement of patient transmissions for the design of tissue compensators for, respectively, breast cancer patients and lung cancer patients. Hansen *et al.* [59], Heijmen *et al.* [63–66], Kirby and Williams [80, 81], Leong [89], Stroom *et al.* [144], Swindell [149], Wong *et al.* [172] and Ying *et al.* [175] have performed studies related to the use of an EPID for on-line dosimetric quality control of treatments (*in vivo* dosimetry).

Using an EPID for *in vivo* dosimetry has the following potential advantages in comparison with the usually applied silicon diodes: (i) Dosimetric data are obtained for a full plane, i.e. not only in a single or a few points. (ii) Dosimetric data are simultaneously obtained with patient positioning data which facilitates the interpretation of the dosimetric data. (iii) In vivo dosimetry with an EPID that is already in use for patient positioning verification does not lead to increased treatment times of patients. (iv) There is no physical contact between the patient and the detector.

Several approaches for *in vivo* dosimetry with an EPID have been investigated: Kirby and Williams have developed a method for estimation of the on-axis patient exit-dose from measured SRI-100-signals, using a set of calibration measurements for homogeneous, flat waterequivalent absorbers [80, 81]. For patients treated for prostatic cancer, Stroom *et al.* have calculated on-axis midplane doses from SRI-100-signals measured during treatment [144]. Leong [89] and Wong *et al.* [172] have proposed to compare predicted portal dose images (PDIs) - i.e. dose distributions behind patients in a plane perpendicular to the beam axis - with PDIs measured during treatment to verify the correct implementation of a treatment plan. For a ^{60}Co beam, Wong *et al.* have assessed the accuracy of the Delta Volume method for prediction of PDIs in a plane close behind the patient [172]. Hansen *et al.* have presented preliminary data on the use of PDIs, measured with an EPID, for a 3D calculation of the dose distribution that was actually delivered to the patient [59].

In our institute we have developed an algorithm for very accurate prediction (1-2%) of transmissions of high energy photon beams through patients, based on CT-data [63, 64]. Calculations are performed in a plane at 160 cm from the focus, which is equal to the fixed distance between the focus and the fluorescent screen of an SRI-100 EPID. In an on-going project we will develop methods to use these calculated patient transmissions, together with *in vivo* measured PDIs with an SRI-100, to estimate dose distributions that have actually been delivered to the patients.

In this paper we report on characteristics of the Philips SRI-100 electronic portal imaging device, relevant to accurate and reproducible portal dose measurement. The relation between grey scale values measured with the EPID and portal doses, measured with an ionisation chamber, has been investigated. The applied SRI-100 is the first prototype of this system, which is in clinical use since April 1988.

2.2 Materials and methods

The SRI-100 EPID basically consists of a fluorescent screen viewed by a CCD camera via two mirrors. The fluorescent screen is a 1.65 mm thick stainless steel plate coated with a fluorescent layer. The focus-to-fluorescent screen distance is 160 cm. At isocentre, the maximum optical image (i.e. detectable radiation field) is 27×21 cm^2. Optical images are digitized using the CCD camera (512×256 pixels; pixel size at isocentre: 0.53×0.82 mm^2). Charge integration can be performed both on the CCD chip - as it operates in slow-scan mode - and by adding multiple frames in a frame processor. In the final images the accumulated pixel signals are presented using 256 grey scale values. Technical details of the EPID have been described by Visser *et al.* [164].

Image acquisition for portal dose measurement was performed with a special procedure, written in the macro command language that comes with the system.* This procedure was also used by Heijmen *et al.* [65, 66] and by Stroom *et al.* [144] and is similar to the procedure described by Kirby and Williams [81]. Each image was acquired by accumulating 120 frames in the frame processor and for each frame an integration time on the CCD chip of 240 ms was used, resulting in a (fixed) acquisition time of about 38 seconds. Consequently, for the 6 MV photon beam of the applied treatment unit (Philips SL 75-10) with a dose rate of 340 monitor units min^{-1}, EPID signals could be integrated for at maximum 220 monitor units (MU). The camera gain, which was kept fixed for all measurements, was selected to yield grey scale values of about 200 for an irradiation with an open, 30×30 cm^2 field with 200 MU. Each image was corrected for 'dark current' in the CCD chip, which was measured in 30 frames prior to the irradiation. To avoid that negative 'dark current' signals would be truncated, the camera offset was chosen such that the average grey scale value in the 'dark current' image was about 20. For noise reduction, grey scale values were always averaged over selected regions of interest (ROIs) in the image.

In this paper, field sizes, coordinates in EPID images and PDIs, dimensions of ROIs in images, as well as distances to the beam axis, are all defined in the plane through the isocentre, perpendicular to the beam axis, i.e. at 100 cm from the focus.

2.2.1 Day-to-day variation in EPID response

A prerequisite for daily dosimetric quality control of linacs and *in vivo* dosimetry with an EPID is an adequate time independence of the response of the device, i.e. day-to-day variations in the response (measured grey scale value per unit of delivered portal dose) have to be small. To assess the time dependence of the EPID response, on 14 days in a 38 days period, *one* EPID image was measured in an open 30×30 cm^2 beam, *followed* by a characterisation of the beam profile with a radiation beam analyser, consisting of a linear array of ionisation chambers. Measurements with the analyser were performed along the two main axes of the EPID with a focus-to-analyser distance of 100 cm. The distance between centres of neighbouring chambers was 15 mm; the chamber dimensions were $9\times34\times3$ mm^3. Irradiations were performed with 150 MU.

Position dependent, local responses of the EPID were determined as ratios of the average grey scale value in a ROI of 9×34 mm^2 in the EPID image defined by the projection of an

*The applied procedure is available on request.

ionisation chamber of the analyser onto the EPID screen, and the - for temperature and pressure variations corrected - reading of the corresponding ionisation chamber.

In this way the day-to-day variation in the local EPID response was assessed for 14 points along the x-axis (corresponding with 14 ionisation chambers) and 14 points along the y-axis.

2.2.2 The EPID response as a function of applied monitor units, absorber thickness and field size

In the investigations regarding the dependence of the EPID response, G/D_p, on the applied number of monitor units (MU), the absorber thickness (t) and the field size (w), G was the average grey scale value in a ROI of 1 cm^2 around the beam axis; the portal dose D_p was measured at the beam axis at a depth of 1.0 cm in a polyethylene slab phantom (35×35 cm^2, thickness 2.5 cm) using an NE-2571 ionisation chamber. The distance from the focus to the surface of the polyethylene phantom was 160 cm which equals the focus-to-fluorescent screen distance of the EPID. As EPID and portal dose measurements cannot be performed simultaneously, the two types of measurements were always performed sequentially, keeping the time interval as short as possible (less than 5 minutes).

2.2.2.1 Monitor units

The dependence of the EPID response on MU was studied with a flat waterequivalent absorber (polystyrene) with a thickness of 20 cm in the beam. The source-to-surface distance was 90 cm and the field size was 10×10 cm^2. The selected range of MU (> 80) is typical for most of our treatments in the pelvic area.

2.2.2.2 Absorber thickness

As the fluorescent screen of the SRI-100 is composed of non-waterequivalent materials, the EPID response might change with spectral changes in the photon beam, as introduced by an absorber (patient) in the beam. To study the absorber thickness dependence of the EPID response, G/D_p-ratios were determined for a water phantom absorber with thicknesses from 10 to 29 cm; the centre of the absorber was always located at the isocentre of the treatment unit. Measurements were performed for fields of 6×6, 10×10, 15×15 and 20×20 cm^2. All irradiations were performed with 100 MU.

2.2.2.3 Field size

To assess the EPID response as a function of field size, G/D_p-ratios were determined for a set of square fields from 3×3 to 20×20 cm^2, without any absorber in the beam. All irradiations were performed with 100 MU.

The following two experiments, designated A and B, were performed to investigate the cause of the observed increase in the on-axis G/D_p-ratio with increasing square field size. In the first experiment (A) the fluorescent screen of the EPID was replaced by a, for visible light, semi-transparant white PMMA plate which was irradiated with photons of the 25×25 cm^2 *light* field in the treatment head. CCD images were recorded for a range of square, optical fields, defined by (black) cardboard collimators which were positioned on the PMMA plate. In experiment B the CCD camera was directly viewing (i.e. without using optical elements like

mirrors) a flat, diffuse light source; for this experiment the camera was outside the gantry and the EPID box was not used. The set-up, consisting of the light source and the CCD camera, was fully enclosed by a black curtain and positioned in a dark room. Again, CCD images were recorded for a range of square, optical fields, defined by cardboard collimators.

A function $K(r)$, describing the increase in EPID response at the beam axis per cm^2 irradiated surface of the fluorescent screen at a distance r from the beam axis, was derived from on-axis measured G/D_p-ratios using the following method: First, the measured G/D_p-ratios for all square fields $w_n \times w_n$ $(n = 1, \ldots, N)$ were normalised to the ratio for the 10×10 cm^2 field. Next, these normalised G/D_p-ratios were used to derive normalised G/D_p-ratios for circular fields, assuming that the normalised response, $G/D_p(R)$, for a circular field with a radius R equals the normalised response for a square field of $w\times w$ cm^2 with w defined by the relation $w^2 = 2\pi R^2$. $K_1(r)$, a first approximation of $K(r)$, was calculated by numerical differentiation of the function $G/D_p(R)$. Modifications of $K_1(r)$, performed to correct for (small) errors related to the above assumed equivalence between square- and circular fields, were calculated as follows: For all square fields $w_n \times w_n$ $(n = 1, \ldots, N)$ in succession, starting with the smallest field w_1, the normalised $G/D_p(w_n)$-ratio was estimated using the equation $G/D_p(w_n) = \int K_n(\sqrt{(x')^2 + (y')^2})\, dx'\, dy'$, with $K_n(r)$ the current approximation of $K(r)$; next, $K_{n+1}(r)$ was calculated by equally spreading the difference between the estimated and the measured normalised $G/D_p(w_n)$-ratio over rings with radii smaller than $\frac{1}{2}w_n$. Finally, $K(r)$ was set equal to $K_{N+1}(r)$.

In order to validate $K(r)$, measured on-axis G/D_p-ratios for *rectangular* fields $a\times b$ (including strongly elongated fields such as 6×20 and 20×6 cm^2), centred around the beam-axis, were compared with G/D_p-ratios calculated with

$$G = \left.\frac{G}{D_p}\right|_{10\times10} D_p \int\limits_{(x',y')\,\epsilon\,(a\times b)} K(\sqrt{(x')^2 + (y')^2})\, dx'\, dy', \tag{2.1}$$

with $G/D_p|_{10\times10}$ the measured absolute response for the 10×10 cm^2 field and D_p the measured absolute on-axis portal dose for the $a\times b$ cm^2 field.

2.2.3 Grey scale values and portal doses behind a thorax phantom

For a thorax phantom, experiments were performed to investigate the validity of the equation

$$G(x, y) = \left.\frac{G}{D_p}\right|_{10\times10} \int\limits_{(x',y')\epsilon\text{field}} D_p(x', y')\, S(x', y')\, K(\sqrt{(x'-x)^2 + (y'-y)^2})\, dx'\, dy', \tag{2.2}$$

to connect grey scale values with portal doses, with $G(x, y)$ the measured grey scale value in point (x, y) of the EPID image, $D_p(x, y)$ the absolute portal dose in point (x, y) of the PDI, $G/D_p|_{10\times10}$ the absolute, on-axis EPID response for the open 10×10 cm^2 field and $S(x, y)$ the local, relative EPID response in (x, y). $K(r)$ has been described in the previous section.

As $S(x, y)$ should reflect the *local* EPID response in (x, y), it was determined as the measured G/D_p-ratio for a *small* field (3×3 cm^2) centred around (x, y), normalised at the beam axis ($S(0, 0) = 1$). G was the average grey scale value in a ROI of 1 cm^2 around (x, y) and D_p

was the portal dose measured with an ionisation chamber in a set-up as described previously, but with the chamber centre located at the ray-line through (x, y). $S(x, y)$-measurements were performed for points (x, y) in a square grid with distances of 3 cm between neighbouring points. Measurements were performed without any absorber in the beam.

In equation (2.2), $K(r)$ is used as the point spread function of the EPID, describing crosstalk effects. The convolution integral expresses the idea that for non-flat portal dose distributions $D_p(x, y)$, e.g. behind a patient or in case of application of intensity modulated beams, the effect of the point spread function $K(r)$ has to be modulated with local beam intensities, which are considered to be proportional to $D_p(x, y)S(x, y)$. Convolution integrals, defined in equation (2.2), were solved using a Fast Fourier routine written in Fortran. The grid size was 2.5 mm. By performing a deconvolution, equation (2.2) could in principle be used to derive PDIs from measured EPID images (this has not been done in this paper).

Grey scale value distributions $G(x, 0)$ along the x-axis, defined as average grey scale values in ROIs of 3.2×3.7 mm^2 around points $(x, 0)$, as derived from EPID images measured behind the thorax phantom, were compared with values predicted with equation (2.2), using measured absolute portal dose distributions as input. Relative portal dose distributions were measured by scanning an ionisation chamber (0.15 cm^3) at a depth of 1.0 cm through a water phantom (Wellhöfer); for conversion to absolute portal doses, an absolute dose measurement at the beam axis was performed. The source-to-surface distance was 160 cm. EPID measurements and absolute portal dose measurements were performed with 150 MU irradiations.

The applied thorax phantom, made of PMMA and cork (lungs), had a constant cross section in craniocaudal direction, i.e. in the y-direction. Portal dose measurements were only performed along the x-axis; for $G(x, 0)$-predictions with equation (2.2) it was assumed that $D_p(x, y) = D_p(x, 0)$. Considering the symmetry of the phantom and the fact that portal doses $D_p(x, y)$ only contribute in second order (i.e. via the tail of the point spread function $K(r)$), to calculated grey scale values $G(x, 0)$, this is a reasonable assumption.

2.3 Results

2.3.1 Day-to-day variation in EPID response

In figures 2.1a and 2.1b, data are presented regarding day-to-day variations in the EPID response. The 14 lines in figures 2.1a and 2.1b represent the observed time-behaviour of measured local EPID responses in 14 points along, respectively, the x- and the y-axis of the EPID. For all 2×14 EPID points separately, the day-to-day variation in the measured response has been quantified as a standard deviation in the observed responses. The average of these 28 standard deviations is 0.55%. The estimated measurement uncertainty of local responses, related to the uncertainty in the dose measurements with the radiation beam analyser and to the unavoidable sequentiality of EPID and beam analyser measurements, equals 0.35%. Therefore, the *real* average day-to-day response variation in the EPID points has been approximately 0.4% (1 SD).

The curves in figures 2.1a and 2.1b are to a high degree parallel. As a consequence, the day-to-day variations in *relative* EPID responses, e.g. normalised to the on-axis response, are within 0.2% (1 SD).

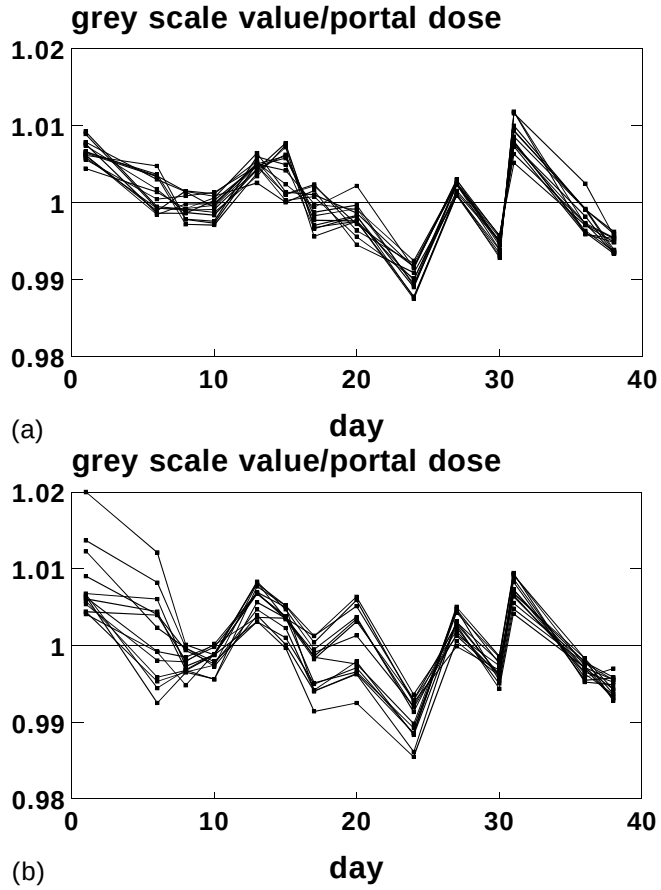

Figure 2.1. The observed day-to-day variation in a 38 days period in EPID response at 14 points along the x-axis of the EPID (a) and at 14 points along the y-axis (b). For presentation purposes, a normalization has been performed such that, for each line (i.e. each EPID point), the average observed response in the 38 days period is equal to unity.

2.3.2 The EPID response as a function of applied monitor units, absorber thickness and field size

2.3.2.1 Monitor units

In figure 2.2, the measured on-axis EPID response is shown as a function of the applied number of monitor units MU. Observed deviations from a linear response are within 0.5%. No saturation effects have been observed. Kirby and Williams have also found a linear relationship between measured grey scale values and applied dose for their SRI-100 EPID; they have also investigated very small numbers of MU [80, 81]. Also Leong has reported this linearity for a fluoroscopic system [89]. Both our system and Kirby's system have a dynamic range that allows resolving single monitor units.

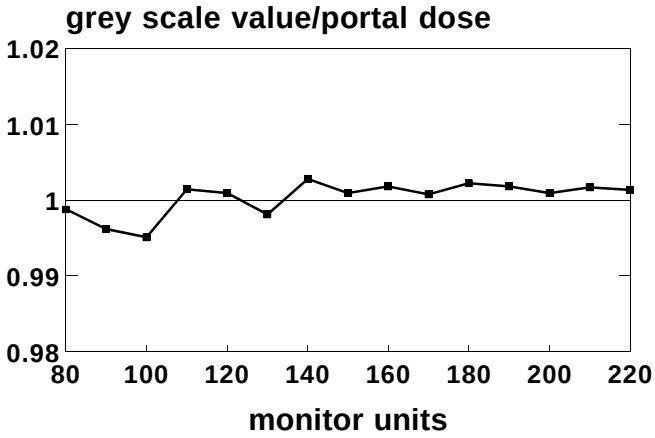

Figure 2.2. The observed EPID response at the beam axis as a function of the applied number of monitor units. The presented G/D_p-values have been normalised to the average measured value.

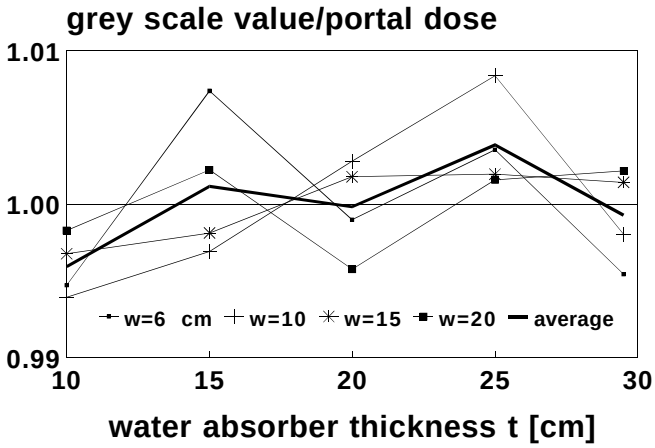

Figure 2.3. Measured grey scale value/portal dose-ratios for the beam axis as a function of absorber thickness t for a set of fields of $w \times w$ cm^2. For presentation purposes, for each field size separately, the presented G/D_p- values have been normalised to the average measured value. (figure 2.4 demonstrates that the G/D_p-ratio is rather strongly field size dependent.) The thick, solid line shows the average t-dependence of the EPID response for the four field sizes.

2.3.2.2 Absorber thickness

Figure 2.3 shows, for a set of field sizes, normalised, measured G/D_p-ratios as a function of the absorber thickness t. The data in figure 2.3 indicate that, for a fixed field size, the EPID response (G/D_p) does not significantly depend on the absorber thickness.

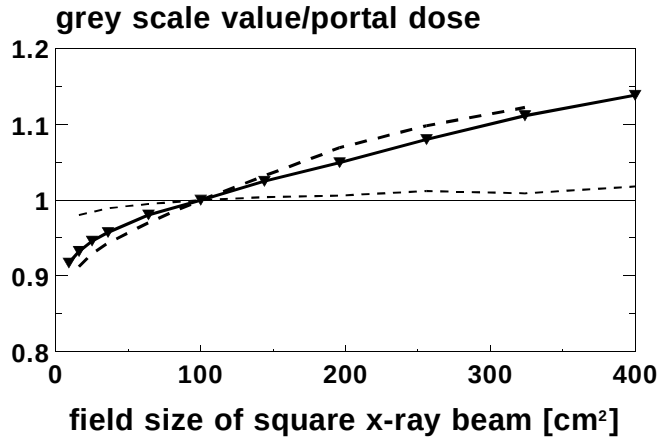

Figure 2.4. Solid line + markers: the EPID response, measured at the beam axis, as a function of the field size of the applied square irradiation fields. The presented on-axis G/D_p-ratios have been normalised to the observed ratio for the 10×10 cm^2 field. There was no absorber in the beam. The thick and thin dashed curves are results of experiments A and B, described in section 2.3.2.3.

2.3.2.3 Field size

In figure 2.4, normalised, measured G/D_p-ratios are presented as a function of the field size of the applied square irradiation fields, showing a rather strong field size dependence of the EPID response. The thick- and thin dashed lines in figure 2.4 show for, respectively, experiments A and B (both described in section 2.2.2.3) the measured grey scale values at the beam axis, relative to the grey scale value for the 10×10 cm^2 field. The close agreement between the solid line with markers and the thick, dashed curve proves that the G/D_p-dependence on radiation field size is basically *not* a direct consequence of the interaction of the x-ray beam with the fluorescent screen. The strongly reduced field size dependence observed in experiment B proves that the increase of the EPID response with increasing x-ray field size is basically *not* due to crosstalk effects in the CCD camera. From the results of the experiments A and B it may be concluded that the increase in EPID response with increasing x-ray field size is mainly due to contributions to the EPID signal from scattered light: Visible photons produced by the x-ray beam in a point of the fluorescent screen do not only generate directly a grey scale value in the corresponding point of the EPID image, but do also lead - due to light scatter from components of the EPID structure, such as the walls and the mirrors, onto the CCD chip - to an increased grey scale value in all other points of the image.

Using the method explained in section 2.2.2.3, the normalised, measured G/D_p-ratios presented in figure 2.4 were used to derive the function $K(r)$. $K(r)$ is depicted in figure 2.5. For all measured data points $G/D_p(w)$ in figure 2.4, $K(r)$ fulfills within 0.6% (maximum deviation) the consistency relation $G/D_p(w) = \int K(\sqrt{(x')^2 + (y')^2})\, dx'\, dy'$.

In table 2.1, measured on-axis G/D_p-ratios for rectangular fields are compared with ratios, calculated with equation (2.1). The agreement between measured and predicted ratios is within 0.3% (1 SD). The observed close agreement between measurements and predictions, also for

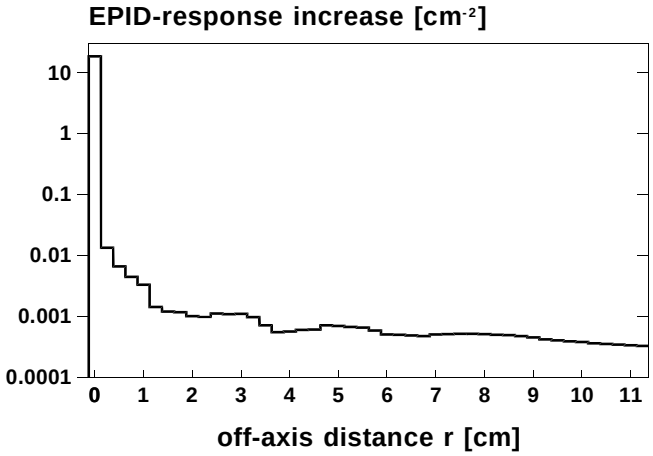

Figure 2.5. The function $K(r)$, describing the increase in EPID response at the beam axis per cm^2 irradiated fluorescent screen at a distance r from the beam axis. $K(r)$ was derived from the data (markers) presented in figure 2.4.

strongly elongated fields, supports the use of $K(r)$ and equation (2.1) for determination of the on-axis portal dose D_p from measured grey scale values G in non-square irradiation fields.

2.3.3 Grey scale values and portal doses behind a thorax phantom

The experimental set-up for the investigations on the thorax phantom absorber is schematically shown in figure 2.6a. In figure 2.6b, measured and predicted grey scale values are presented for a 15×10 cm^2 x-ray field, showing close agreement (typically, deviations smaller than 1-2% outside the penumbra regions) between $G(x,0)$-measurement with the EPID and $G(x,0)$-prediction with equation (2.2). The same small deviations have been found for other field sizes. The dotted line in figure 2.6b is the measured normalised EPID response - as defined in section 2.2.3 - along the x-axis, i.e. $S(x,0)$.

The dashed curve in figure 2.6b was derived using the following linear relation for grey scale value prediction (instead of equation (2.2)): $G(x,0) = C'D_p(x,0)S(x,0)$ with C' the measured on-axis G/D_p-ratio for the *open* 10×10 cm^2 field, $D_p(x,0)$ the portal dose in $(x,0)$ behind the phantom, and $S(x,0)$ the normalised EPID response in $(x,0)$. Figure 2.6b shows, around the beam axis, a reasonable agreement between this prediction and the measurements. However, in the mediastinal region, deviations of up to 7% do occur; in the areas $x < -8$ cm and $x > 8$ cm, deviations are as large as 50%. These observations do clearly demonstrate that the magnitude of the crosstalk effects in the EPID is such that, grey scale value distributions measured with the EPID, normalised to the on-axis value, can differ significantly in shape from normalised portal dose distributions, also after correction for the non-uniform spatial EPID response ($S(x,y)$). Furthermore, these results point at an inherently limited accuracy of the method of Kirby *et al.* for the determination of on-axis patient exit-doses from measured SRI-100-signals, using a set of calibration measurements for homogeneous, flat waterequivalent absorbers, when applied in the thorax region of patients or in case of the use of (strongly)

Table 2.1. Measured and predicted on-axis EPID responses G/D_p for rectangular fields. The predictions were performed using equation (2.1).

Field size		Grey Scale Value/Portal Dose		
a [cm]	b [cm]	measured	calculated	diff. [%]
6	4	0.942	0.938	0.4
4	6	0.941		0.3
10	4	0.954	0.951	0.3
4	10	0.957		0.6
16	5	0.975	0.976	-0.1
5	16	0.980		0.4
12	8	0.995	0.993	0.1
8	12	0.993		-0.1
20	6	1.005	1.000	0.5
6	20	0.995		-0.6
14	10	1.017	1.019	-0.1
10	14	1.022		0.3
18	10	1.047	1.039	0.8
10	18	1.037		-0.2
20	15	1.099	1.095	0.3
15	20	1.099		0.3

intensity modulated beams [80, 81].

2.4 Summary and conclusions

Characteristics of the Philips SRI-100 electronic portal imaging device, relevant to portal dose measurement in radiotherapy, have been investigated. Image acquisition has been performed with a special procedure, written in the macro command language that comes with the system.

A day-to-day variation in EPID response of 0.4% (1 SD) has been observed; variations in *relative*, local EPID responses (e.g. normalised to the on-axis response) are within 0.2% (1 SD).

Measured grey scale values are linearly proportional to transmitted portal doses with a proportionality constant which is independent of the thickness of a flat, waterequivalent absorber in the beam, but which does significantly depend on the size of the applied x-ray beam.

It has been shown that the observed increase in on-axis EPID response with increasing field size is mainly due to contributions to the EPID signal from scattered light: Visible photons produced by the x-ray beam in a point of the fluorescent screen do not only generate a grey

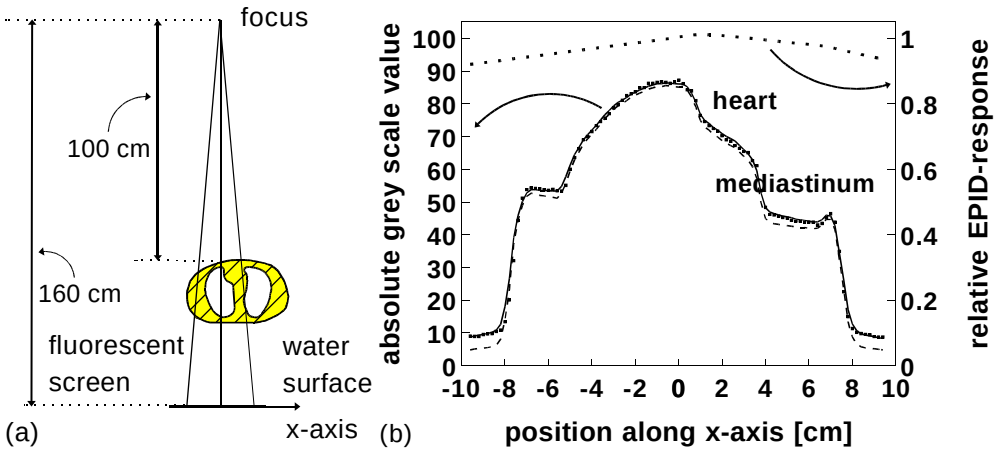

Figure 2.6. (a) A schematic picture of the set-up used to generate the data presented in (b). For the EPID measurements, the horizontal line at 160 cm from the focus represents the fluorescent screen; for the portal dose measurements this line represents the water surface. (b) Measured and predicted grey scale value distributions behind a thorax phantom. The set-up is presented schematically in (a). The markers represent grey scale values measured with the EPID. The solid line is the predicted grey scale value distribution according to equation (2.2). The dashed curve is a prediction, based on an assumed linear relationship between $G(x,0)$ and $D_p(x,0)$. The dotted line is the measured relative EPID response along the x-axis.

scale value in the corresponding point of the EPID image, but do also lead - due to light scatter from components of the EPID structure onto the CCD chip - to an increased grey scale value in all other points of the image.

A function $K(r)$, describing the increase in EPID response at the beam axis per cm^2 irradiated fluorescent screen at a distance r from the beam axis, has been derived from measured on-axis G/D_p-ratios for square fields. For a set of rectangular fields, the measured on-axis G/D_p-ratio has been compared with the predicted ratio, calculated with $K(r)$ and the known on- axis portal dose. The observed close agreement between measurements and predictions, also for strongly elongated fields, supports the proposed use of $K(r)$ for determination of the portal dose D_p from measured grey scale values G in non-square irradiation fields. For a thorax phantom, predicted on- and off-axis grey scale values, calculated with a convolution integral with $K(r)$ as point spread function, are in close agreement (1-2%) with EPID measurements.

In conclusion: The observed small day-to-day variation in the response of the SRI-100 is crucial for application of the EPID for accurate daily dosimetric quality control of treatment units and for on-line dosimetric treatment verification (*in vivo* dosimetry). The, for each field size observed, proportionality between measured grey scale values and transmitted portal doses, independent of the absorber thickness in the beam, facilitates a straightforward application of the SRI-100 for *in vivo* dosimetry and for the design of tissue compensators, based on patient transmissions measured with the EPID. Methods have been developed that accurately described the relation between grey scale values in EPID images and portal doses measured

with an ionisation chamber. In an on-going project we are developing methods to use portal doses, derived from '*in vivo* measured' SRI-100 EPID images, to estimate dose distributions that have actually been delivered to patients.

Acknowledgements

The authors would like to thank P.R.M. Storchi, J.B. v.d. Kamer, O.O. Graveland, D. Binnekamp and J.C. Stroom for their contributions. This work was supported by grant No. DDHK 94-848, awarded by the Dutch Cancer Society.

Chapter 3

Accurate portal dose measurement with a fluoroscopic electronic portal imaging device for open and wedged beams and dynamic multileaf collimation

K.L. Pasma, M. Kroonwijk, J.C.J. de Boer, A.G. Visser and B.J.M. Heijmen
Phys. Med. Biol. 43(8): 2047-2060, 1998.

Measuring portal dose with an electronic portal imaging device (EPID) in external beam radiotherapy can be used to perform routine dosimetric quality control checks on linear accelerators and to verify treatments (in vivo dosimetry). An accurate method to measure portal dose images (PDIs) with a commercially available fluoroscopic EPID has been developed. The method accounts for (i) the optical "cross talk" within the EPID structure, (ii) the spatially non-uniform EPID response and (iii) the non-linearity of the EPID response. The method is based on a deconvolution algorithm. Measurement of the required input data is straightforward. The observed non-linearity of the EPID response was largely due to the somewhat outdated EPID electronics. Non-linearity corrections for more modern systems are expected to be smaller. The accuracy of the method was assessed by comparing PDIs measured with the EPID with PDIs measured with a scanning ionization chamber in a mini phantom, located at the same position as the fluorescent screen. For irradiations in open, wedged and intensity modulated 25 MV photon beams (produced with dynamic multileaf collimation) EPID and ionization chamber measurements agreed to within 1% (1 SD).

3.1 Introduction

The main application for electronic portal imaging devices (EPIDs) is patient set-up verification. However, they can also be used for dosimetric treatment verification. Already in 1986, Leong investigated the dosimetric properties of their video based EPID [89]. In 1991, Morton *et al.* reported on the dosimetric characteristics of an EPID based on a linear array of scintillation crystals [106]. In recent years, several other groups have also studied the properties of their EPIDs for dosimetric measurements. Most studies were performed for two commercial systems, the fluoroscopic, CCD camera based Philips SRI-100 EPID [61, 80, 81] and the Varian PortalVision liquid-filled matrix ion chamber system [43, 44, 173, 176]. The SRI-100 was developed in a collaboration between the former Philips Radiotherapy Systems, the former Laboratory for Space Research in Leiden and the Daniel den Hoed Cancer Center [164]. The PortalVision system was developed by van Herk and Meertens [160].

Several studies on dosimetric applications of EPIDs have been performed. Kirby and Williams have evaluated possibilities for the use of the SRI-100 EPID for quality control checks on the beam profile of a treatment unit [81]. In our institute, this EPID is in daily use for quality control of the absolute output and field flatness of the 10 and 25 MV scanning photon beams of a MM50 racetrack microtron [39].

A number of groups has performed studies with anthropomorphic phantoms and/or patients to evaluate the use of EPIDs for dosimetric quality control of treatments (in vivo dosimetry) [43, 44, 59–61, 80, 85, 98, 99, 125, 176]. Several approaches for in vivo dosimetry with an EPID have been proposed. Kirby and Williams have presented a method for estimation of the on-axis patient exit dose from measured SRI-100-signals, using a set of calibration measurements for homogeneous, flat, water-equivalent absorbers [80, 81]. Leong [89] and Wong *et al.* [172] have proposed to compare a portal dose image (PDI) - i.e. a dose distribution behind a patient in a plane perpendicular to the beam axis, measured during treatment with an EPID - with a corresponding predicted PDI. For a ^{60}Co beam, Wong *et al.* have assessed the accuracy of the delta volume method for prediction of PDIs in a plane close behind the patient [172]. McNutt *et al.* have used the convolution/superposition method, based on precalculated Monte Carlo data, to predict the dose distribution throughout an extended volume which includes the patient and the EPID [98]. The calculated dose distribution in the EPID is then extracted, yielding a predicted PDI.

In our institution, a method has been developed for prediction of PDIs in open and wedged beams, using the planning CT-data of the patients [64, 115]. The calculations are based on a set of input functions such as attenuation curves for primary radiation, and scatter point spread functions describing the radiation scattered from the patient onto the EPID. The input functions are derived from a limited set of measured beam transmissions through flat, polystyrene absorbers. For anthropomorphic phantoms the predicted PDIs agree within 1-2% with ionization chamber measurements. Both the method for PDI prediction and the method for measuring PDIs with an EPID, as described in this paper, have been evaluated clinically for prostate cancer patients [85]. It was shown that in some cases internal organ motion can be detected by comparing PDIs measured during treatment with predicted PDIs.

A few back-projection methods for derivation of the patient dose distribution from a PDI measured with an EPID have been proposed [59, 60, 99, 115, 175]. Accurate back-projection is only possible if the patient position and anatomy during treatment closely resemble the situation during acquisition of the planning CT-scan. In the method of Ying *et al.*, a deviating patient

anatomy at the time of treatment is accounted for with an iterative procedure that modifies the planning CT-data [175].

Recently, we have published a paper on the dosimetric characteristics of our Philips SRI-100 EPID for an open (non-wedged) 6 MV photon beam [61]. We found that the measured pixel value G_{raw} (EPID signals) is linearly proportional to the transmitted dose and that the system is very stable: the observed day-to-day variation of the EPID response per unit of delivered dose is 0.4% and the day-to-day variation in relative response (normalized to the on-axis response) is within 0.2%. However, the EPID response does significantly depend on the size of the applied x-ray beam. It was shown that this is mainly due to light scatter in the EPID structure: visible photons produced by the x-ray beam in a point of the fluorescent screen do not only generate a signal in the corresponding pixel of the EPID image, but also cause an increased signal at all other pixels due to light scatter from components of the EPID structure onto the CCD chip. A kernel describing the increase in on-axis EPID response per unit of area irradiated fluorescent screen at a distance r from the beam axis was derived from the measured on-axis response as a function of field size. It was shown that the derived kernel can be used in a convolution integral to connect portal dose with pixel values G_{raw} measured with the EPID.

In this paper we report on a method to derive absolute portal dose images from measured EPID images in the 25 MV photon beam of a MM50 racetrack microtron using a deconvolution algorithm to correct for the light scatter in the EPID structure as described by the kernel. The non-uniform EPID response and the non-linearity of the EPID response are also taken into account. Preliminary results have been presented at the XII$^{\text{th}}$ ICCR [125].

3.2 Materials and methods

3.2.1 EPID hardware and software

The SRI-100 EPID basically consists of a fluorescent screen, two mirrors and a CCD camera. The fluorescent screen is a 1.65 mm thick stainless steel plate coated with a 411 mg/cm^2 thick layer of Gd_2O_2S:Tb (gadolinium oxysulfide). To reduce the detection of high energy electrons generated in the patient, we have mounted an additional 1 mm thick stainless steel slab on top of the standard fluorescent screen. Image quality is hardly affected by this additional layer so that acquired images can be used for patient set-up verification and portal dose verification at the same time [85]. The water equivalent depth of the in total 2.65 mm thick stainless steel layer is slightly smaller than the depth of maximum dose of the 25 MV photon beam (3.0 cm). The added one millimeter thick stainless steel slab adds 1.3 kg to the weight of the EPID structure. To prevent extra sagging of the structure, which originally weighted about 15 kg, and to avoid loss of image quality we have chosen not to add a thicker slab. The EPID has a fixed focus-to-fluorescent screen distance of 160 cm. In this paper, field sizes, coordinates and distances to the beam axis are all defined in the plane through the isocenter (i.e. at 100 cm from the focus). The maximum detectable radiation field in that plane is 25×19 cm^2. The CCD camera frames (512×256 pixels) are digitized to 8 bits and added in a 16 bit deep frame store memory. Charge integration is performed both on the CCD chip and by adding multiple frames in the frame store memory. Technical details of the EPID have been described by Visser *et al.* [164] and Althof *et al.* [2]

Image acquisition for portal dose measurements is performed with a procedure written in the macro command language that comes with the system. It is similar to the procedure used

by Heijmen *et al.* [61] and Kirby and Williams [81]. However, several modifications have been made to optimize the signal-to-noise ratio; (i) the integration time for each frame on the CCD chip has been increased from 240 to 560 ms to reduce the read-out noise and (ii) the 16 bit deep images of the frame store memory are written directly to disk.* In the original procedure, the images that are stored on disk are only 8 bits deep. Especially for images with low pixel values, the truncation error resulting from this procedure is significant. Since in the new procedure no accuracy is lost due to truncation, the pixel values do not have to be maximized and, consequently, the selection of the integration time on the CCD chip and the number of frames that are accumulated in the frame store memory is less critical.

For dosimetric purposes, the total acquisition time has to exceed the irradiation time. In the applied procedure a fixed number of 60 video frames is accumulated in the frame store memory resulting in a fixed acquisition time of 38.4 s and a maximum irradiation time of 190 MU for a doserate of 300 MU min^{-1}. Each image is corrected for the 'dark current' measured prior to the irradiation. No image enhancement is performed on the images that are used to derive PDIs. Image acquisition starts automatically when the measured pixel values in the center of the video frame reach a threshold, i.e. when the beam is switched on. The last frames are accumulated after the irradiation has ended. The measured pixel values (G_{raw}) are an accumulation of the pixel values in 'filled' (beam on) and 'empty' (beam off) frames divided by the total number of frames (60). The camera gain is fixed to unity.

3.2.2 Dose measurements with an ionization chamber

Ionization chambers are considered the gold standard for dose measurements. In this study a PTW ionization chamber (N31002) was used to derive the relationship between the EPID images $\mathbf{G}_{\text{raw}}$ and portal dose images (PDIs). The ionization chamber was positioned at a depth of 2.5 cm in a polystyrene mini phantom with a transversal cross section of 7×7 cm^2 and a thickness of 5 cm. The center of the ionization chamber was positioned at a distance of 160 cm from the focus, which is equal to the fixed focus-to-fluorescent screen distance of our EPID. For off-axis measurements, the mini phantom with the ionization chamber inserted, was scanned in an empty RFA-300 water phantom.†

Empirically it was found that for a wide range of field sizes, a depth of 2.5 cm resulted in minimal variations in the on-axis response of the system (pixel value/portal dose (G/D_p)) beneath flat phantoms with various thicknesses (t) and exit plane-to-detector-distances (L). In these analyses, pixel values were corrected for the non-linear response of the EPID, described in section 2.3.1.

3.2.3 The non-linear EPID response

In a recent study, EPID signals were found to be linearly proportional to transmitted portal doses in a 6 MV photon beam [61]. For the 25 MV photon beam we found the ratio of G_{raw} and D_p to decrease with increasing portal dose D_p, mainly due to non-linear electronics in the EPID [125]. These results are not contradictory. Due to the extra build-up layer in the present study and the integration time that is a factor of $2\frac{1}{3}$ longer, EPID signals measured for the 25 MV beam are at least a factor of $2\frac{1}{3}$ higher than those measured for the 6 MV beam.

*The applied procedure is available on request.

†Scanditronix Medical AB

Therefore, the 6 MV and 25 MV measurements are on different parts of the response curve of the system.

3.2.3.1 A correction for the non-linear EPID response

A method has been developed to correct measured EPID signals for the non-linear response of the EPID. This method not only corrects for non-linear electronics but also accounts for (potential) differences in sensitivity of the EPID and the ionization chamber for spectral changes in the beam due to the patient. The method is based on a conversion of measured pixel values per filled frame, g_{raw}, into corrected values g. For each pixel, the value per filled frame g_{raw} is derived from the measured pixel value G_{raw} using

$$g_{\mathrm{raw}} = \gamma G_{\mathrm{raw}}, \tag{3.1}$$

with γ the ratio of the total frames and filled frames which is equal to the ratio of the total accumulation time and the irradiation time. g_{raw}-values are then converted into corrected values g using a polynomial function:

$$g = a_1\, g_{\mathrm{raw}} + a_2\, g_{\mathrm{raw}}^2 + a_3\, g_{\mathrm{raw}}^3. \tag{3.2}$$

Finally, g-values are divided by γ yielding corrected pixel values G.

To derive the parameters a_1, a_2 and a_3 in this equation, on-axis G_{raw} and D_p values are measured beneath flat polystyrene absorbers of various thicknesses. The distance between the exit plane of the absorbers and the detector (L) is fixed to 47.5 cm. Measurements are performed for a set of square $w \times w$ fields. The parameters a_1, a_2 and a_3 are determined by minimization of

$$\sum_{w,t,L} \left(\frac{g(w, t = 25, L = 47.5)}{D_p(w, t = 25, L = 47.5)} - \frac{g(w, t, L)}{D_p(w, t, L)} \right)^2, \tag{3.3}$$

$g(w, t = 25, L = 47.5)$ and $g(w, t, L)$ are derived from the measured on-axis pixel values G_{raw} using equations (3.1) and (3.2). The minimization of equation (3.3) is based on the assumption that the optical "cross talk" in the EPID should be independent of the thickness t of the absorber. An iterative algorithm with a Newton type search method is used to obtain a_2 and a_3. a_1 is set to unity to prevent the non-physical $a_1 = a_2 = a_3$=0 solution. The initial values of a_2 and a_3 are zero.

3.2.3.2 Non-linearity of the EPID electronics

By varying the accumulation time on the CCD chip it is possible to determine which part of the problem is only related to non-linear electronics. The ratio of the on-axis pixel values per filled frame, *corrected for the non-linear electronics*, measured with integration times on the CCD chip of T_{int1} ($g(w, t, L, T_{\mathrm{int1}})$) and T_{int2} ($g(w, t, L, T_{\mathrm{int2}})$) should be equal to the ratio of the integration times. This should hold for each w, t, L-combination and can therefore be used to derive a_1, a_2 and a_3 of a third degree polynomial response curve of the EPID electronics by minimizing:

$$\sum_{w,t,L} \left(\frac{g(w, t, L, T_{\mathrm{int1}})}{g(w, t, L, T_{\mathrm{int2}})} - \frac{T_{\mathrm{int1}}}{T_{\mathrm{int2}}} \right)^2. \tag{3.4}$$

Since the spectrum of the beam is unchanged if only the integration time on the CCD chip is altered, the derived g only corrects for non-linear electronics. Differences between the response curve of the EPID electronics and the curve derived with the method described in the previous section point at differences in spectral sensitivity of the EPID and the ionization chamber.

Using the same w, t, L-combinations as in section 3.2.3.1, we have performed EPID measurements for two integration times on the CCD chip: T_{int1}=560 ms and T_{int2}=240 ms. For the measurements with the integration time of 240 ms the number of frames was increased from 60 to 120.

3.2.4 Deconvolution of EPID images to obtain portal dose images

3.2.4.1 Derivation of the sensitivity $S(x, y, w)$ of the EPID

In a previous paper we introduced the following relation between a corrected EPID image and the corresponding PDI [61]

$$\mathbf{G} = \left.\frac{G}{D_p}\right|_{\text{ref}} \cdot \mathbf{D_pS} \otimes \mathbf{K}, \tag{3.5}$$

with **S** an array describing the relative EPID sensitivity (S=1 at the beam axis), $\otimes$ refers to a convolution, $G/D_p\big|_{\text{ref}}$ is the absolute on-axis EPID response for a reference situation ($w \times w$=10 $\times$ 10 cm^2, t=25 cm, L=47.5 cm, $\dot{D}$=300 MU min^{-1} and T_{int}=560 ms) and **K** is a kernel describing the optical "cross talk" in the EPID. Pasma *et al.* observed that **S** in equation (3.5) is slightly field size dependent [125]. This dependency is related to shortcomings of the on-axis measured kernel K in describing optical "cross talk" in off-axis points.

S arrays are derived from corrected EPID images **G** and corresponding portal dose distributions $\mathbf{D_p}$ for a set of square fields below a flat 25 cm thick polystyrene absorber positioned at a distance L=47.5 cm from the detector plane. The set-up for the required ionization chamber measurements is described in section 3.2.2. The function $K(r)$, describing the increase in EPID response at the beam axis per square centimeter irradiated fluorescent screen at distance r from the beam axis, is derived from on-axis measured G/D_p-values (normalized to the reference situation) as a function of field size [61] and stored in a two dimensional array **K**. For each field size, **S** is derived from equation (3.5) by deconvolving **G** with **K** and dividing the resulting $\mathbf{D_pS}$ array by $\mathbf{D_p}$ as measured with the scanning ionization chamber. Straightforward deconvolving **G** with a fast fourier transform (FFT) routine yields physically unrealistic solutions for **S** since **G** is derived from measured EPID images which inevitably contain some noise [125]. Therefore, we use an iterative method based on successive approximations [135]:

$$(\mathbf{D_pS})_{i+1} = \left(\left.\frac{G}{D_p}\right|_{\text{ref}}\right)^{-1} \lambda\mathbf{G} + (\mathbf{I} - \lambda\mathbf{K}) \otimes P(\mathbf{D_pS})_i \,, \tag{3.6}$$

with **I** the identity operator, λ a constant parameter, P a constraint operator and i the i^{th} iteration. The initial approximation of the $\mathbf{D_pS}$-array ($(\mathbf{D_pS})_0$) is equal to $D_p(w = 10, t = 25, L = 47.5)$ inside the field and zero outside. Only physically realistic modifications are allowed; e.g. negative elements of modified $(\mathbf{D_pS})_i$ arrays are set to zero by operator P. Furthermore, elements of **S** outside the field are set to zero. Within 10 iterations the procedure converges to

a solution $\mathbf{D_pS}$. All calculations are performed with arrays of 64 × 64 elements, each element represents a region of interest of 0.5 × 0.5 cm^2.

3.2.4.2 Derivation of a PDI in clinical practice

In clinical practice, a measured EPID image $\mathbf{G}_{\text{raw}}$ is corrected for the non-linear behavior of the EPID using the method described in section 3.2.3.1 and the resulting image $\mathbf{G}$ is deconvolved to account for the optical "cross talk" using the above described procedure. The resulting $\mathbf{D_pS}$ is then divided by the $\mathbf{S}$-array of the smallest square field that includes the applied patient field to derive D_p.

For dynamic multileaf collimation, the EPID measurements are performed with the procedure described in section 3.2.1, with the difference that image acquisition was started manually since the standard procedure uses pixels in the center of the image to detect whether the beam has been switched on and these pixels are usually blocked by the leaves when the irradiation starts. For dynamic multileaf collimation, the ratio of filled and empty frames γ, used for the non-linearity correction described in section 3.2.3.1, is not constant over the whole image like for a static open or wedged field. We use the calculated number of MU for each position divided by the total number of MU given during the irradiation to estimate γ for each position.

3.3 Results

3.3.1.1 A correction for the non-linear EPID response

Measured on-axis ratios of G_{raw} and D_p for square fields of 3 × 3, 5 × 5, 10 × 10, 15 × 15 and 18 × 18 cm^2 and absorber thicknesses 0, 10, 15, 25 and 35 cm are depicted in figure 3.1 (dotted lines). G_{raw} is the average EPID pixel value in a region of 1.5 cm^2 around the beam axis. From t=0 to t=35 cm the ratios increase by 6% and 10% for the smallest field and largest field, respectively. For small thicknesses and large fields, i.e. for high portal doses and EPID signals, the measured pixel values are relatively low; the response of the system is non-linear.

The measured pixel values per filled frame g_{raw}, for the same w, t-combinations as used to derive the ratio G_{raw} over D_p presented in figure 3.1 (dotted lines), have been plotted in figure 3.2 (markers) against the fully corrected pixel values per filled frame g (corrected for non-linear electronics and spectral sensitivity). The response curve (solid line) is defined by equation (3.2) with a_1-, a_2- and a_3-values of 1, -5.9 × 10^{-4} and 7.52 × 10^{-6}, respectively. The ratio of empty frames and filled frames, γ, was 1.28. The dashed line shows the response of an EPID with a perfectly linear response.

Using the response function as depicted in figure 3.2 to correct measured ratios of G_{raw} and D_p presented in figure 3.1 (dotted lines) results in ratios of G and D_p (solid lines) that show no systematic dependence on absorber thickness t; the maximum standard deviation in the derived ratios as a function of thickness is 0.7% for w=3 and the mean of the standard deviations for all field sizes is 0.4%.

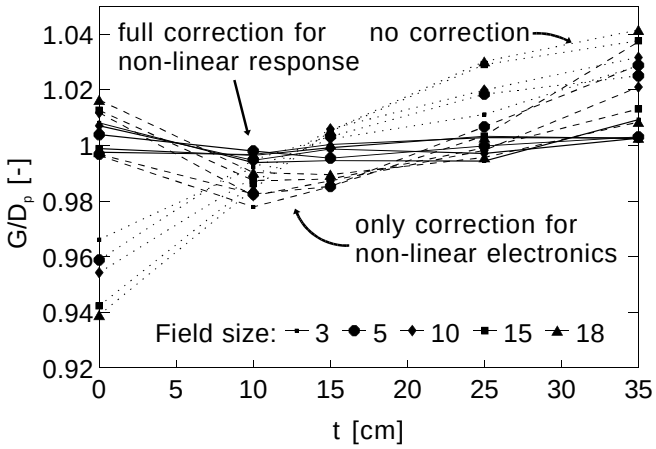

Figure 3.1. Measured ratios of pixel value and portal dose (dotted lines) at the beam axis as a function of the absorber thickness t for five square fields. For presentational purposes, for each field separately, the presented ratios of G and D_p have been normalized to the average measured value. The solid lines represent the ratios of G and D_p corrected for the non-linear EPID response shown in figure 3.2. The results are discussed in section 3.3.1.1. The dashed lines represent the ratio G and D_p corrected only for the non-linear EPID electronics using the method described in section 2.3.2.

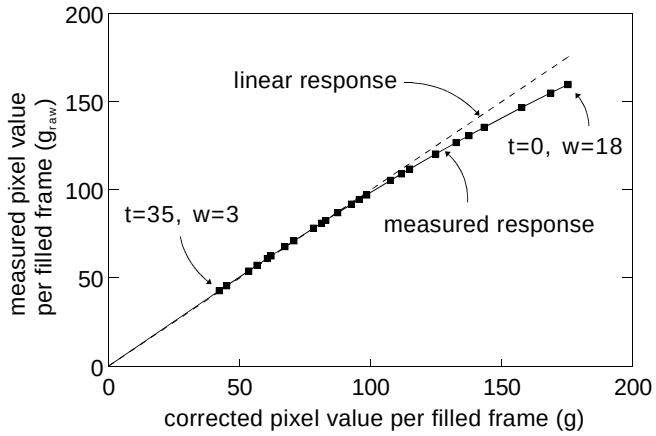

Figure 3.2. The non-linear response of the EPID system; the measured on-axis pixel value per filled frame g_{raw} as function of the corrected pixel value per filled frame g (markers). The solid line represents the response curve of the system as defined by equation (3.2). For comparison, the dashed line shows a perfect linear response. The deviation between the two lines clearly indicates the non-linear response of the system for high portal doses.

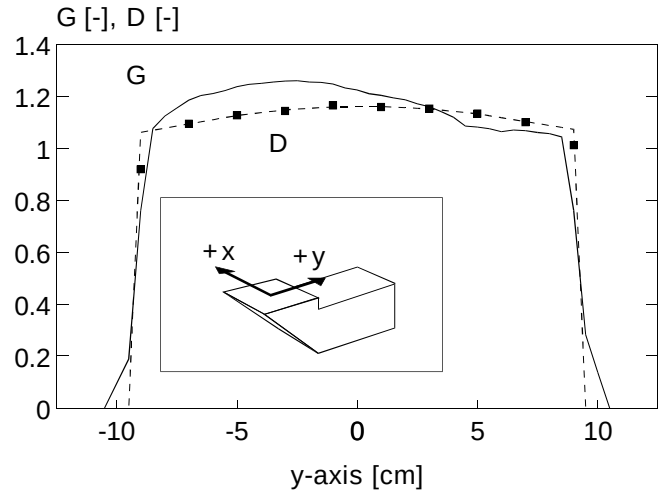

Figure 3.3. The profile along the y-axis of a corrected EPID image (solid line) and the corresponding dose array (markers) for irradiation of a flat, 25 cm thick polystyrene phantom with an 18 $\times$ 18 cm^2 field. Both are normalized to the reference situation ($w \times w$=10 $\times$ 10 cm^2, t=25 cm and L=47.5 cm). The inset shows the orientation of the x- and y-axes relative to the EPID structure.

3.3.1.2 Non-linearity of the electronics

Using the method described in section 3.2.3.2 to correct solely for the non-linear electronics, a_2 and a_3 were found to be -0.00269 and 1.69×10^{-5}, respectively. The dashed lines in figure 3.1 show the ratios of G_{raw} and D_p corrected only for the non-linear electronics. The (systematic) absorber thickness dependencies of the dashed curves are less than those of the corresponding raw data (dotted lines) but not negligible; the maximum standard deviation in the derived ratios as function of thickness is 2.1% for w=3 and the mean of the standard deviations for all field sizes is 1.5%. Hence, the non-linear EPID response is mainly due to non-linear electronics, but a non negligible part is due to differences in spectral sensitivity of the EPID and the ionization chamber.

3.3.2 Derivation of **S***-arrays*

Portal dose measurements for derivation of **S**-arrays were performed at a square grid with distances between neighboring points of 1 cm, except for the two largest fields (16 $\times$ 16 and 18 $\times$ 18 cm^2) for which a 2 cm grid was used. As an example, cross sections through the measured **G** and $\mathbf{D}_p$-arrays for the 18 $\times$ 18 cm^2 field are depicted in figure 3.3. The EPID response increases in the -y direction, for which the distance between the fluorescent screen and the mirror decreases.

Using the procedure described in section 3.2.4, **S**-arrays have been derived from the measured **G**- and $\mathbf{D}_p$-arrays. Cross sections through the **S**-arrays along the x- and y-axes are depicted in figures 3.4a and 3.4b, respectively. Along the x-axis, the **S**-arrays are relatively flat and they demonstrate no field size dependence. Along the y-axis however, S-values increase

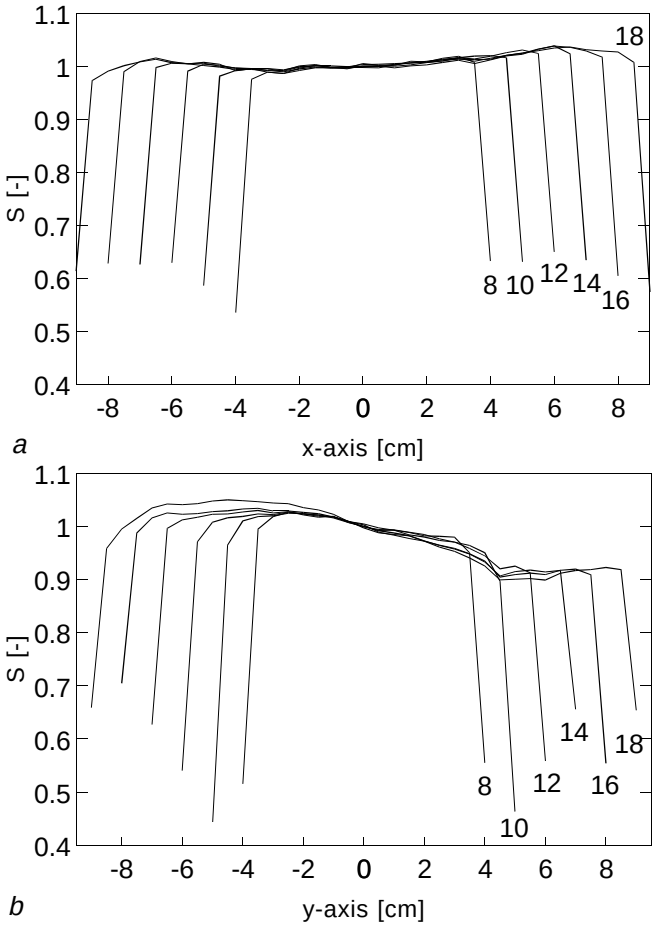

Figure 3.4. Cross sections along the x- (a) and y-axis (b) through the derived **S**-arrays for fields 8×8, 10×10, 12×12, 14×14, 16×16 and 18×18 cm^2.

with decreasing y. Moreover, the **S**-arrays show a field size dependence especially in the -y direction. The kernel $K(r)$, derived from ratios of G and D_p measured at the beam axis, does not exactly describe the "cross talk" in off-axis points. Especially for those points close to the mirror, **S** does not only correct for changes in local EPID sensitivity but also for shortcomings in the kernel.

3.4 Accuracy assessment of PDI measurement with the EPID

The accuracy of the described method for PDI measurement with the EPID has been assessed by comparing PDIs derived from EPID measurements with PDIs measured with the ionization chamber. Measurements were performed for a set of anthropomorphic phantoms irradiated with the 25 MV photon beam of an MM50 racetrack microtron. Furthermore, a flat phantom

was irradiated with an intensity modulated beam produced with dynamic multileaf collimation. Leaf trajectory calculations were performed with an algorithm described by van Santvoort and Heijmen [162] and Dirkx *et al.* [38]

3.4.1 Thorax phantom

The set-up with the thorax phantom is depicted in figure 3.5a. The phantom is made out of cork and lucite and its cross section is constant in cranial-caudal direction. The phantom was irradiated with a 14×12 cm^2 field. The source to surface distance (SSD) was 100 cm and the distance between the exit surface of the phantom and the detector plane was 37.5 cm. The portal dose derived from EPID measurements (using the **S**-array of the 14×14 cm^2 field) show good agreement (0.4 ± 0.7%) with ionization chamber measurements along the x-axis (see figure 3.5b). Similar results were obtained with a 60^o wedge in the beam (figure 3.5c); the observed deviation between the ionization chamber and the EPID measurements is 0.1 ± 0.6%.

3.4.2 Alderson phantom

The Alderson phantom was irradiated in the prostate region with a conformal field (figure 3.6a). The on-axis distance between the exit plane of the phantom and the detector (L) was 48 cm. The percentual differences between the portal dose derived from the EPID image, using the **S**-array of the 12×12 cm^2 field, and portal dose measured with a scanning ionization chamber at a 1 cm grid are depicted in figure 3.6b. The deviation is 0.5 ± 0.8%.

The phantom was also irradiated in the thorax region with a 10×14 cm^2 field (figure 3.6c). The PDI was derived using the **S**-array of the 14×14 cm^2 field. Percentual differences between the ionization chamber measurements and the EPID measurements are shown in figure 3.6d. The deviation is 0.0 ± 0.8%.

3.4.3 Dynamic multileaf collimation

Figure 3.7 shows data for the irradiation of a flat 25 cm thick polystyrene absorber. The distance L between the exit plane of the absorber and the detector was 47.5 cm. Ionization chamber measurements were performed at a 1 cm interval along the y=+0.6 cm and y=-4.4 cm axis. The axes where chosen such that they are not in the 'overlap' region between two adjacent leaf pairs. The solid lines in figure 3.7 represent the EPID dose measurements along both axes, derived using the **S**-array of the 16×16 cm^2 field. The markers represent the corresponding ionization chamber measurements. EPID and ionization chamber measurements agree well, the deviation being -0.4 ± 0.8%.

3.5 Discussion

Using the above described method it is possible to derive absolute portal dose images from EPID images obtained with a Philips SRI-100 EPID in open, wedged and intensity modulated beams (produced with dynamic multileaf collimation) that agree within 1% (1 SD) with ionization chamber measurements. With more than a year's experience with the current characterization

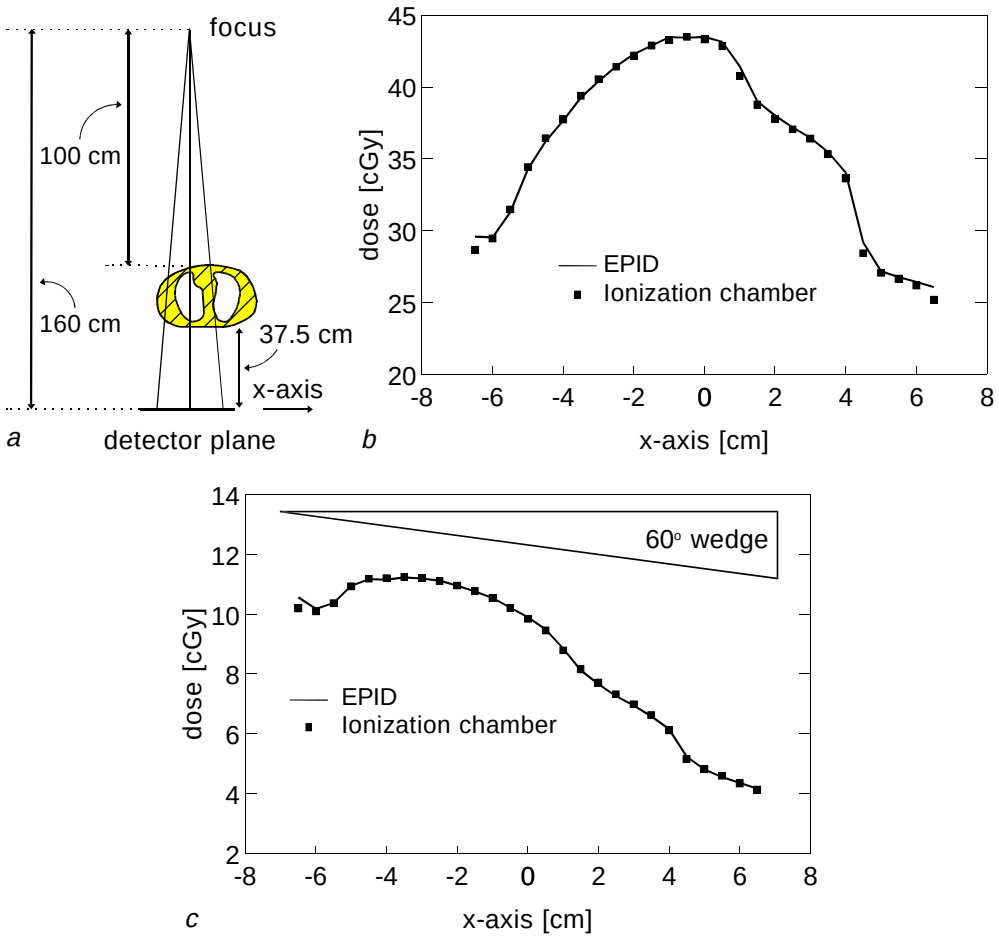

Figure 3.5. Set-up with the thorax phantom (a) used to generate the data for the open (b) and the wedged field (c). The solid lines in (b) and (c) represent portal doses measured with the EPID and the dots are the corresponding ionization chamber measurements.

of our system we have found no evidence that the measurements to determine **K** and **S** have to be repeated. This is in agreement with the observed high stability of the system [61].

The Varian PortalVision liquid-filled matrix ion chamber system is reported to be able to measure the dose rate in open beams with an accuracy of 1% (1 SD) [11]. However, the fastest PortalVision system developed so far has a scan time for acquisition of an image of about 1 s. It is not yet clear how the system can perform dose measurements for dynamic treatments, during which maximum leaf speeds are in the order of 2 cm/s.

A rather complicating feature of the system that was investigated is the non-linear behavior of the complex and somewhat outdated electronics. It is expected that modern CCD camera based systems will not suffer from this problem. At present, a newly developed CCD camera

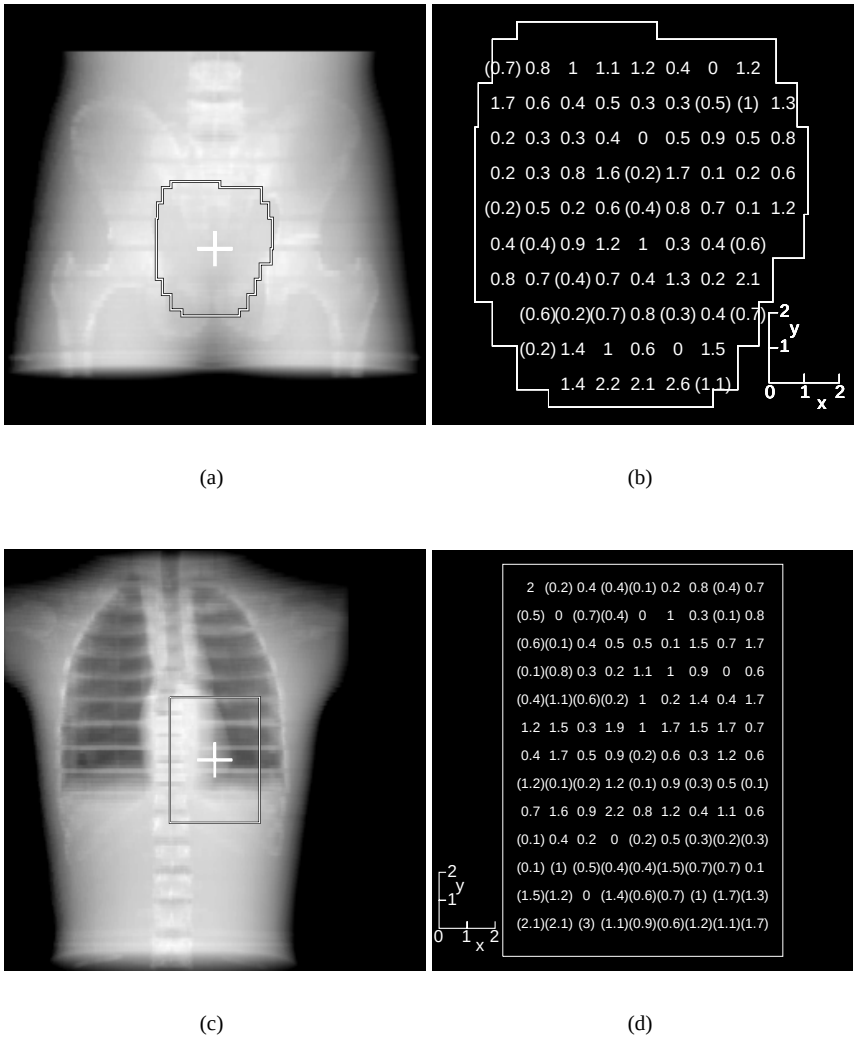

(a) (b)

(c) (d)

Figure 3.6. Digitally reconstructed radiographs (DRRs) of the Alderson phantom with the contours of the applied fields for irradiation in the prostate region (a) and in the thorax region (c). The crosses in the center of each DRR mark the isocenter. Percentual differences between portal doses measured with the scanning ionization chamber at a 1 cm grid and the portal dose measured with the EPID are depicted in (b) for the prostate irradiation and in (d) for the irradiation in the thorax region. Numbers are centered around the measuring point and negative values are in between brackets.

based EPID is being tested in our institute. The main improvements relevant for dosimetric tasks compared to the present system are (i) the increased distance between the mirror and the fluorescent screen, (ii) the use of a modern 10 bit frame grabber and (iii) the simplified electronic coupling between the camera and the frame grabber. Experiments with the SRI-

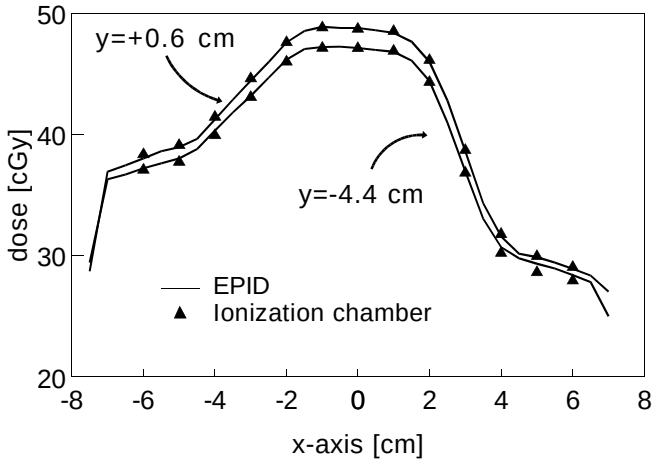

Figure 3.7. Absolute portal doses (cGy) measured in an intensity modulated field along two lines (y=0.6 cm and y=-4.4 cm). A flat, 25 cm thick homogenous polystyrene absorber was in the beam with an exit plane to detector distance L of 47.5 cm. The solid lines represent the EPID measurements and the markers the corresponding doses measured with an ionization chamber.

100 system showed that the higher response in the direction of the mirror decreases when the distance between the mirror and the fluorescent screen is increased by shielding the top edge of the mirror with black carbon paper. At present, the dosimetric characteristics of the new system are being investigated.

Acknowledgments

The authors would like to thank P.R.M. Storchi for providing his FFT-subroutines which where used in our deconvolution program, N. Driver and D. Binnekamp for their help with the RFA-300 water phantom and J. Udo for his help with the experiments. E.B. van Dieren is gratefully acknowledged for providing the DRR-routine used to generate figures 3.6a and 3.6c. This work was financially supported by the Dutch Cancer Society (grants DDHK 94-848 and DDHK 96-1258). The Netherlands Organization for Scientific Research (NWO) is acknowledged for a travel grant.

Chapter 4

Portal dose image prediction for dosimetric treatment verification in radiotherapy I: an algorithm for open beams

K.L. Pasma, B.J.M. Heijmen, M. Kroonwijk and A.G. Visser
Med. Phys. 25(6): 830-840, 1998.

A method is presented for calculation of transmission functions for high energy photon beams through patients. These functions are being used in our clinic for prediction of portal dose images (PDIs) which are compared with PDIs measured with an electronic portal imaging device (EPID). The calculations are based on the planning CT-scan of the patient and on the irradiation geometry as determined in the treatment planning process. For each beam quality, the required input data for the algorithm for transmission prediction are derived from a limited number of measured beam data. The method has been tested for a PDI-plane at 160 cm from the focus, in agreement with the fixed focus-to-detector distance of our fluoroscopic EPIDs. For 6, 23 and 25 MV photon beams good agreement ($\sim$1%) has been found between calculated and measured transmissions through anthropomorphic phantoms.

4.1 Introduction

Three-dimensional (3D) planning systems and modern radiotherapy facilities allow the design and delivery of complex treatment plans. Adequate verification of the correct implementation of sophisticated plans is mandatory. Preferentially, treatment verification should not be restricted to automatic checks with a record and verify system on prescribed treatment unit parameters such as gantry angle and multi-leaf collimator (MLC) settings. Measurements during treatments with thermoluminescent dosimeters (TLDs), diodes, film and electronic portal imaging devices (EPIDs) can provide valuable information on delivered dose distributions and patient set-up [8, 28–30, 43–45, 90, 92, 134].

Several groups have studied the application of EPIDs for dosimetric verification of treatments ('in vivo' dosimetry) [44, 60, 61, 81, 98, 150, 173, 176]. Comparison of PDIs derived from measured portal images with predicted PDIs can reveal problems like incorrect (dosimetric) performance of the treatment unit, erroneous design, production or application of compensators, and deviations between the actual patient anatomy during treatment and the anatomy according to the planning CT-scan, e.g. due to tumor shrinkage or variations in rectum filling [84, 85, 118].

A few groups have developed and tested algorithms for prediction of PDIs. For some inhomogeneous phantoms and a patient, all irradiated with a ^{60}Co beam, Wong *et al.* [172] and Ying *et al.* [175] have compared predicted PDIs, calculated with the delta volume method, with PDIs measured with film, TLD and a scanning ionization chamber. PDIs were predicted and measured in the plane immediately behind the phantoms and the patient. In clinical practice it is often quite unpractical, and for some EPIDs even impossible, to position the EPID detector plane immediately behind the patient. The delta volume method is not suitable to predict PDIs in case of a large air gap between the patient and the EPID [99]. McNutt *et al.* reported how they used the convolution/superposition method, based on precalculated Monte Carlo data, to predict the dose throughout an extended volume which includes a phantom and an EPID, irradiated by a 6 MV photon beam [99]. The calculated dose distribution in the EPID was then extracted and compared with a PDI measured with an EPID. They used distances between the exit plane of the phantoms and the detector of 11 and 22 cm. In the central part of the fields the calculated PDIs generally agreed within 4% with measurements.

In our institute Philips SRI-100 EPIDs are used for treatment verification. The fluorescent screen is positioned at a fixed distance of 160 cm from the focus. In clinical practice the distance between the exit plane of the patient and the fluorescent screen ranges from 30 to 50 cm. Photon beams of upto 25 MV are used. In the literature there are no methods for PDI prediction available which have been tested for air gaps larger than 22 cm and energies above 6 MV. The aim of the work presented in this paper was to develop an accurate ($\sim$2%) algorithm for PDI prediction for these situations based on limited set of measured input data.

We use the following equation for prediction of PDIs

$$D_p(x, y) = T(x, y) \cdot D_{p,0}(x, y), \tag{4.1}$$

with $D_p(x, y)$ the portal dose in point (x, y) of the PDI, $T(x, y)$ a transmission function and $D_{p,0}(x, y)$ the portal dose that would have occurred in (x, y) in the absence of the patient. In this paper we focus on the algorithm that was developed for calculation of transmission functions $T(x, y)$ (as defined by equation (4.1)) for open (non-wedged) beams. For the calculation of the dose distributions $D_{p,0}(x, y)$ in the detector plane of the EPID, needed for prediction of

PDIs with equation (4.1), we have slightly modified an algorithm that was developed in our institute for dose calculations in water phantoms [141, 142].

The portal dose in each point (x, y) of the PDI consists of a primary contribution, due to photons that arrive in (x, y) without interacting with the patient, and a scatter contribution that stems from photons generated in interactions in the patient. In the presented method for $T(x, y)$ prediction, primary and scatter contributions are dealt with separately as was proposed by Cunningham for dose calculations inside patients [32]. The planning CT-data of the patient and the treatment parameters such as the gantry angle and MLC-settings for all fields are used as input for the calculations. The off-axis spectral shift in high energy photon beams and the non-exponential attenuation of these beams in absorbers is taken into account. For each beam quality, $T(x, y)$-predictions are based on a data set derived from measured on- and off-axis transmissions through flat water equivalent absorbers and a dose profile measured in a large field without an absorber in the beam. The method has been implemented and tested for a PDI-plane at 160 cm from the focus. Predicted transmissions of 6, 23 and 25 MV photon beams through anthropomorphic phantoms, with exit plane to detector distances of 37.5 to 50 cm have been compared with measurements. Preliminary results of the algorithm for $T(x, y)$-prediction have been reported by Heijmen *et al.* [64].

The presented work is part of a project to study the use of SRI-100 EPIDs for dosimetric applications. We have investigated the characteristics of this EPID relevant for accurate and reproducible dose measurements in a 6 MV photon beam [61] and we have developed a method to derive PDIs from measured EPID images [116, 125]. Dirkx *et al.* have applied this EPID for accurate daily dosimetric quality control of the 25 MV photon beam of a MM50 racetrack microtron [39]. The developed methods for prediction (as described in this paper) and measurement of PDIs have been tested for a group of 10 prostate cancer patients. The difference between the average on-axis measured portal dose and the predicted portal dose was $0.3 \pm 2.1\%$ for the lateral field and $0.7 \pm 3.4\%$ for the anterior field. For some patients localized off-axis differences of upto 15% were found between predicted portal doses and portal doses measured with the EPID during some of the treatment fractions. The observed large differences pointed at variations in internal patient anatomy ('internal organ motion') due to variations in rectum filling; for some patients the anatomy during the registration of the planning CT-scan did not reflect the average anatomy during the daily treatments [84, 85].

In this paper, field sizes, coordinates and distances to the beam axis are all defined in the plane through the isocenter (i.e. at 100 cm from the focus). The subscript 'open' refers to a non-wedged beam.

4.2 The method of transmission prediction

As stated above the primary- and scatter components, $T^P(x, y)$ and $T^S(x, y)$, of the transmission $T(x, y)$ are calculated separately and subsequently added, i.e.

$$T(x, y) = T^P(x, y) + T^S(x, y). \tag{4.2A}$$

$T^P(x, y)$ and $T^S(x, y)$ are defined by

$$T^P(x, y) = \frac{D_p^P(x, y)}{D_{p,0}(x, y)} \tag{4.2B}$$

and

$$T^S(x, y) = \frac{D_p^S(x, y)}{D_{p,0}(x, y)}, \tag{4.2C}$$

with $D_p^P(x, y)$ the portal dose in point (x, y) of the PDI due to primary photons, $D_p^S(x, y)$ the portal dose in (x, y) due to scattered radiation and $D_{p,0}(x, y)$ the portal dose that would have occurred in (x, y) in the absence of the patient.

The algorithms for the calculation of $T^P(x, y)$ and $T^S(x, y)$ for patients are based on data derived from measured transmissions through flat, water equivalent (polystyrene) phantoms (see section 4.3). To be able to use these data for the prediction of the transmission through an (inhomogeneous) patient, the patient anatomy as described by the planning CT-scan is substituted by an (imaginary) equivalent homogeneous phantom (EHP) consisting of polystyrene. For each treatment beam, a separate EHP is calculated. For each ray line, the patient and the EHP have equal (equivalent) polystyrene thicknesses and equal distances between the center of mass and the detector plane. An EHP is thus defined by two two-dimensional arrays, one with polystyrene thicknesses $t_{(x,y)}$ and the other with distances $L_{(x,y)}$ between the exit point of the EHP and the detector plane. In figure 4.1 an example is given for an irradiation of a thorax phantom with an anterior field in a 6 MV beam (see section 4.4 for details).

In the first step of the derivation of an EHP a ray tracing algorithm is used that derives the water equivalent thicknesses (t_{H_2O}) of the patient along all ray lines in the treatment field. Each CT-slice contains 256×256 pixels of typically 0.2×0.2 cm^2 (the precise pixel size depends on the size of the body contour of the patient), the inter slice thickness is 0.5 cm. For each CT-voxel the algorithm uses nearest neighbor sampling to determine the corresponding Hounsfield unit (HU) [137]. For HU-values below 1100 an electron density relative to water of HU/1000 is assumed; higher values are converted using $0.54 \times \text{HU}/1000 + 0.51$ (these coefficients are for a Siemens somaton plus CT-unit). Finally, the derived water equivalent thicknesses are converted to polystyrene (PS) thicknesses using $t_{PS} = t_{H_2O}\ \mu_{H_2O}/\mu_{PS}$, with μ_{PS} and μ_{H_2O} linear attenuation coefficients (m^{-1}) for the effective beam energy [78], which is assumed to be a third of the nominal beam energy.

4.2.1 Calculation of the primary component $T^P(x, y)$

For an EHP, the primary component of the transmission in point (x, y) of the PDI, positioned at a distance $r_{(x,y)} = \sqrt{x^2 + y^2}$ from the beam axis, and corresponding to the thickness $t_{(x,y)}$ of the EHP along the ray line through point (x, y) (see also figure 4.1) is calculated using

$$T^P(x, y) = C_{\text{open}}(r_{(x,y)}, t_{(x,y)}) \cdot P(t_{(x,y)}), \tag{4.3}$$

with $P(t_{(x,y)})$ the *on*-axis primary transmission component for irradiation of a flat, polystyrene phantom with thickness $t_{(x,y)}$, and $C_{\text{open}}(r_{(x,y)}, t_{(x,y)})$ a function to account for the difference in penetrating beam quality between the beam axis and the *off*-axis point (x, y). This difference is due to the off-axis shift in beam spectrum. Since a clinical photon beam is not monoenergetic, C_{open} does also depend on the phantom thickness. As $T^P(x, y)$ is related to primary radiation (i.e. photons that have not interacted in the patient), it does not depend on $L_{(x,y)}$. The derivation of functions $P(t)$ and $C_{\text{open}}(r, t)$ from measured input data is explained in sections 4.3.3.1 and 4.3.4.

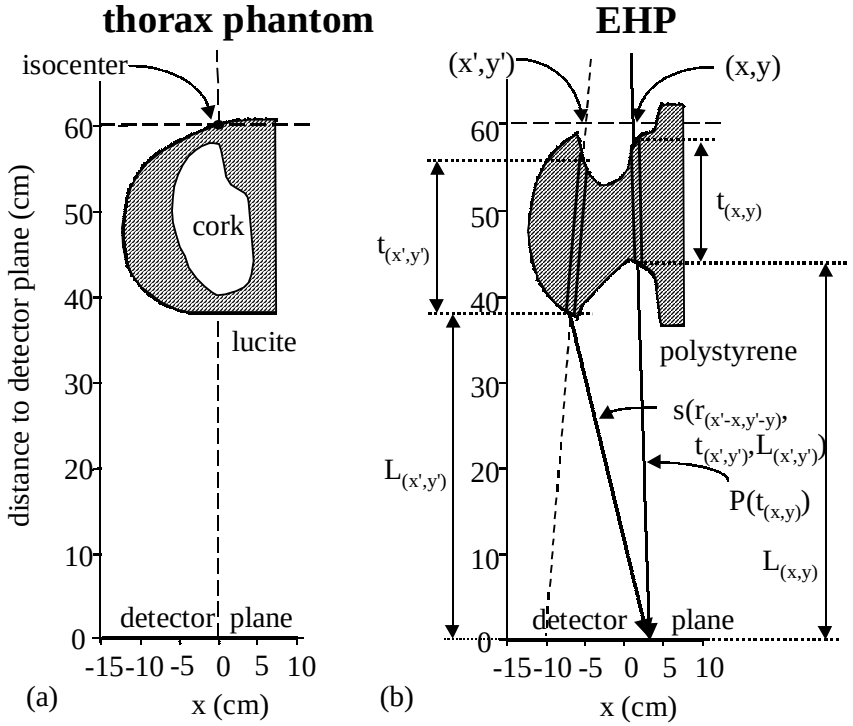

Figure 4.1. (a) Set-up for irradiation of a thorax phantom with an anterior field and (b) the set-up for the corresponding equivalent homogeneous phantom (EHP), used for calculation of the transmission through the thorax phantom. Both the thorax phantom and the EHP have a constant cross section in cranial-caudal direction. $s(r_{(x'-x,y'-y)},t_{(x',y')},L_{(x',y')})$ and $P(t_{(x,y)})$ in (b) are explained in sections 4.2.1 and 4.2.2.

4.2.2 Calculation of the scatter component $T^S(x, y)$

The scatter component of the transmission through an EHP in point (x, y) of the PDI, $T^S(x, y)$, is calculated using rotation symmetric scatter kernels $s(r, t, L)$. For a flat, polystyrene phantom with a thickness t, positioned at a distance L from the PDI-plane, $s(r, t, L)$ is the contribution to the *on*-axis transmission from photons scattered from an imaginary *off*-axis phantom column defined by a ray line at a distance r from the beam axis, per unit of normalized incoming beam fluence $f(r)$ and column cross section (see figure 4.2). The derivation of $f(r)$ and $s(r, t, L)$ from measured data is described in sections 4.3.2 and 4.3.3.2.

The following equation is used for the calculation of $T^S(x, y)$ for an EHP:

$$T^S(x, y) = \int_{(x',\ y')\,\epsilon\ \text{field}} \frac{f(r_{(x',y')})}{f(r_{(x,y)})}\, s(r_{(x'-x,y'-y)}, t_{(x',y')}, L_{(x',y')})\, dx'\, dy', \qquad (4.4)$$

with $s(r_{(x'-x,y'-y)}, t_{(x',y')}, L_{(x',y')})$ the scatter contribution due to the imaginary EHP-column connected to the ray line through (x', y'), with thickness $t_{(x',y')}$ and absorber-to-detector-distance $L_{(x',y')}$, to the total transmission at point (x, y), per unit of incoming beam fluence

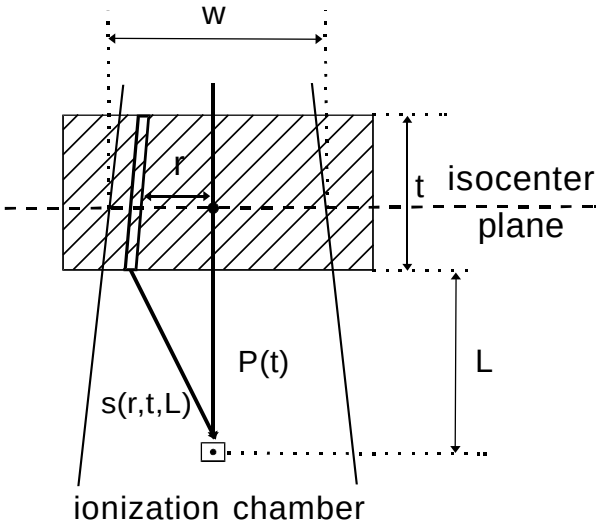

Figure 4.2. Set-up for measurement of beam data used to derive the required input data for the algorithm for transmission prediction. The absorber is made of polystyrene. The scatter kernels $s(r, t, L)$ and the primary contribution $P(t)$, defined in sections 4.2.1 and 4.2.2, are examples of derived input data.

at point (x', y'), $f(r_{(x',y')})$, and EHP-column cross section $(dx'\,dy')$. See figure 4.1 for an example.

Equation (4.4) has been derived from its definition (equation (4.2C)), assuming that (i) the scatter kernels $s(r, t, L)$, describing scatter contributions to the beam axis, can also be used for calculation of scatter contributions to off-axis points, (ii) the scatter kernels $s(r, t, L)$, derived from measured transmissions through flat phantoms, can be used for curved EHPs and (iii) beam penumbras in the PDI-plane, both with the patient in the beam and in the absence of the patient are equal.

4.3 Derivation from measured input data of the functions $f(r)$, $P(t)$, $s(r, t, L)$ and $C_{\text{open}}(r, t)$, used for transmission prediction

The functions $f(r)$, $P(t)$, $s(r, t, L)$ and $C_{\text{open}}(r, t)$ are derived from (i) a dose profile measured along the diagonal of the largest square field without absorber in the beam and (ii) measured on- and off-axis transmissions of the beam through flat, polystyrene phantoms. Examples are given for the 6 MV photon beam of a Siemens KD-2 linac.

4.3.1 Experimental setup for measurement of input data

The experimental set-up for measurement of the required input data is depicted in figure 4.2. Dose measurements are performed with a PTW ionization chamber (N31002), positioned in a polystyrene mini phantom with a transversal cross section of 7×7 cm^2 and a thickness of 5 cm. The short term reproducibility of the dose measurements is 0.2%. The center of the

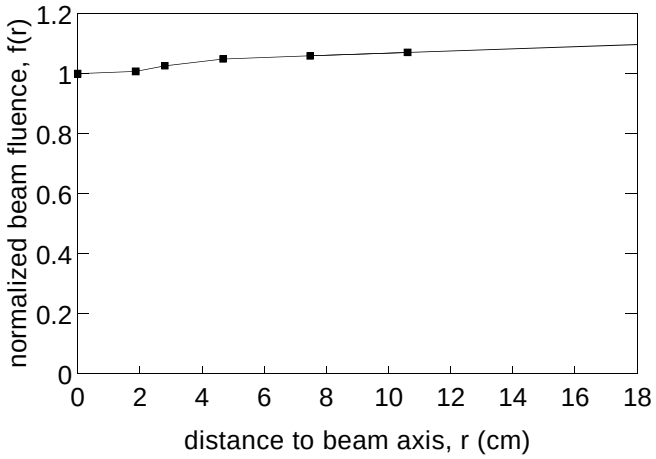

Figure 4.3. Normalized fluence profile $f(r)$ of a 6 MV beam.

ionization chamber is positioned at a distance of 160 cm from the focus, which is equal to the fixed focus-to-fluorescent screen distance of our EPID. The depth of the ionization chamber in the mini phantom is equal to the (effective) water equivalent depth of the fluorescent screen of the EPID. This effective depth is defined as the depth of the ionization chamber for which the variations in on-axis response of the EPID ((grey scale value measured with the EPID)/(portal dose measured with the ionization chamber)) for various thicknesses and exit plane-to-detector distances L of flat absorbers are minimal [116]. To reduce the detection of electrons generated in the patient when irradiated with high energy photon beams, we have mounted an additional 1 mm thick stainless steel slab on top of the standard fluorescent screen of the EPID [125]. Image quality is hardly affected by this additional layer so that acquired images can be used for patient setup verification and portal dose verification at the same time [84, 85]. The effective water equivalent depth of the in total 2.65 mm thick stainless steel layer is 2.5 cm for the 25 MV photon beam.

For off-axis measurements, the mini phantom with the ionization chamber inserted, is scanned in an empty RFA-300 water phantom (Scanditronix Medical AB).

4.3.2 Derivation of the normalized incoming beam fluence profile $f(r)$

The dose profile, measured along the diagonal of the largest field without absorber in the beam, is used to derive the normalized incoming beam fluence profile $f(r)$ with r the distance to the beam axis. Assuming radial symmetry, $f(r)$ is constructed by replacing the penumbras of the measured dose profile by a linear extrapolation of the remaining central part of the dose profile. The extrapolation is performed upto 18 cm, which is the distance between the beam axis and the corner of a 25×25 cm^2 field. An example is given in figure 4.3.

4.3.3 On-axis transmissions $T(w, t, L)$ through flat, polystyrene phantoms

On-axis primary contributions $P(t)$ and scatter kernels $s(r, t, L)$ defined in, respectively, sections 4.2.1 and 4.2.2, are derived from measured on-axis transmissions through flat, polystyrene absorbers. Transmissions are measured for a set of square $w \times w$ fields, absorber thicknesses t and distances L from the exit plane of the absorber to the detector plane (see also figure 4.2). The absorbers consist of piled polystyrene slabs of $40 \times 40 \times 1$ cm^3. The $T(w, t, L)$-set that was measured for the 6 MV beam contains the transmissions for all combinations of

w = 3, 4, 5, 6, 8, 10, 12, 15, 20, 25 cm,
t = 5, 10, 15, 20, 25, 30 cm and
L = 40, 45, 50, 55 cm.

Note that also some clinically irrelevant w, t, L-combinations (e.g. t=5 cm, L=40 cm) are included; they have been measured to get a better understanding of the behavior of the primary and scatter contributions, also in extreme cases.

Irradiations were performed with 150 monitor units (MU). To reduce the effect of (small) output fluctuations of the linac on the measured transmissions, for each w, L-combination the time interval between the dose measurements with and without absorber was kept limited. For L=50 cm, the measured transmissions are presented in figure 4.4a.

4.3.3.1 Derivation of on-axis primary contributions $P(t)$ from measured transmissions $T(w, t, L)$

The contribution of scattered photons to the measured on-axis transmissions reduces to zero for an infinitely small field. To estimate the on-axis primary contributions $P(t)$, for all t, L-combinations, the curves $T(w^2, t, L)$, as presented for L=50 cm in figure 4.4a, are linearly extrapolated to w^2=0, using a least square fit through the measured data points for w^2 = 9, 16 and 25 cm^2, yielding extrapolated transmissions $T(w^2 = 0, t, L)$. Next, for each thickness t, the extrapolated transmissions $T(w^2 = 0, t, L)$ for all L are averaged, yielding the primary contribution $P(t)$. For all beam qualities and phantom thicknesses t, the observed standard deviation in derived extrapolated transmissions $T(w^2 = 0, t, L)$ for a range of distances L was generally below 0.3% and no systematic L-dependence was observed. This is in agreement with the behavior of primary radiation. For the 6 MV beam, data are presented in Table 4.1. In figure 4.4b, the logarithm of $P(t)$ is presented as a solid line. The dashed line is the extrapolation of the line through the data points for t=0 and t=5 cm. The deviation between the solid and dashed lines for larger thicknesses is due to the non-exponential attenuation of the non-monoenergetic beam.

Because extrapolated transmissions $T(w^2$=0,t,L) do not depend on L, in clinical practice, the measurement of transmissions for the 3×3 and 4×4 cm^2 fields can be limited to L=50 cm, yielding a reduction in the number of w, t, L-combinations mentioned above.

4.3.3.2 Derivation of scatter kernels $s(r, t, L)$

The total scatter contributions $S(w, t, L)$ to the measured on-axis transmissions $T(w, t, L)$ are used to derive the scatter kernels $s(r, t, L)$, defined in section 4.2.2. The $S(w, t, L)$-functions are obtained using $S(w, t, L) = T(w, t, L) - P(t)$. $S(w, t, L = 50\ cm)$-functions derived

Table 4.1. Extrapolated transmissions $T(w^2 = 0, t, L)$. The last two columns show, respectively, $P(t)$, as derived by averaging all $T(w^2 = 0, t, L)$-data for each t, and the standard deviation therein.

	L [cm]					
	40	45	50	55		
t [cm]		$T(w^2 = 0, t, L)$			$P(t)$	SD
5	0.7812	0.7800	0.7805	0.7801	0.7804	0.0005
10	0.6139	0.6141	0.6141	0.6139	0.6140	0.0001
15	0.4872	0.4867	0.4867	0.4863	0.4867	0.0003
20	0.3887	0.3880	0.3884	0.3883	0.3883	0.0003
25	0.3119	0.3115	0.3117	0.3114	0.3116	0.0002
30	0.2514	0.2512	0.2513	0.2512	0.2513	0.0001

from figures 4.4a and 4.4b are presented in figure 4.4c. Note that in this figure the scatter contribution is maximum for t=15 cm. This observation is in agreement with the Monte Carlo results published by Jaffray *et al.* [74].

For each t, L-combination, a corresponding scatter kernel $s(r, t, L)$ is derived such that it obeys the following equation for each field $w \times w$:

$$S(w, t, L) = \int_{(x', y') \,\epsilon\, w \times w} f(r_{(x', y')})\, s(r_{(x', y')}, t, L)\, dx'\, dy' \tag{4.5}$$

The integral on the right hand side of equation (4.5) equals the expression of equation (4.4) for the on-axis scatter contribution $T^S(0, 0)$ for a flat polystyrene absorber with a thickness t, positioned at a distance L from the PDI-plane.

The algorithm that is applied for derivation of scatter kernels $s(r, t, L)$ that obey equation (4.5) for each measured field $w \times w$ is described in Appendix A. This algorithm is similar to the method of Storchi and Woudstra to derive scatter kernels for dose calculations inside water phantoms [142]. However, several improvements were made e.g. to avoid non-physical, negative scatter contributions. The scatter kernels corresponding to the $S(w, t, L = 50)$ functions in figure 4.4c are depicted in figure 4.4d. The kink in the kernels around r=2.25 cm is due to a twist in the $S(w^2, t, L)$-curve at w=3 cm; for smaller fields there is no measured data available and therefore the values are derived using a linear interpolation. No effort has been made to smooth the kernels since the fluctuations average out in calculations of $T^S(x, y)$ with equation (4.4).

4.3.4 Derivation of functions $C_{\text{open}}(r, t)$

The functions $C_{\text{open}}(r, t)$, used in equation (4.3) for calculation of primary contributions to the transmission through an EHP, describing the off-axis change in penetrating quality of the beam are calculated using $C_{\text{open}}(r, t) = P(r, t)/P(t)$ with $P(t)$ and $P(r, t)$ primary contributions to, respectively, on- and off-axis transmissions through flat, polystyrene phantoms of thicknesses t. Derivation of the required function $P(t)$ is described in section 4.3.3.1. Off-axis primary contributions $P(r, t)$, needed for calculation of $C_{\text{open}}(r, t)$, are determined using $P(r, t) = T(r, a \times b, t, L) - T^S(r, a \times b, t, L)$ with $T(r, a \times b, t, L)$ a measured off-axis transmission in

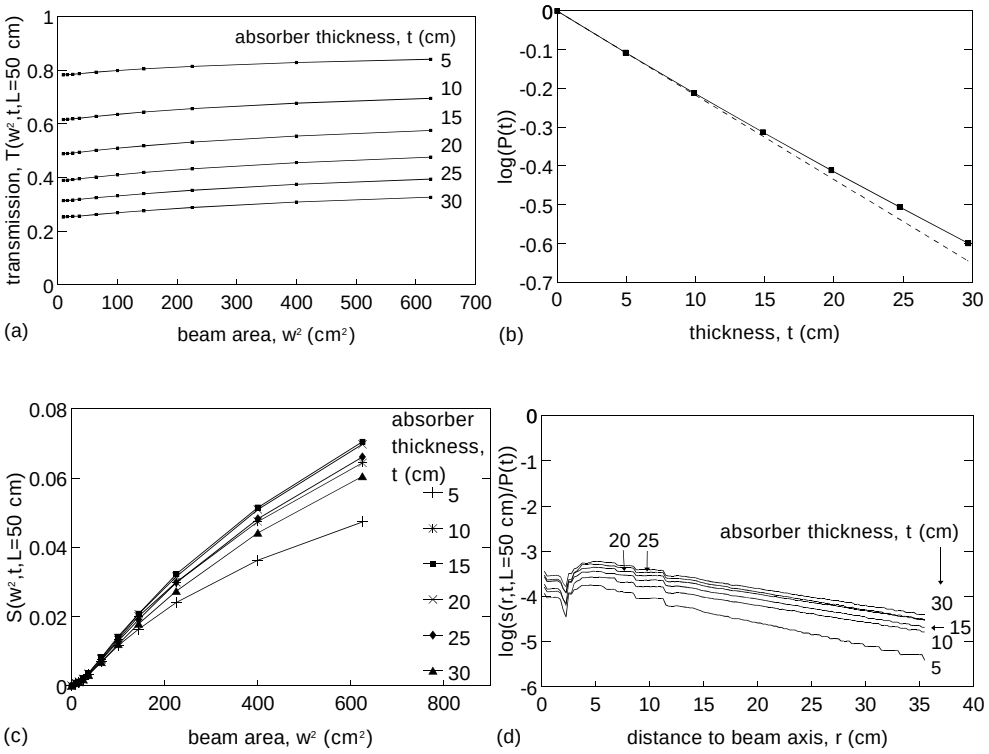

Figure 4.4. Measured on-axis transmissions $T(w^2, t, L$=50 cm) of a 6 MV beam through flat, polystyrene absorbers and derived primary and scatter contributions. Extrapolation of the measured transmission functions depicted in (a) to w^2=0 yields the primary contribution $P(t)$ in (b) (continuous line). The deviation between $P(t)$ and the dashed line demonstrates the non-exponential attenuation of the beam. The scatter functions $S(w^2, t, L$=50 cm) in (c) have been derived with $S(w^2, t, L = 50 \text{ cm}) = T(w^2, t, L = 50 \text{ cm}) - P(t)$. The derivation of the scatter kernels s(r,t,L=50 cm) in (d) from the $S(w, t, L = 50$ cm)-data in (c) is explained in section 4.3.3.2

a rectangular field $a \times b$ and $T^S(r, a \times b, t, L)$ the corresponding scatter contribution calculated with equation (4.4).

As primary contributions do not depend on L (see sections 4.2.1 and 4.3.3.1), $C_{\text{open}}(r, t)$-functions are derived from transmissions measured for only one L. Furthermore, the derivation of the $C_{\text{open}}(r, t)$-functions can be performed with measured off-axis transmissions of only one large field. However, for noise reduction we have combined data measured for three fields: 20×8, 20×14 and 20×20 cm^2. For those fields, measurements were performed at off-axis points x=2, 4 and 8 cm, for absorber thicknesses 5, 10, 20 en 30 cm and a fixed exit plane to detector distance of 50 cm. Derived $C_{\text{open}}(r, t)$-functions are depicted in figure 4.5. The observed decrease in penetrating quality of the beam with increasing off-axis distance is due to the shape of the flattening filter and the off-axis spectral shift. For all r, t-combinations, the

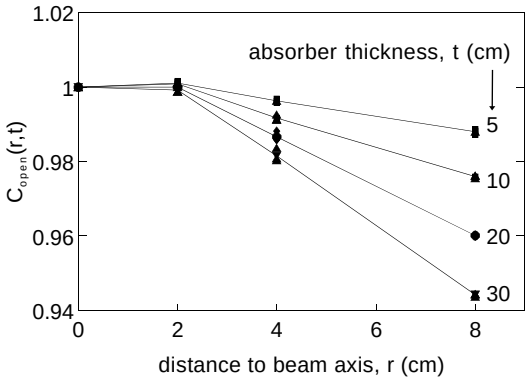

Figure 4.5. Functions $C_{\text{open}}(r, t)$ (lines) describing the off-axis decrease in penetrating quality of the 6 MV beam. The dots represent the derived value of $C_{\text{open}}(r, t)$ for each field size.

Table 4.2. $P(r, t)$-values obtained by extrapolation to field size zero of measured transmissions for square fields $w^2 = 3 \times 3$, 4×4 and 5×5 cm^2 centered around off-axis points r=5 and r=10 cm, and $P(r, t)$-values calculated using $P(r, t)$=$T(r, a \times b, t, L)$-$T^S(r, a \times b, t, L)$. All data are for a 23 MV beam.

	r=5 cm			r=10 cm		
t [cm]	$P(r, t)$ extrapolated	$P(r, t)$ calculated	Diff. [%]	$P(r, t)$ extrapolated	$P(r, t)$ calculated	Diff. [%]
10	0.7373	0.7373	0.0	0.7263	0.7278	-0.2
15	0.6359	0.6361	-0.0	0.6238	0.6244	-0.1
20	0.5505	0.5500	0.1	0.5372	0.5369	0.1

standard deviation in the $C_{\text{open}}(r, t)$-values derived from measured data from different fields $a \times b$ was generally less than 0.1%.

For the 23 MV beam of a Siemens KD-2 linac, the above described method for generation of off-axis primary contributions, $P(r, t)$, used for derivation of the functions $C_{\text{open}}(r, t)$, has been compared with an alternative method which is similar to that used for generation of the on-axis function $P(t)$ (see section 4.3.3.1). Each alternative $P(r, t)$-value is obtained by extrapolation to field size zero of measured transmissions for square fields $w^2 = 3 \times 3$, 4×4 and 5×5 cm^2 centered around the off-axis point r. Data are presented in Table 4.2. For points up to 10 cm from the beam axis, the maximum deviation between these alternative primary contributions and those derived with the method described above was only 0.2%.

4.4 Comparison of predicted and measured transmissions for anthropomorphic phantoms

The accuracy of the method for transmission prediction (described in section 4.2) has been assessed by comparing predictions with ionization chamber measurements for a large set of anthropomorphic phantoms. The setup for the measurements is described in section 4.3.1. The ionization chamber was used since it is the gold standard for dose measurements. A method for accurate dose measurement with our EPID has been presented elsewhere [116, 125]. Predictions were performed at a 0.25 cm grid using equation (4.3) for the primary component and equation (4.4) for the scatter component. In this section, representative data are presented for irradiations with the 6 and 23 MV photon beams of a Siemens KD-2 linac. The anthropomorphic phantoms consist of polystyrene, lucite and cork. Therefore the calculation of EHPs is somewhat different from the applied procedure for patients that is described in section 4.2. The geometrical thicknesses of these materials along the ray lines are derived from CT-data and then converted to water equivalent thicknesses, using μ/μ_{H_2O} ratios for the effective beam energy (2 MeV and 7.6 MeV for the 6 and 23 MV photon beam respectively). As for patients the water equivalent thicknesses are then converted to polystyrene thicknesses, yielding the EHP. The μ/μ_{H_2O} ratios for lucite and polystyrene are respectively 1.137 and 1.018 for the 6 MV photon beam and 1.117 and 0.987 for the 23 MV photon beam [79]. Since no accurate data for cork was available, 0.3 was used for both energies, in agreement with the electron density relative to water according to the CT-scanner. The reported percent differences between predicted and measured PDIs are defined by (calculation-measurement)/measurement $\times$ 100.

The thorax phantom depicted in figure 4.6a, made out of cork and lucite, is symmetric in cranial-caudal direction. This phantom was irradiated by a 14×12 cm^2 field with the 6 and 23 MV photon beams. The source to surface distance (SSD) was 100 cm and the distance between the exit surface of the phantom and the detector plane was 37.5 cm. The EHP for transmission prediction for a 6 MV beam is shown in figure 4.1. Measured and predicted transmissions with the primary and scatter components are depicted in figure 4.6b. The solid lines represent the predicted transmissions and the squares the measurements. The percent differences are depicted in figure 4.6c. The observed agreement, except for the point on the steep gradient (x=3.7 cm), is 0.4 ± 0.4% for the 6 MV beam and 0.3 ± 0.7% for the 23 MV beam.

A second thorax phantom, made out of polystyrene and cork and symmetric in cranial-caudal direction, was irradiated with a lateral 20×20 cm^2 field of the 6 MV photon beam. The setup is depicted in figure 4.7a. The distance between the exit surface of the phantom and the detector plane was 45 cm. Measurements and predictions are depicted in figure 4.7b. Excluding the points on the steep gradients (x=-6.9, -6.3, -5.6, -2.5 and -1.9 cm), the observed agreement between measured and predicted transmissions is 0.2 ± 1.0%. Note that in figure 4.7b the predicted and measured transmissions for $-10 < x < -7$ are slightly higher than 1. The incoming (primary) photon beam reaching this part of the detector plane has not passed any phantom material. Therefore, the primary component of the transmission is 1; side scatter from the phantom yields a total transmission higher than 1.

The head and neck phantom depicted in figure 4.8, made of polystyrene with an air gap of 4×4 cm^2, has a constant cross section in the lateral direction. This phantom was irradiated with an anterior, 16×10 cm^2 field of the 6 MV photon beam. The SSD was 100 cm and the

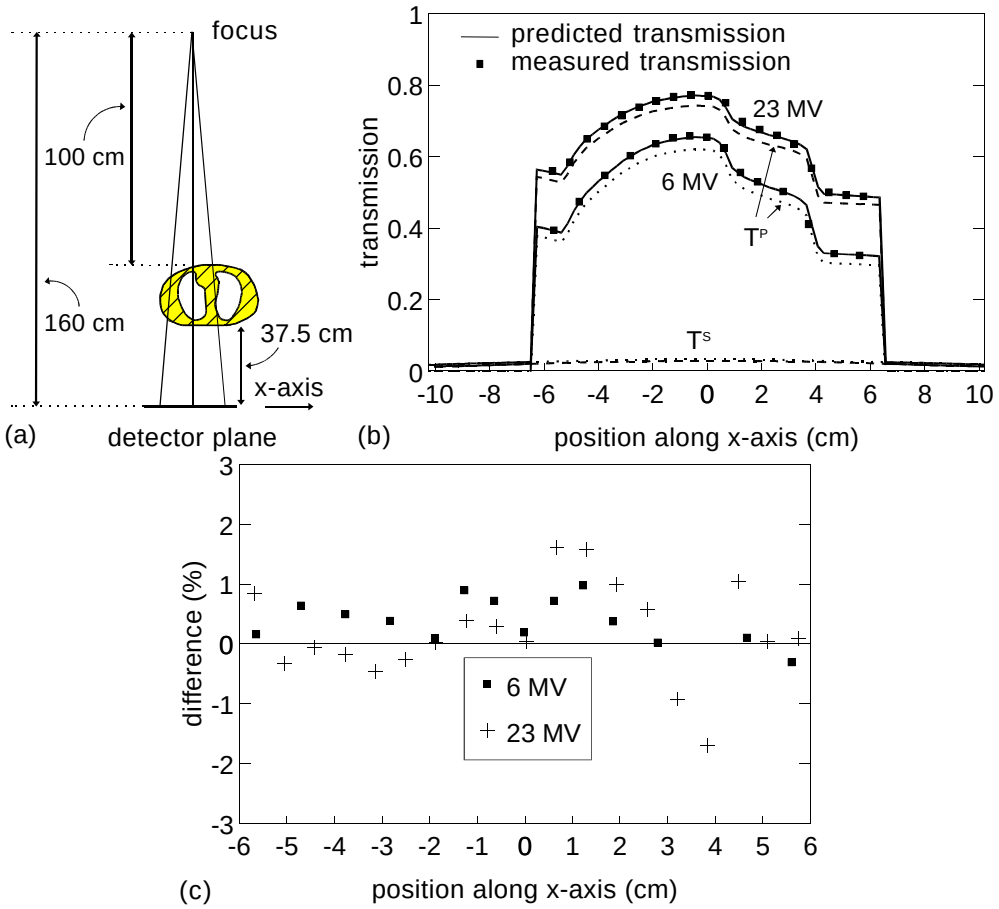

Figure 4.6. (a) Schematic picture of the setup for irradiation of a thorax phantom with the 14×12 cm^2 field of the 6 and 23 MV beams. (b) The markers represent measured transmissions. Continuous lines show the calculated transmissions. The percent difference between the measurements and calculations are depicted in (c).

on-axis distance between the exit surface of the phantom and the detector plane was 44 cm. The squares and the solid line in figure 4.8 are, respectively, measured and predicted transmissions. The upper dashed curve is the calculated primary component and the lower dashed curve the calculated scatter component. Outside the points in areas with steep gradients ($x = -1.3$, 1.9 and 5.7 cm) measured and predicted transmissions agree within $0.3 \pm 0.8\%$.

The calculated on-axis scatter contribution $T^S(0,0)$ depicted in figures 4.6b, 4.7b and 4.8 often significantly differ from off-axis scatter contributions. Assuming off-axis scatter contributions to be equal to the on-axis scatter contribution may lead to systematic errors in predicted off-axis transmissions of up to 3%. Hansen *et al.* have applied a simple model for the on-axis scatter contribution to estimate off-axis scatter contributions. They claim an acceptable accuracy of this approach which is attributed to the large (2 m) distance between the focus and

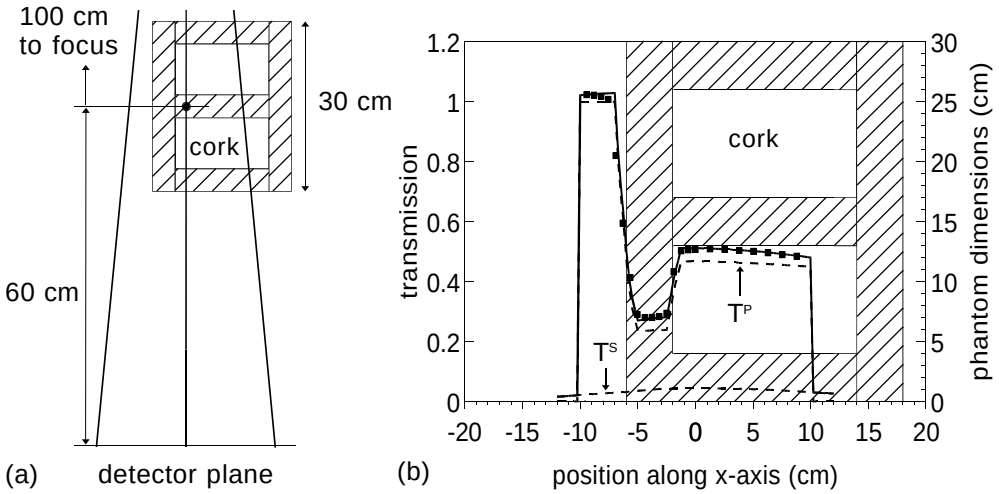

Figure 4.7. (a) Schematic picture of a thorax phantom irradiated with a lateral 20×20 cm^2 field of the 6 MV beam. (b) The predicted transmission is represented by a solid line and the measured transmission with markers. The upper and lower dashed lines represent the primary and scatter component of the calculated transmission.

the EPID [60].

4.5 Discussion

In clinical practice it is convenient to have a large clearance between the treatment head of the accelerator and the EPID. EPIDs are generally positioned at a distance between 150 and 200 cm from the focus [44, 60]. Our SRI-100 EPIDs are positioned at 160 cm from the focus. Due to the resulting relatively large air gap between irradiated patients and the fluorescent screen of the EPID, our treatment planning system cannot be used for the accurate prediction of PDIs, needed for dosimetric treatment verification. This was the main motivation to implement a separate algorithm for PDI-prediction. Our preference to have a dosimetric treatment verification that is independent from our commercial treatment planning system was an additional reason for starting up the project. In the literature there are no methods for PDI prediction available which have been tested for air gaps larger than 22 cm and energies above 6 MV. The work presented in this paper covers these situations.

For each photon beam, the input for the algorithm for PDI prediction is completely derived from a set of measured beam data. Our treatment planning system is also fully based on basic measured input data such as dept dose curves and beam profiles [141, 142]; precalculation of input data using Monte Carlo codes is not required. This was a reason why we preferred to develop a method for PDI prediction that did not force us to start working with Monte Carlo codes for generation of input data for these dose calculation algorithms, as would be required by the method of McNutt *et al.* [99]. A disadvantage of our approach could be the

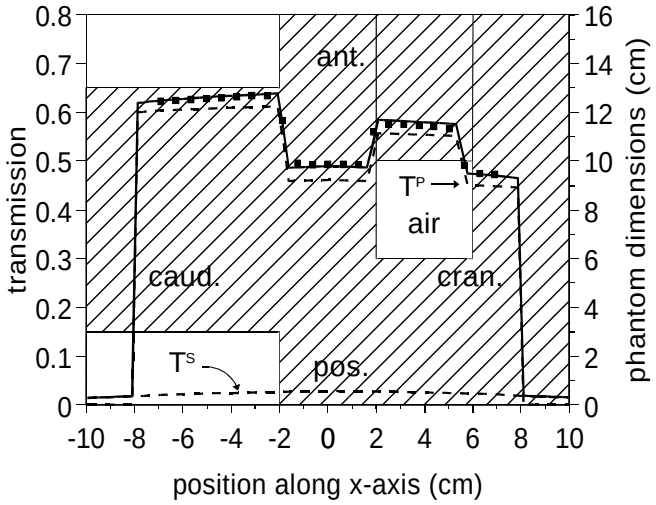

Figure 4.8. The depicted polystyrene head and neck phantom with a constant cross section in lateral direction was irradiated with a 16×10 cm^2 field of the 6 MV beam. The predicted (solid line) and measured (markers) transmission are shown. The upper and lower dashed line represent the primary and scatter component of the calculated transmission.

required effort for the measurement of the beam data. As mentioned in section 4.3.3, the set of w, t, L-combinations for which transmission measurements were performed for the 6 MV beam contains some clinically irrelevant combinations. Furthermore, the fields 3×3 and 4×4 cm^2, used to derive the primary component, only have to be measured for one L (see section 4.3.3.1). Skipping these w, t, L-combinations and the one's for which the isocenter is outside or at the edge the phantom the set reduces from 240 w, t, L-combinations, as listed in section 4.3.3, to 140. For dosimetric verification of the open (non-wedged) fields used for treatment of prostate cancer patients with the 25 MV beam of the MM50 racetrack microtron, the relevant beam data set could be measured in only 4 hours.

The substitution of patients by equivalent homogeneous phantoms makes this algorithm easy to implement and fast. Using a Hewlett Packard 712-80 workstation (32 MB, HP-UX 10.20, 92.0 million instructions per second (MIPS)) calculation of the EHP for one field takes 4 minutes, of $T(x, y)$ 25 seconds and of $D_{p,0}(x, y)$ 20 seconds. These calculations are performed off-line in batch mode and only have to be done once for each patient. The accuracy of calculated transmissions is very high ($\sim$1%, see section 4.4). No systematic deviations between measured and predicted transmissions have been found.

Following equation (4.1), $D_{p,0}(x, y)$, i.e. the PDI that would have been measured in the absence of the patient, can be derived from

$$D_{p,0}(x, y) = D_p(x, y)/T(x, y)$$

with $D_p(x, y)$, the measured PDI with the patient in the treatment beam and $T(x, y)$ the predicted transmission. $D_{p,0}(x, y)$, which is proportional to the beam fluence entering the patient, could then be used for a check on the beam flatness and symmetry or for a forward calculation of the actually delivered dose distribution in the patient. A potential problem with

the above described scenario for derivation of $D_{p,0}(x, y)$ is that the calculated transmission $T(x, y)$, used in this scenario for the derivation of $D_{p,0}(x, y)$ does, in turn, also depend on the incoming beam fluence ($f(r)$ in equation (4.4)) and therefore on $D_{p,0}$(x,y). To study the dependence of transmissions $T(x, y)$ on the beam fluence profile $f(r)$, we have compared transmission predictions with the nominal beam fluence profile in equation (4.4) with predictions performed with two alternative profiles substituted in equation (4.4). By definition, both alternative profiles were normalized to 1 at the beam axis. The first was a highly non-flat, linear profile with a value of 1.30 at r=18 cm. The other, consisting of two straight lines defined by, respectively, $f(x, -18)$=0.7 and $f(x, 18)$=1.30 was highly asymmetric in the y-direction. The transmissions calculated with the nominal beam fluence and the two alternative profiles differ less then 1% for all points (x, y). Hence, also for strongly deviating fluence profiles $D_{p,0}(x, y)$ can be derived from a measured PDI using the transmission function $T(x, y)$ calculated with the expected nominal profile.

For several prostate cancer patients we have observed large local differences between PDIs measured with the SRI-100 during some of the treatment fractions and PDIs predicted with the methods described in this paper. The observed large differences point at variations in internal patient anatomy ('internal organ motion') due to variations in rectum filling; for some patients the anatomy during the registration of the planning CT-scan did not reflect the average anatomy during the daily treatments [84, 85]. Therefore, a forward calculation of the dose distribution delivered to the patient, based on a measured PDI and the planning CT-scan, can lead to erroneous conclusions. This problem could be overcome by using on-line measured CT-data generated with a tomotherapy unit [97].

The presented method for transmission prediction is only suitable for non-wedged photon beams. An extension for transmission prediction in wedged beams, based on only very few extra measured input data, is under investigation. The first results are promising [117]. PDI-prediction for intensity modulated beams generated either by dedicated tissue compensators or by dynamic multileaf collimation is a subject of future research.

Acknowledgments

The authors would like to thank P.R.M. Storchi, J.C.J. de Boer, J.B. van de Kamer and O.O. Graveland for their contributions. This work was financially supported by the Dutch Cancer Society (Grant DDHK 94-848).

Appendix: Derivation of scatter kernels $s(r, t, L)$

For each t, L-combination separately, the corresponding kernel $s(r, t, L)$ is calculated with the following algorithm.

Step 1 Definition of $s'(r, t, L)$
A new function is introduced

$$s'(r, t, L) = f(r) \cdot s(r, t, L). \tag{A1}$$

According to equation (4.5) $s'(r, t, L)$ should obey

$$S(w, t, L) = \int_{(x,y) \in w \times w} s'(r = \sqrt{x^2 + y^2}, t, L)\, dx\, dy \tag{A2}$$

for all fields $w \times w$.

Step 2 Calculation of a first approximation of $s'(r, t, L)$
First, on-axis scatter contributions $S(R, t, L)$ for circular fields are estimated from the measured scatter contributions for rectangular fields using $S(R, t, L) = S(w, t, L)$, with $R = w/\sqrt{\pi}$ the radius of the circular field. Assuming the validity of this procedure for calculation of $S(R, t, L)$, the following equation for $s'(r, t, L)$ can be derived from equation (A1)

$$S(R, t, L) = \int_{r=0}^{R} 2\,\pi\, r\, s'(r, t, L)\, dr \tag{A3}$$

and a first approximation for $s'(r, t, L)$ at points $r = n\delta$ (δ=0.25 cm) can be calculated by numerical differentiating $S(R, t, L)$:

$$s'(n \cdot \delta, t, L) = \frac{S(n \cdot \delta, t, L) - S((n-1) \cdot \delta, t, L)}{2\pi n \delta^2} \quad n = 1, \ldots, N, \tag{A4}$$

N is the index of the largest circular field involved.

The applied conversion of measured scatter contributions for square fields into scatter contributions $S(R, t, L)$ for circular fields introduces (small) errors in the function $s'(r, t, L)$. Therefore, the following iterative algorithm is applied to calculate $s'(r, t, L)$ from its first approximation.

Step 3 Calculation of $s'(r, t, L)$ in an iterative procedure
First, scatter contributions $S(w_j, t, L)$ for all square fields $w_j = 0.5 \cdot j$ are determined by interpolation in the measured $S(w, t, L)$-data. Then, starting with the largest field, these scatter contributions are also calculated using

$$T^S(w_j, t, L) = \int_{(x,y) \in w_j \times w_j} s'(r = \sqrt{x^2 + y^2}, t, L)\, dx\, dy. \tag{A5}$$

and the difference between $S(w_j, t, L)$ and $T^S(w_j, t, L)$ is spread over all elements of $s'(r, t, L)$ that contribute to the calculated scatter:

$$n_j = \frac{\sqrt{\frac{1}{2}w_j^2}}{\delta}$$
$$\Delta = \frac{S(w_j, t, L) - T^S(w_j, t, L)}{n_j} \tag{A6}$$
$$s'(n \cdot \delta, t, L) \sim s'(n \cdot \delta, t, L) + \frac{\Delta}{2\pi n \delta^2} \quad n = 1, \ldots, n_j$$

with n_j the number of elements contributing to the on-axis scatter in a $w_j \times w_j$-field and where $\sim$ means an update of the value for $s'(n \cdot \delta, t, L)$. The procedure of calculating the scatter contribution with equation (A5) and correcting $s'(r, t, L)$ with (A6) is subsequently repeated for the next field $(j - 1)$ and so forth up to the smallest field $(j = 1)$. This whole iterative procedure for correcting $s'(r, t, L)$ is repeated five times after which $s'(r, t, L)$ has converged to a stable solution. The differences between the measured and calculated transmissions are then smaller than 0.2%.

Step 4 Calculation of the scatter kernel $s(r, t, L)$

The scatter kernel $s(r, t, L)$ can be calculated from the derived $s'(r, t, L)$ using equation (A1). However, the maximum radius r for which $s'(r, t, L)$ can be obtained with the above described procedure is equal to the radius of the largest equivalent circular field. To be able to account for the scatter contribution from one corner to the opposite corner of a large field, the tail of the kernel is logarithmically extrapolated to $r = \sqrt{2 \times w_{\max}^2}$, with $w_{\max}$ the size of the largest square field.

Chapter 5

In vivo dosimetry for prostate cancer patients using an electronic portal imaging device; demonstration of internal organ motion

Marco Kroonwijk, Kasper L. Pasma, Sandra Quint, Peter C.M. Koper,
Andries G. Visser and Ben J.M. Heijmen
Radiother. Oncol. 49(2): 125-132, 1998.

Purpose: To investigate the use of a commercially available video-based EPID for in vivo dosimetry during treatment of prostate cancer patients.

Methods: For ten prostate cancer patients, the inter-fraction variation within measured portal dose images (PDIs) was assessed and measured PDIs were compared with corresponding predicted PDIs, based on the planning CT scan of the patient.

Results: For the lateral fields, the average standard deviation in the measured *on-axis* portal doses during the course of a treatment was 0.9%; for the anterior fields this standard deviation was 2.2%. The difference between the average on-axis measured portal dose and the predicted portal dose was $0.3 \pm 2.1\%$ (1 SD) for the lateral fields and $0.7 \pm 3.4\%$ (1 SD) for the anterior fields. *Off-axis* differences between measured and predicted portal doses were regularly much larger (up to 15%) and were caused by frequently occurring gas pockets inside the rectum of the patients during treatment or during acquisition of the planning CT scan. The detected gas pockets did sometimes extend into the gross tumour volume (GTV) area as outlined in the planning CT scans, implying a shift of the anterior rectum wall and prostate in anterior direction (internal organ motion).

Conclusions: The developed procedures for measurement and prediction of PDIs allow accurate dosimetric quality control of the treatment of prostate cancer patients. Comparing measured PDIs with predicted PDIs can reveal internal organ motion.

5.1 Introduction

EPIDs have become a useful tool for the verification and correction of daily patient set-up during radiotherapy treatment [8, 28]. For this purpose, the position of bony structures in a portal image, relative to the treatment field, is compared with their position in a corresponding simulator image or digitally reconstructed radiograph (DRR).

Portal images also contain dosimetric information; the pixel signals (grey scale values) in portal images are related to the portion of radiation transmitted through the patient and hence also related to the dose absorbed by the patient. Several years ago investigations started to find out whether the video-based SRI-100 EPID (Philips Medical Systems, Crawley, UK) can be used for dosimetric treatment verification. The linearity and stability of this system make it very suitable for dosimetric applications [39, 61, 81]. Since 1994, two of these EPIDs are in daily use for dosimetric quality control of the scanning photon beams of our MM50 Racetrack microtron (Scanditronix Medical, Uppsala, Sweden) [39]. Recently, an algorithm has been developed to convert a measured EPID image into an absolute portal dose image (PDI), defined as the (transmitted) dose distribution in the plane of the fluorescent screen of the EPID, located at 160 cm from the focus [61, 116, 125]. Also, a method has been developed for prediction of PDIs, based on the planning CT scan of the patient [64, 115]. Comparing PDIs obtained with the EPID during treatment with predicted PDIs can reveal problems like incorrect (dosimetric) performance of the treatment unit, erroneous design, production or application of compensators and deviations of the patient anatomy during the daily treatment fractions from the anatomy during acquisition of the planning CT scan [172].

This paper reports on our first clinical experience with in-vivo dosimetry using an EPID. For the ten prostate cancer patients in this study, EPID images were acquired for all treatment fields on every treatment day. The inter-fraction (i.e. day-to-day) variation in measured PDIs was assessed and measured PDIs were compared with a corresponding predicted PDI which was calculated using the planning CT scan of the patient. The obtained data point at internal organ motion due to observed gas pockets in the rectum of the patients.

5.2 Material and Methods

5.2.1 Patients

Six out of ten prostate cancer patients in this study participated in a randomized trial, comparing conventional treatment using rectangular fields with conformal treatment using multi-leaf collimator (MLC) defined fields [83]. One of the patients was treated after a prostatectomy. For all ten patients a planning CT scan was acquired with a slice distance of 5 mm. The patients were asked to retain full bladder at the time of acquisition of the planning CT scan and during the daily treatments. No attempts were made to control the rectal contents of the patients. For each patient the visible prostate and the seminal vesicles were outlined manually on all applicable CT slices by the radiation oncologist. The obtained gross tumour volume (GTV) [73] was then extended automatically in 3-dimensions (3D) [145, 147] with a margin of 15 mm, yielding the planning target volume (PTV) [73]. The treatment plans were designed with the CadPlan 3D treatment planning system (TPS) (Varian-Dosetek, Espoo, Finland). All patients were treated in supine position with a three field, isocentric technique, consisting of one anterior and two lateral oblique fields that were partially delivered with a 60^{o} wedge inserted.

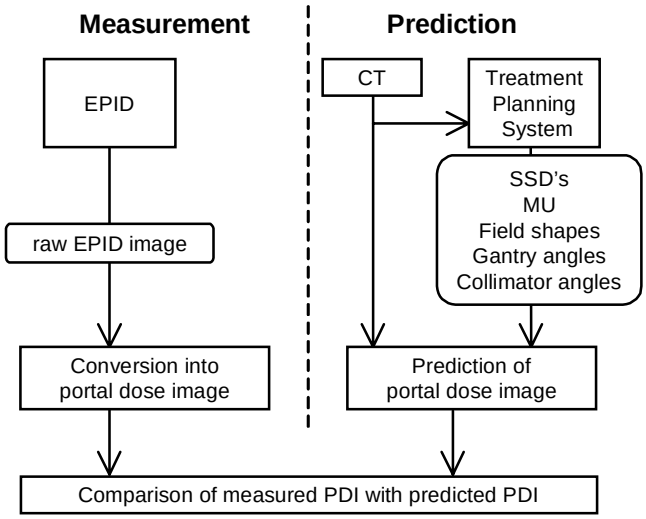

Figure 5.1. Schematic overview of the implemented dosimetric treatment verification method (in vivo dosimetry) for comparison of measured and predicted PDIs.

The treatments were performed with the 25 MV photon beam of a MM50 racetrack microtron. The doserate was 300 monitor units (MU) min^{-1}. A total dose of 66 Gray was prescribed to the isocenter and delivered in 33 fractions. Apart from some minor underdosages (<2%) in small parts of the superior and inferior ends of the PTV of some patients, the treatment plans fulfilled the ICRU-50 recommendations on dose homogeneity in the PTV [73]. (At present, these underdosages are avoided by using intensity modulated beams) [37].

During treatment, patient set-up was verified and corrected using an off-line correction protocol, based on analysis of the position of bony structures in EPID images, acquired in the non-wedged portion of each treatment field [8]. Using this protocol the standard deviation of systematic and average random 3D set-up errors are as low as 1.5 and 2.0 mm, respectively. Prior to the analyses of measured PDIs, the position of the bony structures in all daily measured images was registered with the bony anatomy visible in a corresponding DRR that was derived from the planning CT scan of the patient.

5.2.2 In vivo dosimetry

For the patients in this study, EPID images were acquired for all treatment fields on every treatment day and the inter-fraction variation in measured PDIs was assessed. Moreover, measured PDIs were compared with a corresponding predicted PDI calculated using the planning CT scan of the patient; this procedure is schematically shown in figure 5.1. Details on the prediction and measurement of PDIs are discussed in sections 5.2.2.1 and 5.2.2.2.

5.2.2.1 PDI prediction

The fixed focus-to-fluorescent screen distance of the applied EPID is 160 cm. Due to the resulting large air gap between the patient and the EPID detector (35-55 cm) the CadPlan TPS

cannot be used for accurate prediction of PDIs for this EPID. Therefore, we have developed our own algorithms to predict PDIs, using planning CT data of the patient as input [64, 85, 115]. Primary photon contributions and contributions from photons scattered from the patient onto the EPID are calculated separately and are added to obtain the PDI.

For calculation of the primary component, beam-hardening effects, e.g. due to a flattening filter, a wedge or a compensator, are taken into account. Scatter contribution calculations are basically convolutions of the two-dimensional beam fluence profile entering the patient with scatter kernels, describing the scatter from the patient onto the EPID. Basic input data for the calculations are obtained from a set of transmission measurements through flat, polystyrene absorbers for relevant absorber thicknesses, field sizes and distances to the EPID detector [115]. For a wide range of inhomogeneous anthropomorphic phantoms and treatment energies, predicted portal dose values and doses measured with an ionisation-chamber agree within 1% (1 SD) [64, 85, 115].

5.2.2.2 PDI measurement

Portal images were acquired with a commercially available video-based SRI-100 EPID. This EPID basically consists of a fluorescent screen, two mirrors and a charge coupled device (CCD) camera [2, 164]. In order to reduce detection of high energy electrons generated inside the patient, an extra one millimeter thick stainless steel plate was mounted on top of the standard fluorescent screen, which consists of a 1.65 mm thick stainless steel plate coated with a fluorescent layer. The total water equivalent depth of the EPID detector is only slightly smaller than the depth of maximum dose of the applied 25 MV photon beam [116]. The extra build-up layer resulted in a minor decrease in resolution but at the same time led to an increase of the signal-to-noise ratio in portal images. Modifications to the software of the SRI-100 system were performed at the level of the macro command language that comes with the system: (i) the standard image acquisition time was adjusted to fully enclose the irradiation time in order to measure the total delivered dose for each treatment field ($\leq$58 MU: 12.8 s, 59-69 MU: 15.36 s, 70-86 MU: 19.2 s, 87-115 MU: 25.6 s, 116-173 MU: 38.4 s and 174-384 MU: 76.8 s) and (ii) for dosimetric purposes, an additional "raw" 16-bit image was saved to avoid digitization noise in low grey scale value images [85, 116, 125]. Image enhancement procedures, used to obtain adequate image quality for patient set-up verification, continued automatically after the raw image was saved. With these modifications, acquisition of portal images, suitable for in vivo dosimetry, could be fully integrated into existing imaging routines for patient set-up verification without introducing an increase in the overall treatment time.

Visible photons produced by the x-ray beam in a point of the fluorescent screen not only generate a signal in the corresponding pixel of the EPID image, but also generate a (much lower) signal in all other pixels. Heijmen *et al.* have shown that this is due to light scatter from components within the EPID structure onto the CCD chip [61]. PDIs are derived from measured EPID images by removing the contributions from scattered light to the pixel signals in an EPID image using a deconvolution algorithm, as described by Pasma *et al.* [116, 125]. Using this method, derived PDIs generally agree within 1% (1 SD) with ionisation-chamber measurements in open, wedged and intensity modulated beams for various anatomical phantoms.

5.2.3 EPID stability

During the study, the stability of the EPID response was verified on a two-weekly basis by comparing the pixel signals in acquired EPID images with measurements performed with an ionisation chamber array, positioned at 100 cm from the focus. Details on the applied set-up and equipment are given in [39]. During the four month period of this study, the variation in *absolute* on-axis EPID response was 0.7% (1 SD). The variation in the EPID response, *relative* to the on-axis measured grey scale value was less than 0.2% (1 SD). Both the observed variations in absolute on-axis response and in the relative off-axis response are in agreement with the observations of Heijmen *et al.* [61] and Dirkx *et al.* [39]. In the analyses of the inter-fraction variation in the portal doses measured during patient treatment, the reported standard deviations were obtained by subtracting 0.7^2 from the square of each measured standard deviation; this corrected standard deviation is more directly correlated with patient thickness variations.

5.3 Results and discussion

For each patient, acquisition of EPID images was planned for all of the 33 treatment fractions. However, some portal image acquisitions failed, e.g. because of accelerator interlocks or starting image acquisition too late, leaving about 30 successful acquisitions per treatment field, per patient.

5.3.1 On-axis portal doses

For each patient and for the lateral and anterior fields separately, the on-axis inter-fraction variation in measured PDIs and the average on-axis differences found between the measured PDIs and the predicted PDI are presented in table 5.1. For the lateral fields, the average standard deviation in the on-axis measured portal doses was 0.9%. For the anterior fields the standard deviation was 2.2%. For the ten patients, the average difference between the on-axis measured portal dose and the predicted portal dose was $0.3 \pm 2.1\%$ (1 SD) for the lateral fields and $0.7 \pm 3.4\%$ (1 SD) for the anterior fields.

From the measured set of transmissions through flat water-equivalent absorbers, as used for the PDI prediction algorithm, relationships between radiological thicknesses and portal doses were derived for typical lateral and anterior treatment fields. A variation in radiological thickness of 1 cm, e.g. due to a variation in rectum and/or bladder filling, results in a variation in the transmitted dose of approximately 1.9% for a lateral field and 3.1% for an anterior field. This difference between lateral and anterior fields is an explanation for the observed larger standard deviations for the anterior fields. Variations in on-axis portal dose could also be slightly higher for the anterior fields because for these fields the central ray-line passes both the rectum and the bladder, whereas the central ray-line of the lateral fields does not pass organs with a variable filling.

5.3.2 Off-axis portal doses

For the six patients with the largest inter-fraction variation in measured PDIs, the observed variations for the right lateral field are presented in figure 5.2, together with beam's-eye-view

Table 5.1. On-axis inter-fraction variation in measured PDIs and average on-axis difference between measured and predicted PDIs for lateral and anterior fields separately, for ten prostate cancer patients.

	Lateral field		Anterior field	
patient number	Difference between measured and predicted PDI [%]	Inter-fraction variation (1 SD) [%]	Difference between measured and predicted PDI [%]	Inter-fraction variation (1 SD) [%]
1	-0.1	1.2	-4.2	3.5
2	2.7	0.5	2.0	1.6
3	1.2	0.3	-0.3	0.2
4	0.5	1.1	1.5	1.7
5	1.9	0.6	3.6	2.6
6	-4.6	1.0	3.7	1.3
7	2.2	1.1	4.2	4.2
8	1.6	0.2	-5.6	2.8
9	-0.8	1.5	1.3	2.2
10	-1.3	1.1	0.8	0.7

(BEV) contours of the GTV (prostate + seminal vesicles), the rectum and the bladder, as derived from the planning CT scan. For patient 8, the inter-fraction variation is also presented in colour in figure 5.3a. For the lateral fields, areas with large variations (SD $>$ 3%) are mainly found for pixels corresponding to rays passing through the planned position of the rectum, the superior/posterior portion of the prostate, and the posterior part of the seminal vesicles. For rays passing only through the bladder, the observed variations in measured portal doses are generally much smaller. For the anterior fields, the areas with large variations are also strongly correlating with the BEV contour of the rectum, as depicted in figure 5.3b for patient 8.

For those treatment fractions that show large differences between measured and predicted PDIs, the deviations do mostly occur in the areas of the PDI for which also large inter-fraction variations are observed. For patient 8, differences between the PDI measured during fraction 13 and the corresponding predicted PDI are presented in figures 5.3c and 5.3d for the right lateral field and the anterior field, respectively. The maximum difference between measured and predicted portal dose is 15%, pointing at a difference in lateral radiological pathlength

Figure 5.2. Observed inter-fraction variations in measured PDIs for the right lateral treatment field of patients 1 and 5-9. Each pixel represents the standard deviation in the observed portal doses during the course of the treatment. The dashed BEV contours represent, from left to right, the rectum, the GTV including prostate and seminal vesicles (not available for patient 1 because of prostatectomy) and the bladder. The presented iso-standard deviation contours connect pixels with standard deviations of 2 and 3% for patients 1, 5 and 6. For patients 7, 8 and 9 only the 3% contour is displayed, because maximum standard deviations in these images are larger than 4%.

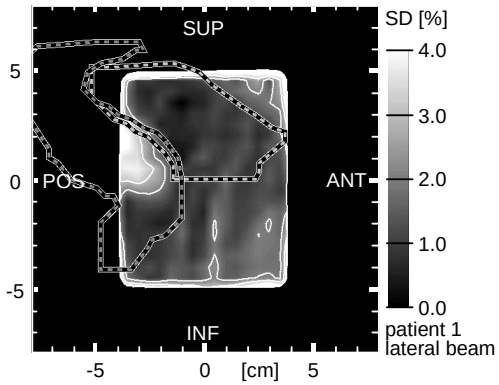
SUP
POS
ANT
INF
5
0
-5
-5
0
[cm]
5
SD [%]
4.0
3.0
2.0
1.0
0.0
patient 1
lateral beam

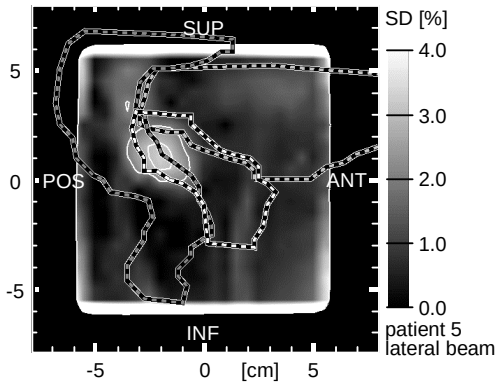
SUP
POS
ANT
INF
5
0
-5
-5
0
[cm]
5
SD [%]
4.0
3.0
2.0
1.0
0.0
patient 5
lateral beam

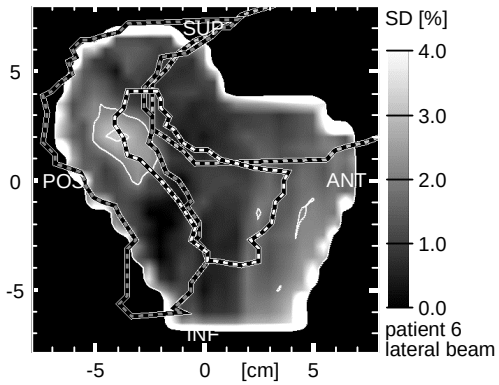
SUP
POS
ANT
INF
5
0
-5
-5
0
[cm]
5
SD [%]
4.0
3.0
2.0
1.0
0.0
patient 6
lateral beam

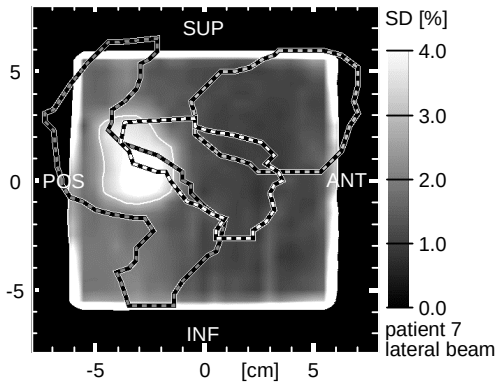
SUP
POS
ANT
INF
5
0
-5
-5
0
[cm]
5
SD [%]
4.0
3.0
2.0
1.0
0.0
patient 7
lateral beam

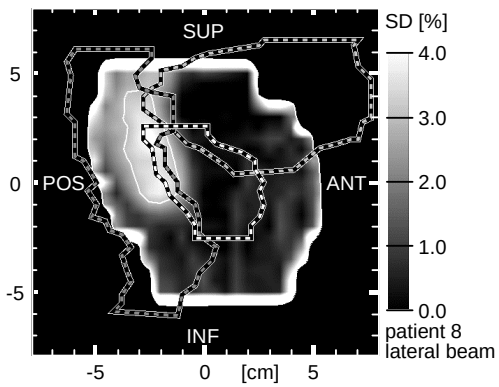
SUP
POS
ANT
INF
5
0
-5
-5
0
[cm]
5
SD [%]
4.0
3.0
2.0
1.0
0.0
patient 8
lateral beam

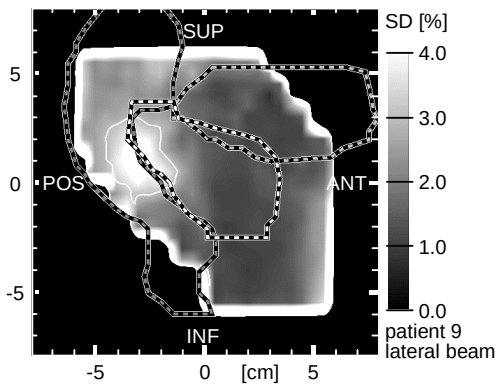
SUP
POS
ANT
INF
5
0
-5
-5
0
[cm]
5
SD [%]
4.0
3.0
2.0
1.0
0.0
patient 9
lateral beam

with the planning CT scan of about 6 cm. Also for patient 8, figures 5.3e and 5.3f show the difference between the average measured PDI (average of 27 fractions) and the predicted PDI for the right lateral field and the anterior field, respectively.

5.3.3 Gas pockets and organ motion

Observed variations in both lateral and anterior measured PDIs were often due to localized areas of increased portal dose inside the rectum contour and the posterior part of the GTV contour, pointing at the presence of gas pockets inside the rectum of the patients of variable size and shape. In the presence of both faeces and a gas pocket, the gas is generally floating on top of the faeces. In figures 5.3c and 5.3d, the red spots inside the GTV contour are due to the presence of a large gas pocket inside the rectum of patient 8 during treatment. During acquisition of the planning CT scan, the rectum of patient 8 also contained a (smaller) gas pocket, see figure 5.4. Due to this gas pocket, the differences between measured and predicted portal doses inside the BEV contour of the rectum in the lateral view (figure 5.3c) and on-axis differences in the anterior view (figure 5.3d) are relatively small.

The presence of a large gas pocket within the BEV contour of the GTV, as observed in the lateral field (figure 5.3c), points at internal organ motion. During fraction 13, the positions of the prostate and seminal vesicles were in disagreement with the planning CT scan. The gas pocket in the rectum of the patient pushed both the anterior part of the rectal wall and the GTV in anterior direction, yielding a risk for an unintended irradiation of a large part of the rectum and for underdosing the anterior part of the GTV. Similar observations were made for other fractions of patient 8 and also for other patients.

Figures 5.3e and 5.3f show, for patient 8, for each pixel the difference between the average measured portal dose (average of 27 fractions) and the predicted portal dose for the right lateral field and the anterior field, respectively. The blue spots are due to the presence of the gas pocket during acquisition of the planning CT scan (figure 5.4). The deviations inside the upper part of the GTV contour as presented in figure 5.3e, point at the presence of gas pockets during treatment that resulted in movement of the GTV in anterior direction.

Figure 5.3. The blue, red and yellow contours represent the BEV contours of, respectively, the rectum, the gross tumour volume and the bladder; point (0,0) corresponds to the isocenter.
a. Observed inter-fraction variations (1 SD) in the measured portal doses for the right lateral field of patient 8.
b. As figure 5.3a but now for the anterior field.
c. Differences between the portal doses measured during fraction 13 of patient 8 for the right lateral field and the corresponding predicted portal doses.
d. As figure 5.3c, but now for the anterior field.
e. Differences between the average measured PDI (average of 27 fractions) and the predicted PDI for the right lateral field of patient 8.
f. As figure 5.3e, but now for the anterior field.
The applied scale in figure 5.3c is different from the scale in figures 5.3d, 5.3e and 5.3f, due to the large deviations in portal dose as measured in fraction 13 in the lateral beam of patient 8.

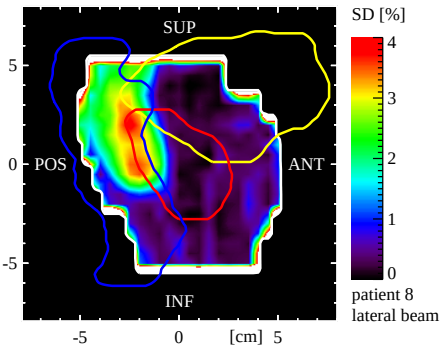
SUP
POS
ANT
INF
5
0
-5
-5
0
[cm]
5
SD [%]
4
3
2
1
0
patient 8
lateral beam

(a)

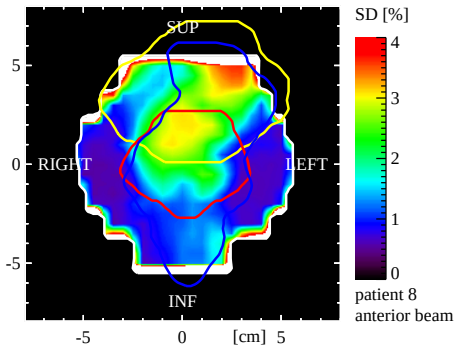
SUP
RIGHT
LEFT
INF
5
0
-5
-5
0
[cm]
5
SD [%]
4
3
2
1
0
patient 8
anterior beam

(b)

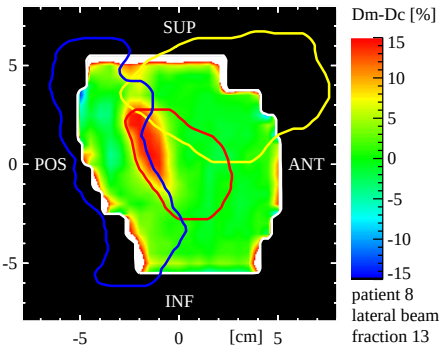
SUP
POS
ANT
INF
5
0
-5
-5
0
[cm]
5
Dm-Dc [%]
15
10
5
0
-5
-10
-15
patient 8
lateral beam
fraction 13

(c)

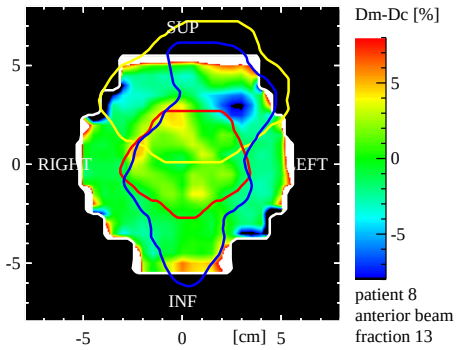
SUP
RIGHT
LEFT
INF
5
0
-5
-5
0
[cm]
5
Dm-Dc [%]
5
0
-5
patient 8
anterior beam
fraction 13

(d)

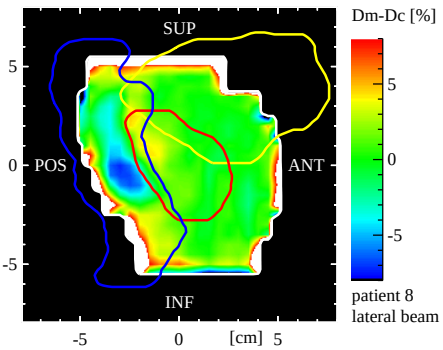
SUP
POS
ANT
INF
5
0
-5
-5
0
[cm]
5
Dm-Dc [%]
5
0
-5
patient 8
lateral beam

(e)

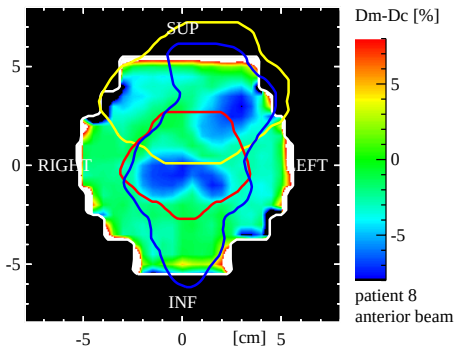
SUP
RIGHT
LEFT
INF
5
0
-5
-5
0
[cm]
5
Dm-Dc [%]
5
0
-5
patient 8
anterior beam

(f)

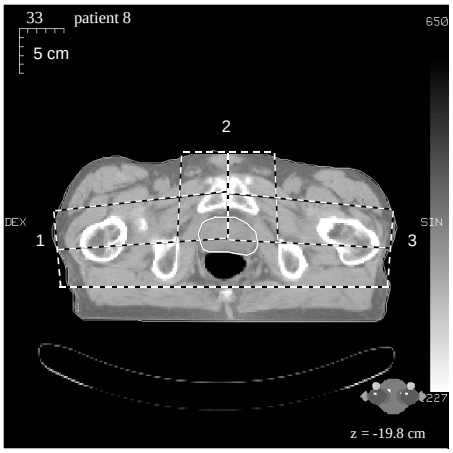

Figure 5.4. The planning CT scan of patient 8, used for PDI prediction. The transversal slice shown contains the isocenter. The closed white contour indicates the GTV volume and the dashed lines show the applied beams. Notice the gas pocket inside the rectum.

In recent years, several groups have studied internal organ motion in prostate cancer patients [4, 6, 7, 31, 87, 102, 132, 152, 159, 163]. The observed prevalence in this study of gas pockets occurring in the upper part of the rectum close to the superior portion of the prostate and the seminal vesicles (figures 5.2 and 5.3) is in agreement with the presence of internal organ motion in these areas reported in the literature, see e.g. Beard *et al.* [7] and van Herk *et al.* [159]

For back-projection methods aiming at calculation of the 3D patient dose distribution from measured portal images (see e.g. Hansen *et al.* [60] and McNutt *et al.* [98]), an accurate 3D representation of the patient is required. In this study, we have observed that large deviations between measured and predicted portal doses were always due to differences in patient anatomy during acquisition of the planning CT scan and during the treatment fractions, due to gas pockets in the rectum of the patients. In case of large deviations between predicted and measured PDIs, calculation of the patient dose distribution based on the planning CT scan would therefore have resulted in non-meaningful dose distributions in the corresponding volumes in the patients. In on-going studies we are investigating the applicability of gas pockets visible in EPID images for on-line *geometrical* verification and correction of the position of the prostate of the patient in the treatment beams. The data presented in this paper do not allow to decide whether EPID images can be used for detection of internal organ motion due to variation in the amount of faeces present in the rectum.

5.4 Conclusions

The small average on-axis differences between measured and predicted PDIs and the variation therein indicate that the developed methods and procedures allow accurate dosimetric quality control of the treatment of prostate cancer patients in clinical practice. Large off-axis differences

between measured and predicted PDIs have been found to correspond with frequently occurring gas pockets inside the rectum of the patient during treatment or during acquisition of the planning CT scan. In case a detected gas pocket extends into the GTV area, as outlined in the planning CT scan, organ motion is evident.

Acknowledgements

The authors would like to thank Joep Stroom, Maarten Dirkx and Hans de Boer for fruitful discussions and are grateful to the technologists working at the MM50 racetrack microtron for the daily acquisition of the images during patient treatment and for the effort that has been made to implement the procedures in clinical practice. This work was financially supported by grant DDHK 94-848, awarded by the Dutch Cancer Society.

Chapter 6

Transit dosimetry with an electronic portal imaging device for 115 prostate cancer patients

Kasper L. Pasma, M.Sc., Marco Kroonwijk, B.Sc., Sandra Quint, Andries G. Visser, Ph.D, and Ben J.M. Heijmen, Ph.D
Submitted to *Int. J. Radiation Oncol. Biol. Phys.*

Purpose Comparison of predicted portal dose images (PDIs) with PDIs measured with an electronic portal imaging device (EPID) may be used to detect errors in the dose delivery to patients. However, these comparisons can not reveal errors in the MU calculation of a beam, since the calculated number of MU is both used for treatment (and thus affects the PDI measurement) and for PDI prediction. In this paper a method is presented that enables 'in vivo' verification of the MU calculation of the treatment beams. The method is based on comparison of the intended on-axis patient dose at 5 cm depth for each treatment beam, D_5, with D_5 as derived from the portal dose D_p measured with an EPID. The developed method has been evaluated clinically for a group of 115 prostate cancer patients.

Methods and Materials The patient dose D_5 was derived from the portal dose measured with a fluoroscopic EPID using (i) the predicted beam transmission (i.e. the ratio of the portal dose with and without the patient in the beam) calculated with the planning CT data of the patient and (ii) an empirical relation between portal doses D_p and patient doses D_5. For each beam separately, the derived patient dose D_5 was compared with the intended dose as determined from the relative dose distribution as calculated by the treatment planning system and the prescribed isocenter dose (2 Gy). For interpretation of observed deviating patient doses D_5, the corresponding on-axis measured portal doses D_p were also compared with predicted portal doses.

Results For three beams, in total 7828 images were analyzed. The mean difference between the predicted patient dose and the patient dose derived from the average measured portal dose was: $0.4 \pm 3.4\%$ (1 SD) for the anterior-posterior (AP) beam and $-1.5 \pm 2.4\%$ (1 SD) for the lateral beams. For 7 patients the difference between the predicted portal dose and the average measured portal dose for the AP beam and the corresponding difference in patient dose were both greater than 5%. All these patients had relatively large gas pockets (3-3.5 cm in AP direction) in the rectum during acquisition of the planning CT, which were not present during (most) treatments.

Conclusions An accurate method for verification of the MU calculation of an x-ray beam using EPID measurements has been developed. The method allows the discrimination of errors that are due to changes in patient anatomy related to appearance or disappearance of gas pockets in the rectum and errors due to a deviating cGy/MU-value.

6.1 Introduction

So far, electronic portal imaging devices (EPIDs) have been mainly used for patient set-up verification. For this purpose the position of the bony anatomy in a portal image is compared with the position in a corresponding simulator image or digitally reconstructed radiograph (DRR). An EPID can also be used to measure portal dose images (PDIs), i.e. a dose distribution behind the patient in a plane perpendicular to the beam axis [116, 172]. Several methods to use EPIDs for dosimetric treatment verification have been proposed [14, 60, 84, 98, 115, 118, 172, 175]. Only a few, small studies have been performed to evaluate proposed procedures in clinical practice [14, 60, 84, 118].

Boellaard *et al.* derived midplane dose distributions (2D) from measured PDIs [14]. Their method did not require CT data; the radiological thickness of the patient is determined from the ratio of a PDI acquired with and without the patient in the beam. Besides requiring an extra EPID measurement for each field this method has the drawback that it assumes inhomogeneities to be symmetrically positioned with respect to the patient midplane. This approach did sometimes result in an erroneous dose distribution, e.g. for the anterior beam of a prostate cancer patient with a large gas pocket in the rectum. Hansen *et al.* derived the primary fluence from a measured PDI and back projected that fluence through the patient to yield the primary fluence distribution in the patient. This distribution was then convolved with dose deposition kernels to derive the 3D dose distribution in the patient [60]. Results were presented for a humanoid phantom and a pelvic patient. McNutt *et al.* developed an iterative convolution/superposition algorithm to reconstruct the dose distribution in a patient from a measured PDI and showed results for three phantoms [98]. The last two methods require that the patient representation during treatment is known. In the method of Ying *et al.*, a deviating patient anatomy at the time of treatment is accounted for with an iterative procedure that modifies the planning CT data [175].

In our institution, PDIs are measured with a fluoroscopic EPID [61, 84, 116]. Pasma *et al.* have developed a deconvolution method to derive these PDIs from measured EPID images [116]. For anthropomorphic phantoms, the PDIs measured with the EPID agree within 1% with absolute portal dose measurements performed with an ionization chamber. Kroonwijk *et al.* have used this EPID for the daily measurement of PDIs for 10 prostate cancer patients [84]. In the lateral beams they observed large day-to-day variations in the areas of the PDIs corresponding with the rectum, situated adjacent to the upper part of the prostatic gland and the vesiculae seminalis. These variations were due to frequently occurring gas pockets with variable dimensions. Measured PDIs for these patients were also compared with predicted PDIs. These predictions were based on the planning CT scan of the patients [115]. Again, for the lateral beams large deviations between predictions and measurements occurred in areas close to the posterior/superior border of the prostate and the posterior part of the vesiculae seminalis. These deviations were due to the presence of large gas pockets during acquisition of the planning CT scan or during treatment. Gas pockets in the measured images did sometimes extend into the beam's-eye-view projection of the gross tumor volume (GTV) as derived from the planning CT scan, implying a shift of the anterior rectum wall and the prostate in ventral direction (internal organ motion).

Comparison of predicted PDIs with measured PDIs can reveal problems like a deviating cGy/MU-value, a deviating beam profile, erroneous data transfer from the treatment planning system (TPS) to the treatment unit, and deviations between the actual patient anatomy and the anatomy according to the planning CT scan. The calculated number of monitor units (MU)

for a beam is both used for treatment and for PDI prediction. Therefore, an error in the MU calculation of a treatment beam cannot be detected by comparison of measured and predicted PDIs.

In this paper we present a new and simple method to verify the calculated number of monitor units for a treatment beam. For each beam, the measured portal dose (D_p) is used to derive the corresponding on-axis patient dose at 5 cm depth (D_5), which is then compared with the predicted dose as determined with the relative dose distribution calculated by the TPS and the prescribed isocenter dose (2 Gy). The method has been clinically evaluated for 115 prostate cancer patients. For interpretation of observed differences, the on-axis measured portal doses were also compared with the portal dose calculated with the algorithm described in [115].

6.2 Methods and Materials

6.2.1 Patients

The 115 prostate cancer patients in this study were treated in the period February 1996 until March 1998 with the 25 MV photon beam of a Scanditronix MM50 racetrack microtron. 100 patients were treated in supine position and 15 in prone position. An isocentric technique was used for all patients, consisting of an anterior-posterior field (AP) and left lateral (LL) and right lateral (RL) oblique fields, which were partially delivered with a 60^o wedge inserted. Individually customized field shapes were created by a multileaf collimator. During each fraction a dose of 2 Gy was planned to be delivered to the isocenter. The treatment plans were designed with the Cadplan 3D treatment planning system (V2.7.9, Varian Dosetek, Espoo, Finland). The slice distance of the planning CT scans was 5 mm.

During treatment, the patient setup was verified and corrected using an off-line correction protocol, based on an analysis of the position of bony structures in EPID images, acquired in the non-wedged portion of each treatment field [8]. Using this protocol the systematic and random 3D setup errors were as low as 1.5 and 2.0 mm (1 SD), respectively. The time to setup the EPID software for image acquisition is about equal to the time required to rotate the gantry and to setup the next (non-wedged) field. The time to setup a wedged field (using a motorized wedge) after delivery of an open field for the same gantry angle is less than the setup time of the EPID. To prevent an increase in treatment time, EPID measurements in this study were therefore limited to the non-wedged fields. For the first 104 patients in the study the intention was to acquire images on a daily basis. For the last group of 11 patients, images were only acquired when required for the setup verification protocol (for these patients on average 9 images were acquired for each beam).

6.2.2 Portal dose measurements and predictions

Portal images were acquired with a commercially available fluoroscopic EPID (SRI-100, Philips Medical Systems, Crawley, UK). This EPID basically consists of a fluorescent screen, two mirrors and a CCD camera [2, 164]. The fluorescent screen is a 1.65 mm thick stainless steel plate coated with a layer of gadolinium oxysulphide. The focus to fluorescent screen distance of this EPID was fixed at 160 cm. To reduce the detection of high energy electrons generated in the patient, an additional 1 mm thick stainless steel slab was mounted on the standard fluorescent screen. Image quality is hardly affected by this additional layer; acquired images can be used

both for geometrical and for dosimetrical treatment verification [85]. Charge integration was performed both on the CCD chip and by adding multiple frames in the frame store memory. Each image was corrected for 'dark current' in the CCD chip, which was measured in 10 frames prior to the irradiation. These 8 bit deep 'dark current' frames were first multiplied by the ratio -120/10 and then added in a 16 bit frame store memory. Storing camera frames was then halted until the center pixel values of the camera frames reached a threshold, i.e. when the beam was switched on. Acquisition of the preset number of camera frames was then automatically started. Each frame was multiplied by the ratio of 120 and the preset number of frames and added in the frame store memory. Subsequently, the data in the frame store memory was divided by 120 and the 16 bit deep images were written to disk. The resulting pixel values are the mean of the pixel values in the acquired frames corrected for the dark current on the CCD chip. The accumulation time on the CCD chip was set to 560 ms. All irradiations were performed with a doserate of 300 MU min^{-1}. The machine was calibrated such that 1 MU delivers 1 cGy of dose at 100 cm from the focus at a depth of dose maximum in water for a 10×10 cm^2 field. To ensure that the whole treatment could be monitored, the acquisition time was automatically adjusted according to the preset number of MU by adapting the number of frames that were accumulated ($\leq$58 MU: 12.8 s, 59-69 MU: 15.36 s, 70-86 MU: 19.2 s, 87-115 MU: 25.6 s, 116-173 MU: 38.4 s and 174-384 MU: 76.8 s).

To be able to verify whether frame accumulation did fully enclose the beam-on time, two extra frames were acquired, one immediately after the acquisition of the frames used to determine the dark current and one just after acquisition of the preset number of frames used to acquire an image for geometrical and dosimetrical treatment verification. For both extra frames, the mean pixel value around the central axis was stored in a log file. In case one of these pixel values exceeded a threshold value it was concluded that image acquisition had started too late or too early and the image was not used in the analyses.

Conversion of measured EPID images into PDIs was performed in three steps. Acquired images were first corrected for the non-linear response of the system [116]. Subsequently, the image was corrected for the optical 'cross talk' by deconvolving it with a point spread function. This function describes the on-axis EPID response increase due to an off-axis irradiation of the fluorescent screen. The point spread function is derived from on-axis EPID response measurements (portal dose/pixel value) as function of field size [61, 116]. Finally, the resulting array is divided by a sensitivity array to correct for the spatially non-uniform EPID response. This array is slightly field size dependent, related to shortcomings of the on-axis measured point spread function in describing optical 'cross talk' in off-axis points [116]. The applied procedure allows accurate conversion of pixel values into portal doses for all field sizes. For anthropomorphic phantoms, derived PDIs generally agreed within 1% with the dose measured with an ionization chamber chamber [116]. The on-axis portal doses used for the derivation of patient doses at 5 cm depth were defined as mean portal doses in a region of 1.5×1.5 cm^2 (defined at 100 cm from the focus), centered around the beam axis.

During the study period, the EPID response gradually decreased due to radiation damage to the CCD chip ($\sim$3%/year). This decrease was carefully monitored and corrected for using the daily acquired images for the quality control of the absolute output and field flatness of the scanning photon beams of the MM50 [39] and the two-weekly output checks with an ionization chamber.

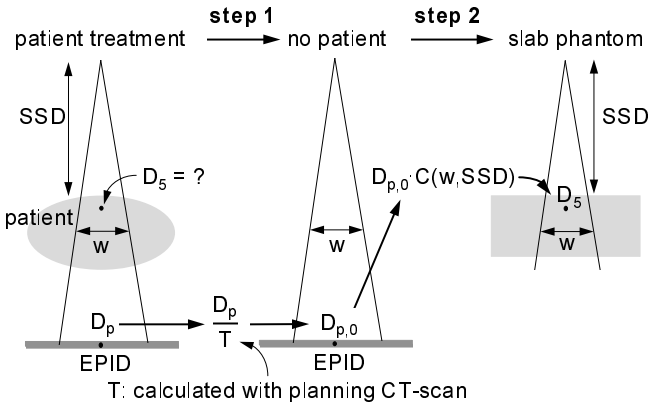

Figure 6.1. Overview of the method used to derive the patient dose D_5 from the measured portal dose D_p. The process is described in section 6.2.3.

PDI prediction was performed using the following equation

$$D_p(x, y) = T(x, y) \cdot D_{p,0}(x, y), \tag{6.1}$$

with $D_p(x, y)$ the portal dose in point (x, y) of the PDI, $T(x, y)$ a transmission function and $D_{p,0}$ the portal dose that would have occurred in (x, y) in absence of the patient. The calculation of $T(x, y)$ was based on the planning CT scan of the patient and the irradiation geometry as determined in the treatment planning process. Separate calculations were performed to assess the contributions from primary (non-scattered) photons and from photons that scattered from the patient onto the PDI-plane, which were then added. The applied algorithm is described in detail elsewhere [115]. For anthropomorphic phantoms irradiated with 6 MV, 23 MV and 25 MV photon beams, predicted and measured transmissions agreed within 1%. For the calculation of $D_{p,0}(x, y)$ (used in equation (6.1)) we used an algorithm developed for dose calculations in water phantoms and the calculated number of MU [115, 141, 142].

6.2.3 Derivation of the patient dose D_5 from the measured portal dose D_p

Derivation of the on-axis patient dose at a depth of 5 cm was performed in a two step process (see figure 6.1). First, the on-axis portal dose that would have been measured with the EPID without the patient in the beam ($D_{p,0}$) was derived using the inverse of equation (6.1). $D_{p,0}$ was then multiplied with a conversion factor yielding D_5, the on-axis patient dose at a depth of 5 cm:

$$D_5 = D_{p,0} \cdot C(w, \text{SSD}), \tag{6.2}$$

with w the equivalent square field size of the applied field and SSD the on-axis source-to-surface distance. $C(w, \text{SSD})$ was experimentally determined for a set of relevant SSDs and square fields (SSD=75, 80, 85, 90 and 95 cm and w=6, 8, 10, 12 and 14 cm) using a 25 cm thick water equivalent slab phantom and taking equation (6.2) as the definition of $C(w, \text{SSD})$. The on-axis portal dose without an absorber in the beam, $D_{p,0}$, and the dose D_5 in the slab

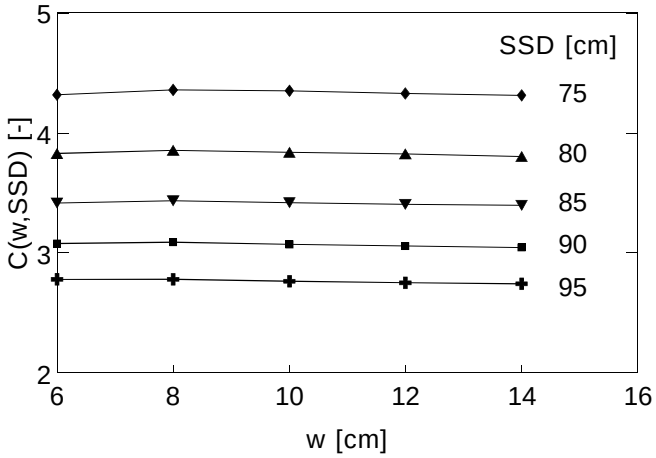

Figure 6.2. $C(w, \mathrm{SSD})$; the measured dose in a water equivalent slab phantom at 5 cm depth, divided by the corresponding portal dose measured in absence of the phantom.

phantom were both measured with an ionization chamber using 150 MU. $D_{p,0}$ was measured as a function of field size, D_5 also as a function of SSD. Data are presented in figure 6.2.

6.2.4 Derivation of the patient dose D_5 from the prescribed isocenter dose

The relative contribution of each individual beam to the combined dose distribution of all the beams (normalized to 100% in the isocenter) was calculated by the treatment planning system. For each beam separately, the relative on-axis dose at 5 cm depth was determined, which was converted to the absolute patient dose D_5 using the prescribed isocenter dose per fraction of 2 Gy. For the (retrospective) verification of the MU-calculation of each treatment beam of an individual patient, this predicted D_5 was compared with the D_5 derived from the average on-axis portal dose measured during the treatment sessions for which EPID-images were acquired.

6.3 Results

For the 115 patients in the study, in total 8038 images were acquired for the three treatment beams. Acquisition of the images did sometimes fail, due to a too early or too late start of image acquisition resulting in an incomplete accumulation of signal (the method to detect these errors is described in section 6.2.2), or due to an incomplete signal accumulation because of a treatment interrupt. The MM50 log file was used to identify these acquisition errors. In total 210 images had acquisition failures and were therefore excluded from the analyses.

For the two lateral beams and the AP beam distributions of the observed standard deviations in the measured on-axis portal doses for individual patients are depicted in figure 6.3. The mean standard deviation for the AP beam was 1.8% which is higher than the 1.2% for the lateral beams; this was also found in a previous study with 10 prostate cancer patients [84]. In the anterior-posterior direction variations in radiological thickness have relatively more effect

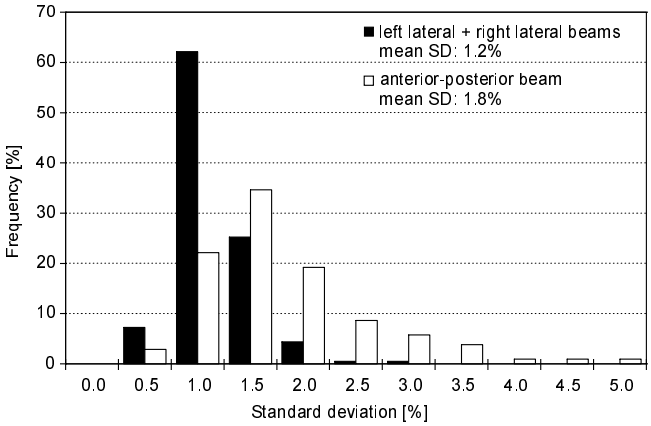

Figure 6.3. Distributions of observed standard deviations in the daily measured on-axis portal dose for the 115 patients in this study.

on the transmitted dose than in a lateral-direction. Furthermore, variations in radiological thicknesses for the AP fields are larger and more frequent since the central ray-line passes both the rectum and the bladder, whereas the central ray-line of the lateral fields does not pass through organs with a variable filling. Remarkable is the inter-patient variation of the observed standard deviations; which ranges from 0.5% upto 5%.

The distributions of per cent differences between the predicted and the average measured portal dose and the predicted and average measured D_5 for the LR beam, the RL beam and the AP beam are depicted in figure 6.4. As expected the standard deviations of the differences in D_5 are slightly higher than those in D_p, since the standard deviation of D_5 is a combination of the uncertainty in D_p and the uncertainty in the method to derive D_5 from D_p (this method is described in section 6.2.3). For the AP beam (figure 6.4c) there are 7 patients for which the difference between the predicted and average measured portal dose and the difference in patient dose D_5 are both greater than 5% (arbitrary value). A variation in radiological thickness of 1 cm results in a variation in transmitted dose of approximately 3% for the anterior field [84]. According to the planning CT-data, all these patients had a gas pocket in the rectum of 3-3.5 cm in AP direction. Apparently these gas pockets where absent during (most of) the treatments. For the LR and RL beams the observed differences in portal dose are maximally 5%.

Figure 6.5 shows the correlation of differences between predicted and measured portal doses and the corresponding differences between predicted and back projected patient doses. A deviation between the actual patient anatomy and the anatomy according to the planning CT scan equally affects both the difference between the predicted and measured portal dose and the difference between the predicted and back projected patient dose. This is also true in case of a deviating cGy/MU-value of the treatment beam. The latter deviation would result in a constant difference over the entire radiation field between the measured and predicted PDIs. The data points in the upper right corner of figure 6.5 belong to the 7 patients with a large gas pocket in the rectum during acquisition of the planning CT scan (see also figure 6.4c). In this study the differences between predicted and measured PDIs were always limited to an area around the beam axis; constant differences over the entire irradiation field did not occur, i.e.

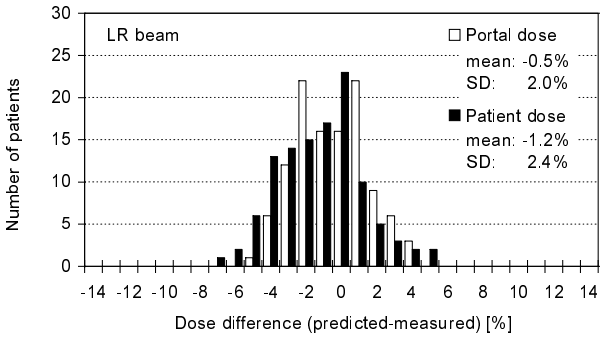

(a)

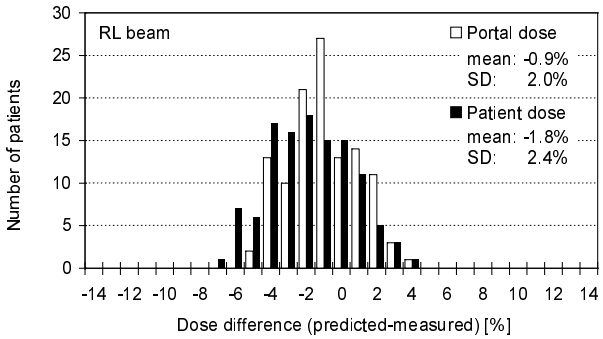

(b)

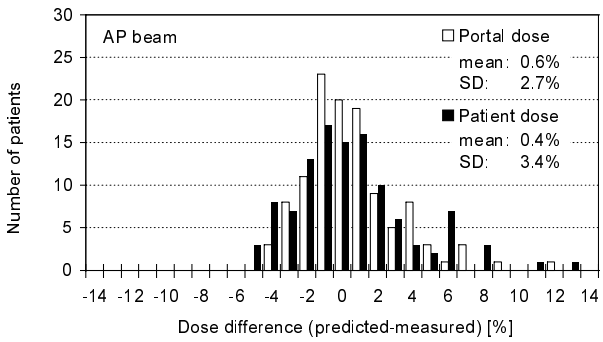

(c)

Figure 6.4. Histograms showing frequencies of observed per cent differences between the predicted and average measured portal doses D_p and between the predicted and average measured patient doses D_5 for (a) the left lateral beam, (b) the right lateral beam and (c) the anterior-posterior beam

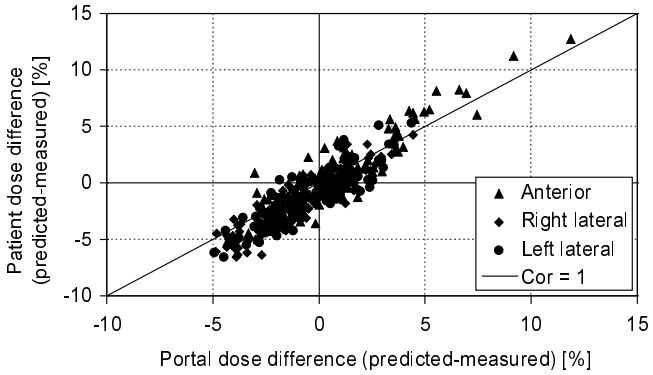

Figure 6.5. Correlation between the differences in predicted portal dose and the measured portal dose and the differences in predicted patient dose and the back projected patient dose. Each marker resembles one treatment beam for one patient. The solid straight line represents a perfect correlation.

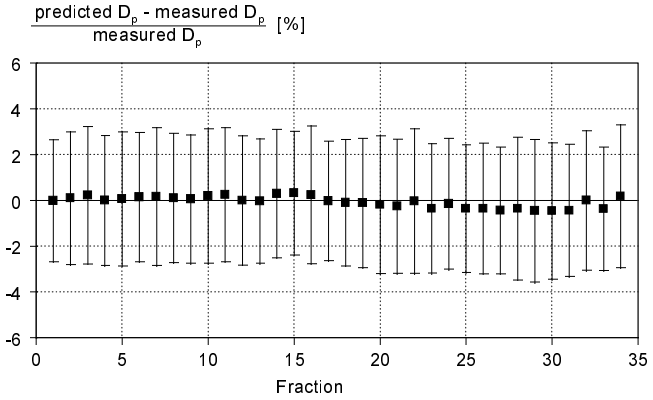

Figure 6.6. The per cent difference between the predicted portal dose and the measured portal dose, averaged over all patients and all beams, as a function of the fraction number. The error bars show the ± 1 SD variations.

deviating cGy/MU-values were not encountered.

In figure 6.5, an error in the calculated number of monitor units would result in a point far above (MU too high) or below (MU too low) the 1-to-1 line, since such an error *only* affects the difference in patient dose (parallel to the y-axis) and *not* the difference in portal dose (parallel to the x-axis), since both the measured and the predicted portal dose are based on the same (incorrect) number of MU. No errors of this type were found in this patient group.

In figure 6.6 the per cent difference between the predicted and measured portal dose as function of the fraction number has been plotted. The data shows that there is no time trend in the measured portal dose due to a systematic change in radiological thickness of the patients during the cause of treatment.

6.4 Discussion

So far most dosimetric verification studies have been performed using diodes for point measurements. However, diodes have several drawbacks: i. The increase in treatment time due to the time needed to position the diode on the patient. ii. Diodes act as a buildup material and thus increase the skin dose [109]. iii. If used for entrance dose measurements, diodes attenuate the primary beam [109]. iv. For practical reasons only very limited numbers of diodes are used for simultaneous measurements. v. In order to determine the midplane dose both entrance and exit dose measurements have to be performed. For a proper interpretation of these measurements a portal image for each treatment field is needed to determine the actual position of the detectors in the treatment field and their relative positions [70]. (The detector for the exit dose measurements is in the shadow of the detector for the entrance dose measurement if both detectors are placed on the beam axis.) Due to these drawbacks there are only a few studies with large numbers of patients, like that of Noel *et al.* with 7519 patients [110] and of Lathinen *et al.* who performed 1912 diode measurements at the first treatment and every time a treatment parameter was changed [86]. Both groups analyzed treatments for which discrepancies between the planned and measured dose occurred and found causes like: incorrect SSD, forgotten wedge filter, erroneously placed compensators, calculation errors and incorrect MU settings.

Using an EPID for dosimetric treatment verification has several advantages: there is no increase in treatment time (acquired images can be used both for setup verification and transit dosimetry), the portal dose can be acquired not in one or a few points, but for all points in the treatment field (also allowing a check of the validity of the planning CT-scan by comparison of predicted and measured PDIs [84]) and there is no physical contact of the detector with the patient. A potential problem of transit dosimetry with an EPID is that measured portal doses are rather insensitive to variations in the applied source-to-surface distances. However, this problem does not occur when transit dosimetry is combined with patient setup verification, as performed in this study [8].

For 7 out of the 115 patients the planning CT data was not representative for the treatment; bowel gas in the planning CT scan may have pushed the prostate in anterior direction [84] compared to its average position during treatments. However, we did not quantify this shift. Currently a study is performed based on multiple CT data [146]. For each patient, changes in anatomy as indicated by the planning CT scans will be correlated with changes in the calculated, i.e. simulated, PDIs that would have been measured with the EPID during treatment.

In principle the back projection method described in this paper can be expanded to derive the 3D dose distribution in the patient. Equation (6.1) can be used to derive the dose distribution that would have been measured in absence of the patient. This dose distribution is proportional to the beam fluence entering the patient [115]. The measured beam fluence can be used for a forward calculation of the dose distribution in the patient using the standard or an independent TPS. This dose distribution can then be compared with the planned dose distribution. A major difficulty is that the reconstructed dose distribution will be incorrect along the ray lines that pass through parts of the patient anatomy that have deviated compared to the situation during acquisition of the planning CT scan.

6.5 Conclusions

In this paper a method is presented that enables a verification of the MU calculation of treatment beams using EPID portal dose measurements. For each beam separately, the on-axis patient dose at a depth of 5 cm, D_5, is derived from the portal dose measured with an EPID and compared with the intended patient dose as determined from the relative dose distribution calculated by the TPS and the prescribed isocenter dose of 2 Gy. Comparison of an observed difference between measured and the predicted portal dose with the corresponding difference between the back projected and intended patient dose allows the discrimination of errors in the MU calculation and errors caused by a deviating patient anatomy due to appearance or disappearance of gas pockets in the rectum. All observed deviations larger than 5% (arbitrary value) could be attributed to variations in patient anatomies.

Acknowledgements

The authors would like to thank Martin Opdam for his help with the measurements, Joep Stroom for useful discussions and the technologists working at the MM50 racetrack microtron for their enthusiastic support of the project. This work was financially supported by the Dutch Cancer Society (grants DDHK 94-848 and DDHK 98-1681).

Chapter 7

Verification of compensator thicknesses using a fluoroscopic electronic portal imaging device

Kasper L. Pasma, Marco Kroonwijk, Erik B. van Dieren, Andries G. Visser
and Ben J.M. Heijmen
Med. Phys. in press

A method is presented for verification of compensator thicknesses using a fluoroscopic electronic portal imaging device (EPID). The method is based on the measured transmission through the compensator, defined by the ratio of the portal dose with the compensator in the beam and the portal dose without the compensator in the beam. The transmission is determined with the EPID by dividing two images, acquired with and without compensator inserted, which are only corrected for the non-linear response of the fluoroscopic system. The transmission has a primary and a scatter component. The primary component is derived from the measured transmission by subtracting the predicted scatter component. The primary component for each point is only related to the radiological thickness of the compensator along the ray line between the focus and that point. Compensator thicknesses are derived from the primary components taking into account off-axis variations in beam quality. The developed method has been tested for various compensators made of a granulate of stainless steel. The compensator thicknesses could be determined with an accuracy of 0.5 mm (1 SD), corresponding to a change in the transmitted dose of about 1% for a 10 MV beam. The method is fast, accurate and insensitive to long-term output and beam profile fluctuations of the linear accelerator.

7.1 Introduction

Compensators can be used in radiotherapy for beam intensity modulation. In our institute, a group of head and neck cancer patients is treated with a conformal technique based on intensity modulation to improve sparing of the salivary glands [157].

There have been several publications on how to perform quality assurance for compensators. Chu *et al.* used film for a 2D verification of the dose distribution at the exit plane of a phantom [25]. An advantage of using film is that the required equipment is commonly available in a radiotherapy department. Obvious disadvantages are the time needed for processing the films and the need of a sensitometric curve to convert optical densities into absorbed doses.

Mejaddem *et al.* compared the intended profile of the mold of a compensator with the profile measured with a laser interferometric transducer [100]. They found an average difference of 0.04 mm (1 SD) between the intended profile and the laser measurements. The high accuracy of this technique was needed since a deviation of 0.1 mm in thickness of the applied Cerrobend filling corresponded to 0.5% change in transmission dose for a 6 MV beam. The described technique is suited for commissioning of a milling device (especially for high-density compensators), but is impractical for routine checks of the produced molds.

Low *et al.* developed a method for verification of compensators by comparing the fluence measured with an electronic portal imaging device (EPID) with the fluence calculated using the intended filter shape [95]. They investigated the use of a liquid-filled matrix ionization chamber system (PortalVision, Varian). An advantage of using an EPID is that it can perform quick two-dimensional measurements. They limited their tests to relatively simple compensator geometries since they had no independent way to verify more complex geometries. The predicted and measured fluence for a 6 MV beam agreed within $\pm 3\%$, which was considered acceptable. For one test situation the measured fluence was asymmetric due to asymmetric accelerator output. Roback *et al.* used this type of liquid-filled matrix ionization chamber to verify the uniformity of the exit dose beneath a wedge and a step phantom for beams with missing tissue compensators [131].

In this paper we describe a method to determine the 2D *thickness* profile of a compensator, prior to clinical application, with an accuracy of 0.5 mm (1 SD). An error of 0.5 mm in thickness corresponds to a change in transmitted dose of 1% for a 10 MV beam. The method is based on the transmission through the compensator measured with a fluoroscopic, CCD camera based EPID (Philips SRI-100). This transmission array is used to derive the equivalent polystyrene thicknesses of the compensator along each rayline. The polystyrene thicknesses are then converted into the thicknesses of the compensator material. An advantage of using the transmission is that the method is not sensitive to long-term output and beam profile fluctuations of the linear accelerator.

7.2 Materials and Methods

7.2.1 Design and production of compensators

The compensators that are used in our institute consist of a Styrofoam mold filled with a granulate of stainless steel [161]. The filled mold is mounted between two lucite plates, which are screwed together. The mold and the lucite plates are attached to a tray which fits only in one

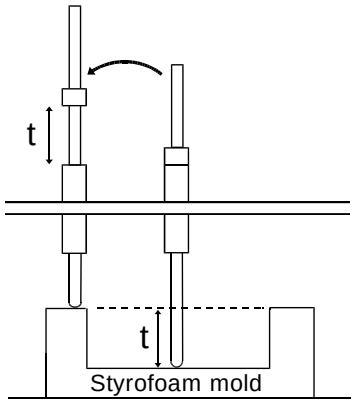

Figure 7.1. Setup to verify the depth of a Styrofoam mold.

way in the accessory tray of an MM50 racetrack microtron. The applied beam energy is 10 MV (quality index 0.704; the percent depth dose curve is similar to a 7 MV photon beam [21]). The distance between the focus and the entrance plane of the compensator is 71 cm. The maximum allowed thickness of the steel granulate is 3 cm. Required thicknesses of compensators are calculated using an in house developed inverse treatment planning algorithm. Outside the field the compensator thickness along each line parallel to the x-axis is set equal to the thickness at the corresponding field edge. The calculated thicknesses are transferred to a computer controlled milling device (PAR Scientific ACD$-$5) which mills out a cavity in the Styrofoam block. The vertical cutting inaccuracy of this device is specified to be ± 0.1 mm. The inaccuracy in the positioning of the Styrofoam block is estimated to be ± 0.5 mm. To prevent the drill from moving outside the Styrofoam block due to this positioning inaccuracy the minimal thickness of the steel granulate is set to 0.3 cm.

For this paper we used a simple setup (depicted in figure 7.1) for an independent verification of the depths of the milled out molds. In this way depths could be measured with an accuracy of ± 0.1 mm. The setup could only be used to measure mold depths in areas without a gradient. It was used to verify whether there was a systematic offset in the milled out profile.

7.2.2 Transmission measurements with the EPID

The transmission through a compensator is defined by

$$T(x, y) = \frac{D_p(x, y, \text{with compensator})}{D_p(x, y, \text{without compensator})}, \tag{7.1}$$

with $D_p(x, y)$ the portal dose in point (x, y) of the fluorescent screen. In our institute we use Philips SRI-100 EPIDs, which basically consist of a fluorescent screen, two mirrors and a CCD camera [164]. The focus to fluorescent screen distance of these EPIDs is fixed to 160 cm. The maximum detectable field size in the plane through the isocenter is 19×25 cm^2 [116], which is sufficient for our compensators used in the head and neck region. To reduce the detection of high energy electrons generated in the patient, we have mounted an additional 1 mm thick

stainless steel slab on the standard fluorescent screen. Image quality is hardly affected by this additional layer [85].

The raw EPID signals (G_{raw}) are not linearly related to the incident dose [116]. This is due to non-linear electronics of the EPID and due to differences in spectral sensitivity between an ionization chamber and the EPID. A third-order polynomial function derived from the on-axis measured response (G_{raw}/D_p) of the system is used to convert the raw EPID signals (G_{raw}) into corrected EPID signals (G).

We have previously described the characteristics of this EPID relevant for accurate and reproducible dose measurements in a 6 MV photon beam [61] and we have developed a method to derive portal dose images ($\mathbf{D}_p$) from corrected EPID images ($\mathbf{G}$), using a deconvolution method that corrects the measured EPID images for optical 'cross-talk' and (small) variations in local EPID sensitivity [116]. For transmission measurements, the field size for the EPID image with and without the compensators inserted is equal and therefore the correction for variations in EPID sensitivity is identical for both images. Furthermore, the effect of 'cross-talk' was expected to be similar. Therefore we have tested whether equation (7.1) can be approximated by

$$T(x, y) = \frac{G(x, y, \text{with compensator})}{G(x, y, \text{without compensator})}, \tag{7.2}$$

with $G(x, y)$ the measured pixel value at point (x, y), corrected for the non-linearity in the EPID response.

The validity of this equation was tested by comparing on-axis ionization chamber transmission measurements with EPID transmission measurements for flat, polystyrene absorbers. Transmissions were measured for a set of square fields ($w \times w$), absorber thicknesses (t) and distances from the exit plane of the absorber to the detector (L). The ionization chamber (PTW, N31002) was inserted in a mini phantom with a transverse cross section of 7×7 cm^2 and a thickness of 5 cm; this phantom was also used in other studies [115, 116]. The center of the ionization chamber was positioned at a depth of 2.0 cm. The mini phantom was positioned at the beam axis in the plane of the fluorescent screen, the distance between the surface and the focus was 158 cm. The data were acquired using the 10 MV photon beam of an MM50 racetrack microtron. The dose rate was set to 200 MU min^{-1} and measurements were performed with 150 MU. For the EPID measurements the camera gain was set to unity, the accumulation time on the CCD chip was set to 560 ms and the number of camera frames that where accumulated was set to 120. For noise reductions, each image was acquired twice and averaged. The parameters of the third-order polynomial function used to correct for the non-linear response of the EPID for 10 MV were 1, -0.0124, and 6.87×10^{-6}, respectively. Results are presented in section 7.3.1.

7.2.3 Derivation of the compensator thicknesses

The transmission $T(x, y)$ consists of a primary component $T^P(x, y)$, related to photons that have not interacted with the compensator, and a scatter component $T^S(x, y)$, originating from photons that are generated in interactions in the compensator. The primary component $T^P(x, y)$ is derived from the measured transmission $T(x, y)$ using

$$T^P(x, y) = T(x, y) - T^S(x, y), \tag{7.3}$$

with $T^S(x, y)$ the calculated scatter component of the transmission, using the intended compensator thicknesses as input. $T^P(x, y)$ is only related to the radiological thickness of the compensator along the corresponding ray line. Using a measured relationship between the radiological compensator thickness and the primary component of the transmission the thickness of the compensator along each ray line is derived. Off-axis variations in beam quality are taken into account.

7.2.3.1 Calculation of $T^S(x, y)$.

$T^S(x, y)$ is calculated using an algorithm developed to predict the transmission through patients for *in vivo* dosimetry [115]. The intended compensator is substituted by an (imaginary) equivalent homogeneous phantom (EHP) consisting of polystyrene (PS). Along each ray line, the thickness of the EHP (t_{PS}) is equal to the corresponding radiological thickness of the compensator. The relation for this thickness is

$$t_{\mathrm{PS}} = \frac{\mu_{\mathrm{steel}}}{\mu_{\mathrm{PS}}} t_{\mathrm{steel}} + \frac{\mu_{\mathrm{lucite}}}{\mu_{\mathrm{PS}}} t_{\mathrm{lucite}}, \tag{7.4}$$

with t_{steel} the thickness of the granulate of stainless steel, t_{lucite} the thickness of the two lucite plates of the tray and μ_{steel}, μ_{PS} and μ_{lucite} the linear attenuation coefficients of the primary component of the transmission for steel, polystyrene and lucite, respectively. The ratio $\mu_{\mathrm{lucite}}/\mu_{\mathrm{PS}}$ is 1.12 [115]. The ratio $\mu_{\mathrm{steel}}/\mu_{\mathrm{PS}}$ has been derived from measurements described in section 7.2.3.3. The radiological thickness of the Styrofoam mold is neglected.

The distance between the exit plane of the compensator and the fluorescent screen of the EPID ($\sim$ 87 cm) is larger than the distance between a patient and this screen. To be able to calculate $T^S(x, y)$ with the input data that are also used for transmission predictions through patients, the EHP of the compensator is shifted such that the distance between the exit plane and the screen is 60 cm. The resulting overestimation of the scatter component is corrected using the inverse square law. The database used for transmission predictions through patients contains input data for L ranging from 40 to 60 cm, for prediction of $T^S(x, y)$ for compensators only a sub-set (L=60 cm) of this database is required.

7.2.3.2 Derivation of $t_{\mathrm{steel}}(x, y)$ from $T^P(x, y)$

The thickness of the granulate of stainless steel, $t_{\mathrm{steel}}(x, y)$, is derived in a step process. In the first step, $T^P(x, y)$ is used to determine the equivalent polystyrene thickness $t_{\mathrm{PS}}(x, y)$ of the compensator. In the second step this thickness is converted into a stainless steel thickness.

To determine the equivalent polystyrene thickness $t_{\mathrm{PS}}(x, y)$ corresponding to the derived primary component $T^P(x, y)$, $T^P(x, y)$ is first converted into the *on*-axis primary component corresponding to the equivalent polystyrene thickness of the compensator at point (x, y), $P(t_{\mathrm{PS}}(x, y))$. The relation between these two components is [115]

$$P(t_{\mathrm{PS}}(x, y)) = \frac{T^P(x, y)}{C_{\mathrm{open}}(r(x, y), t^{\mathrm{i}}_{\mathrm{PS}}(x, y))}, \tag{7.5}$$

with $t^{\mathrm{i}}_{\mathrm{PS}}(x, y)$ the *intended* equivalent polystyrene thickness (calculated with equation (7.4)) and $t_{\mathrm{PS}}(x, y)$ the measured equivalent polystyrene thickness. $C_{\mathrm{open}}(r(x, y), t^{\mathrm{i}}_{\mathrm{PS}}(x, y))$ is a

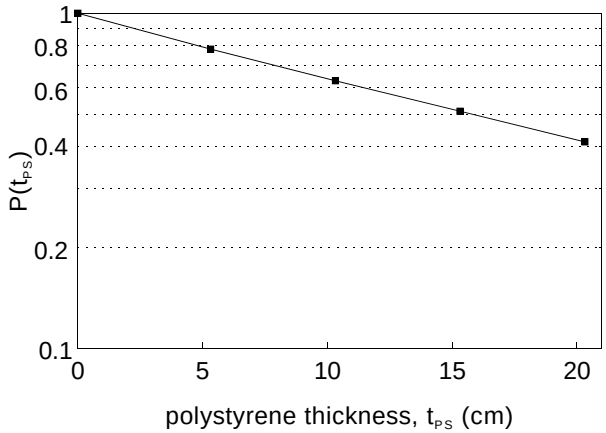

Figure 7.2. The on-axis primary component of the transmission as a function of the polystyrene absorber thickness for the 10 MV beam of an MM50 racetrack microtron

function to account for the difference in beam quality between the beam axis and the off-axis point (x, y) at a distance $r(x, y) = \sqrt{x^2 + y^2}$ from the beam axis. Derivation of this function from measured data is explained in another paper [115].

For each point the thickness $t_{\mathrm{PS}}(x, y)$ is calculated from the derived on-axis primary component, $P(t_{\mathrm{PS}}(x, y))$, using a measured relationship between the thickness of a polystyrene absorber and the on-axis primary transmission, $P(t_{PS})$, derived from the input database. $P(t_{\mathrm{PS}})$ for the applied 10 MV beam is depicted in figure 7.2. Finally, the thickness of the granulate of stainless steel, $t_{\mathrm{steel}}(x, y)$, is derived from $t_{\mathrm{PS}}(x, y)$, using equation (7.4).

The derived thicknesses could be used to repeat the above described process iteratively, but this would only affect the scatter component, which contributes less than 4% to the transmission, and the function $C_{\mathrm{open}}(r(x, y), t_{\mathrm{PS}}(x, y))$, which depends only slightly on thickness (for the 10 MV beam of the MM50 a difference of 1 cm stainless steel corresponds to a change of C_{open} of less than 0.5%). As described in section 7.3.2 one iteration is sufficient to derive compensator thicknesses to within 0.5 mm (1 SD).

7.2.3.3 Derivation of the ratio $\mu_{\mathrm{steel}}/\mu_{\mathrm{PS}}$

The ratio $\mu_{\mathrm{steel}}/\mu_{\mathrm{PS}}$ is used for the conversion of stainless steel thicknesses into the equivalent polystyrene thicknesses (see section 7.2.3.1). It was derived from on-axis measured transmissions through flat compensators of 2.00 cm and 3.02 cm thickness (the thicknesses were measured with the setup depicted in figure 7.1), irradiated with fields of 8×18 and 18×18 cm^2. To achieve maximum accuracy, these transmission measurements were performed with an ionization chamber using the setup described in section 7.2.2. Measurements were performed with 150 MU and dose rate was set to 200 MU min^{-1}. The thickness of the two lucite tray holders (t_{lucite}) was 0.91 cm, which corresponds to an equivalent polystyrene thickness (using equation (7.4)) of 1.02 cm.

The radiological thickness of the compensator was derived from the measured transmissions using the method described in the previous sections. For calculation of the EHP of the

Table 7.1. Derivation of the ratio $\mu_{\text{steel}}/\mu_{\text{PS}}$ from on-axis measured transmissions through two flat compensators.

t_{steel} [cm]	field size [cm^2]	T [−]	T^S [−]	T^P [−]	$< T^P >$ [−]	t_{PS} [cm]	$\frac{\mu_{\text{steel}}}{\mu_{\text{PS}}}$ [−]
3.02	8×18	0.5219	0.0064	0.5155	0.5162	14.90	4.600
	18×18	0.5320	0.0152	0.5169			
2.00	8×18	0.6377	0.0063	0.6314	0.6319	10.23	4.606
	18×18	0.6463	0.0139	0.6324			
						mean:	4.603

compensators a first approximation of the ratio $\mu_{\text{steel}}/\mu_{\text{PS}}$ of 4.5 was used, based on the density of the filling material [161]. With equation (7.4) the ratio $\mu_{\text{steel}}/\mu_{\text{PS}}$ was derived from the measured radiological thicknesses. Results are presented in table 7.1.

7.3 Results

7.3.1 EPID transmission measurements

To verify the accuracy of the EPID transmission measurements they have been compared with on-axis transmission measurements with an ionization chamber using the setup described in section 7.2.2. The EPID signals were corrected for the non-linear response of the system. The $T(w, t, L)$ set that was measured contains all possible combinations of

w = 3, 10, 18 cm,
t = 10, 20, 30 cm, and
L = 40, 50, 60 cm.

The EPID and ionization chamber transmission measurements for all these situations agreed within $-0.2 \pm 0.5\%$ (1 SD). The short term reproducibility of the ionization chamber transmission measurements was 0.3% (1 SD), hence the short term reproducibility of the EPID transmission measurements was 0.4% (1 SD). Using raw EPID signals (G_{raw}) resulted in a deviation between EPID and ionization chamber transmission measurements of $-1.0 \pm 1.3\%$ (1 SD).

7.3.2 Compensator thicknesses measured with the EPID

To verify the accuracy of the developed method for compensator thickness verification, the compensator thicknesses derived from EPID measurements were compared with intended thicknesses, for molds containing areas without a gradient the intended depth was verified using the method described in section 7.2.1. Data are presented for four compensators: (i) a flat 1 cm thick compensator, (ii) a spherical compensator (figure 7.3), (iii) a wedge-shaped compensator and (iv) a clinical compensator (figure 7.7). All compensators were irradiated with a square 16×16 cm^2 field. Image aquisition was performed with the EPID settings described in section 7.2.2. Field sizes, coordinates and distances to the beam axis are all defined in the plane through the isocenter (i.e. at 100 cm from the focus). EPID images were corrected for the

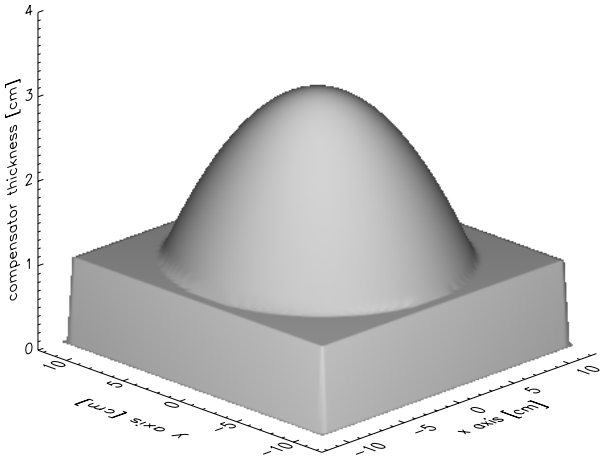

Figure 7.3. Spherical compensator.

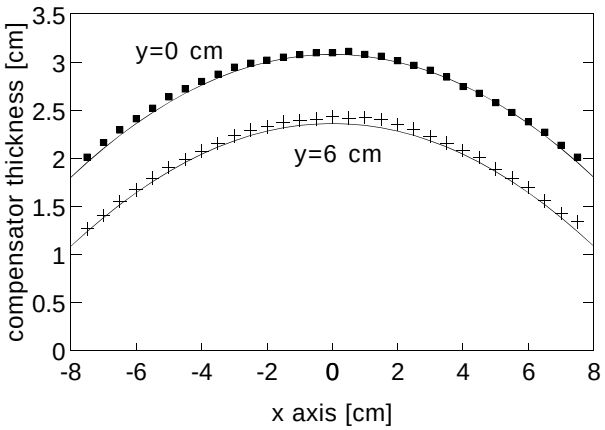

Figure 7.4. Measured (markers) and realized (lines) thicknesses of the spherical compensator depicted in figure 7.3, along the y=0 and y=6 cm axes.

non-linear response of the system and resampled to arrays of 64 × 64 elements; each element represents a region of interest of 0.5 × 0.5 cm^2.

Using the setup described in section 7.2.1 it was found that the thickness of the flat compensator was 1.04 cm instead of the intended 1.00 cm. In the central 14 × 14 cm^2 part of the beam, the mean deviation between the thickness measured with the EPID and the realized thickness of 1.04 cm was 0.2 ± 0.2 mm (1 SD).

The realized on-axis thickness of the spherical compensator (depicted in figure 7.3) was 3.08 cm, which decreased to 1.08 cm at r=10 cm, for $r \geq 10$ cm the thickness was 1.08 cm. These thicknesses have been measured using the setup described in section 7.2.1. The mold was

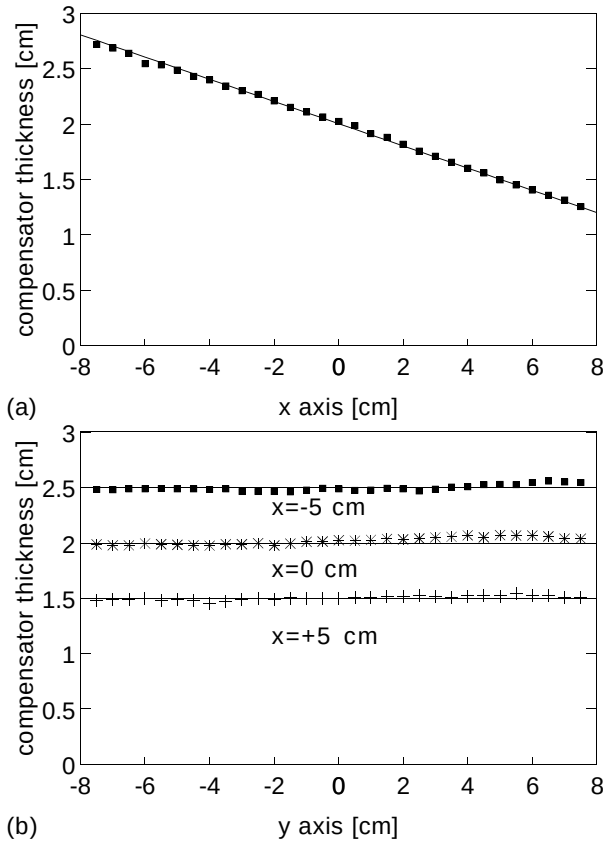

Figure 7.5. (a) Compensator thicknesses measured with the EPID (markers) compared with the intended thicknesses (lines) (a) along the x-axis and (b) along the y-axis for $x = -5$, 0 and 5 cm for a wedge-shaped compensator.

0.08 cm deeper than intended. Cross sections along the y=0 and y=6 cm axis of the measured and realized thickness of the spherical compensator are depicted in figure 7.4. Within the central 14×14 cm^2 part of the beam, the mean deviation between the measured and realized thickness was 0.4 ± 0.3 mm (1 SD).

The wedge-shaped compensator had an intended thickness of 3 cm at $x = -10$ cm which decreased to 1 cm at x =10 cm and was symmetrical in the y-direction. Due to the gradient in the mold, the actual depths could not be verified independently. Results are presented in figures 7.5a and 7.5b. The mean deviation between the measured and intended thicknesses within the radiation field, but outside the penumbra region, was 0.1 ± 0.3 mm (1 SD).

The clinical compensator designed for elective treatment of the neck is depicted in figure 7.6. The minimal thickness was 1 cm. To verify the realized thickness it was irradiated with the 16×16 cm^2 field. For patient treatment a smaller, assymetrical conformal field is used. Measured and intended thicknesses agreed within 0.0 ± 0.4 mm (1 SD). Results are depicted in figure 7.7; points outside the patient field were excluded.

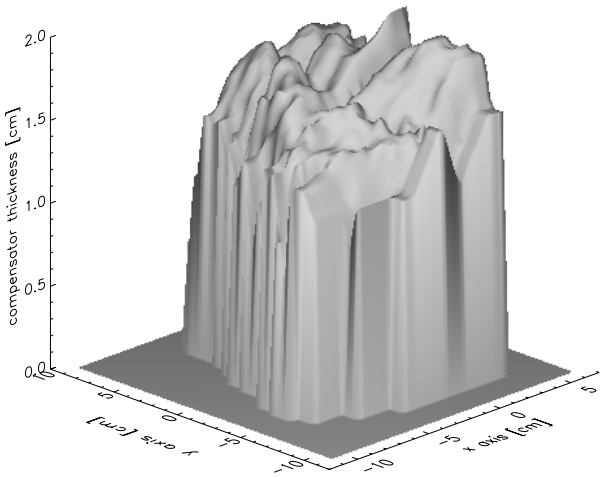

Figure 7.6. Clinical compensator.

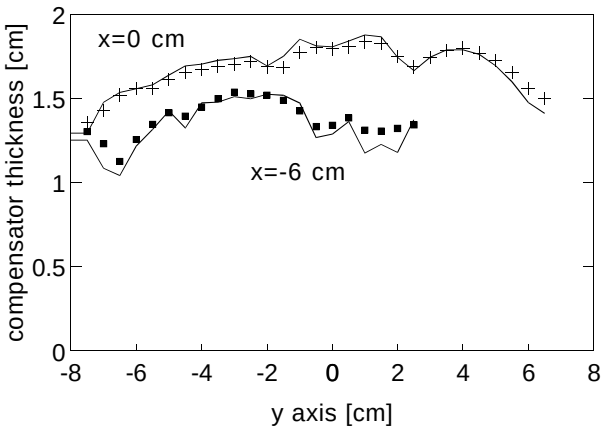

Figure 7.7. Measured (markers) and intended thicknesses (lines) of the clinical compensator depicted in figure 7.6, along the lines through points $x = 0$ cm and $x = -6$ cm parallel to the y-axis.

7.4 Discussion and conclusions

An accurate method has been developed for measuring the thickness of compensators with an EPID. Using a fluoroscopic EPID, the mean deviation between the intended and measured thicknesses for the four compensators was 0.2 ± 0.3 mm (1 SD). The accuracy of determined thicknesses of the steel granulate is estimated to be at least 0.5 mm (1 SD). The accuracy is limited by the accuracy of the EPID transmission measurements of 0.4% (1 SD), corresponding to an error in the derived thicknesses of 0.2 mm (1 SD). A difference in thickness of 0.5 mm

corresponds to a change in the transmitted dose of about 1% for a 10 MV beam, the accuracy of the method is thus sufficient.

In clinical practice the developed method can be used to verify the thicknesses of a compensator before the patient is treated. If a square radiation field is applied that encompasses the fields used for patient treatment, inaccurate transmission measurements in the beam penumbra can be avoided. In this way accurate thickness verification of the whole compensator is achieved, including areas close to the clinical field borders. An image of the field without compensator inserted only has to be acquired once and then all compensators that need to be verified can be irradiated. Systematic deviations between the intended and measured thicknesses can be corrected by adjusting the number of monitor units. Non-systematic deviations point at the use of the wrong compensator (designed for an other field or patient) or a manufactering error.

The applied procedure for the prediction of the scatter component was originally developed for patients for which the distance between the exit plane and the detector can be as small as 40 cm [115]. The distance between the exit plane of the compensator and the detector is about 87 cm, which results in a scatter component that contributes less than 4% to the transmission. Hansen *et al*. [60] have developed a simpler method to estimate the scatter component for these large exit plane to detector distances, based on the work of Swindell and Evans [150]. We have not used this method, since we already had an accurate method.

Acknowledgments

This work was financially supported by the Dutch Cancer Society (Grant DDHK 94-848).

Chapter 8

Dosimetric verification of intensity modulated beams produced with dynamic multileaf collimation using an electronic portal imaging device

Kasper L. Pasma, Maarten L.P. Dirkx, Marco Kroonwijk, Andries G. Visser
and Ben J.M. Heijmen
Submitted to *Med. Phys.*

Dose distributions can often be significantly improved by modulating the two-dimensional intensity profile of the individual x-ray beams. One technique for delivering intensity modulated beams is dynamic multileaf collimation (DMLC). However, DMLC is complex and requires extensive quality assurance. In this paper a new method is presented for a pretreatment dosimetric verification of these intensity modulated beams utilizing a charge-coupled device (CCD) camera based fluoroscopic electronic portal imaging device (EPID). In the absence of the patient, EPID images are acquired for all beams produced with DMLC. These images are then converted into two-dimensional dose distributions and compared with the calculated dose distributions. The calculations are performed with a pencil beam algorithm as implemented in a commercially available treatment planning system using the same absolute beam fluence profiles as used for calculation of the patient dose distribution. The method allows an overall verification of (i) the leaf trajectory calculation (including the models to incorporate collimator scatter and leaf transmission), (ii) the correct transfer of the leaf sequencing file to the treatment machine and (iii) the mechanical and dosimetrical performance of the treatment unit. The method was tested for intensity modulated 10 and 25 MV photon beams; both model cases and real clinical cases were studied. Dose profiles measured with the EPID were also compared with ionization chamber measurements. In all cases both predictions and EPID measurements and EPID and ionization chamber measurements agreed within 2% (1 σ). The study has demonstrated that the proposed method allows fast and accurate pretreatment verification of DMLC.

8.1 Introduction

Dose distributions delivered by multiple field irradiation techniques can often be significantly improved by modulating the two-dimensional intensity profile of the individual x-ray beams [15, 19, 20, 75, 76, 138, 166–168]. Intensity modulated (IM) beam profiles, calculated by means of inverse treatment planning, can be realized in several ways. One technique is the use of dynamic multileaf collimation (DMLC). So far, the 'sliding window' technique in combination with DMLC has received most attention in the literature. This technique is based on moving each leaf pair of a multileaf collimator (MLC) independently but unidirectionally across the treatment field while the beam is on, effectively sweeping apertures of variable widths across the treatment field. The width of the aperture varies between leaf pairs. Moreover, for each leaf pair the width is also a function of time. Convery and Rosenbloom have described the basic algorithm to calculate the required leaf trajectories; the algorithm has the form of an optimization problem in which the beam on time is minimized [27]. Three groups have independently developed analytical equations to calculate the leaf trajectories [139, 140, 148], which were further developed by others [38, 162, 170]. Compared to the algorithm of Convery and Rosenbloom computation times of the analytical approaches are much shorter. The first group of patients were irradiated using DMLC in 1995 at Memorial Sloan-Kettering Cancer Center, NY [93]. Recently, treatment of head and neck cancer patients with DMLC has started in our clinic.

A disadvantage of the dynamic technique is that it is difficult to verify due to its complexity. Bortfeld *et al*. have therefore proposed to produce intensity modulated beams by superpositioning a number of partially overlapping, static, irregularly shaped fields produced with the MLC [16]. Controlling the delivery of a sequence of small doses and static leaf settings was considered to be a straightforward extension of existing linear accelerator control. However, in contrast with DMLC [38, 162, 170], a method to avoid tongue-and-groove underdosage has not yet been described for the static technique.

For verification of segmented beam delivery Curtin-Savard and Podgorsak proposed the use of the scanning liquid ionization chamber EPID [33]. Without a patient in the beam, portal images were acquired for each subfield of the leaf sequence and converted into a dose rate distribution. Subsequently, the images were converted into absolute dose distributions by multiplication with the corresponding monitor unit setting. Finally, the individual dose distributions were summed to produce a dose distribution at the measurement depth. These distributions were then compared with dose distributions predicted by a treatment planning system. Because of the use of the monitor unit setting, the comparison with the dose distribution of the planning system is basically a verification of the relative dose distribution. The applied EPID is relatively slow in returning to the initial state. Therefore, they had to apply a 60 s rest interval between measurement of subsequent segments, yielding long overall measurement times of typically one hour. Due to the scanned signal readout and the measurement of dose rate instead of dose, the applied EPID is not suitable for high precision dosimetric verification of DMLC.

To test the reproducibility and accuracy of DMLC, the use of film has been reported [22, 94, 165]. At Memorial Sloan-Kettering Cancer Center film dosimetry is performed in a flat homogeneous phantom for each field prior to the first treatment. Measured dose distributions are compared with corresponding calculated dose distributions [94]. A disadvantage of film dosimetry is that it is time consuming since it requires developing and scanning of the film,

furthermore a sensitometric curve is needed to convert optical densities into doses.

CCD camera based EPIDs are a promising tool for verification of DMLC due to their high data acquisition rate and capability to measure simultaneously in all points of the treatment field [5, 96, 112, 116]. Balter *et al.* showed preliminary results of a method to derive leaf positions in each camera frame acquired during treatment and to compare them with a table of prescribed leaf positions [5]. Leaf positions could be determined with an accuracy of 0.6 mm and a duty cycle of less than 1 s. A similar approach was implemented by Partridge *et al.* [112] They used a custom made EPID with image acquisition synchronized to the accelerator magnetron current pulse production, with one CCD camera frame acquired per accelerator pulse. Data were presented for a 6 MV beam. The accuracy of the leaf position measurements was 2 mm. Due to a limitation of the camera triggering hardware the pulse rate of the linac had to be reduced. Ma *et al.* calculated normalized reference images from MLC leaf sequencing files and compared these with normalized images measured with a fluoroscopic beam imaging system (BIS, Wellhöfer Dosimetrie, Schwarzenbruck, Germany) for a 6 MV photon beam [96]. This imaging system can be fastened to the blocking tray holder of a linear accelerator. It was especially designed for quality control tasks. For the calculation of the reference images a measured portal image of a large open field was used. The reference images were therefore not only related to the prescribed fluence, but also contained optical distortions in the EPID system. A global correlation coefficient was used to compare the calculated reference image with the image measured with the BIS system. This method can be used to verify whether the leaf sequencing files have been transferred correctly to the linac control computer and whether the treatment can be correctly executed without machine faults. Transmission through the leaves (both intraleaf and interleaf) was not taken into account and a simple empirical method was used to model extrafocal scatter. Despite these limitations, they concluded that it was possible to detect uncertainties of less than 0.5 mm in leaf position during DMLC.

The above described methods to verify leaf motion cannot be used to check whether the calculated leaf trajectories do indeed generate the absolute beam fluence profiles used in treatment planning. In this paper a new method is presented for a pretreatment verification of these absolute beam fluence profiles utilizing a commercially available CCD camera based fluoroscopic EPID. In the absence of the patient EPID images are acquired for all beams produced with DMLC. These images are then converted into two-dimensional dose distributions and compared with calculated dose distributions. The calculations are performed with a pencil beam algorithm as implemented in a commercially available treatment planning system (TPS) using the same absolute beam fluence profiles as used in the TPS for calculation of the patient dose distributions. In this paper results are presented for intensity modulated 10 and 25 MV photon beams; both model cases and real clinical cases were studied. Absolute dose profiles measured with the EPID were also compared with ionization chamber measurements. Preliminary results on measurements of absolute dose distributions in IM fields produced with DMLC have been reported [116].

8.2 Materials and Methods

8.2.1 EPID and ionization chamber dose measurements

The applied EPID was a Philips SRI-100 (Philips Medical Systems, Crawley, UK), which basically consists of a fluorescent screen, two mirrors and a CCD camera. The fluorescent

screen is a 1.65 mm thick stainless steel plate coated with a layer of gadolinium oxysulphide. To reduce the detection of high-energy electrons generated in patients, an extra 1 mm thick stainless steel slab has been mounted on the standard fluorescent screen [116]. The added slab hardly affects the image quality [85]. The acquired images may be used both for set-up verification and for *in vivo* dosimetry [84]. The EPID has a fixed focus to fluorescent screen distance of 160 cm. Technical details of the EPID have been described by Visser *et al*. and Althof *et al.* [2, 164]

Image acquisition is performed with a procedure written in the macro command language that comes with the system. The integration time on the CCD chip was set to 240 ms and 120 camera frames were accumulated in the frame store memory. The read out time needed to transmit a frame from the CCD to the frame grabber (during which no signal is accumulated) is 80 ms. The final image is the mean of the integrated camera frames, corrected for the dark current measured prior to the irradiation. In the original procedure image acquisition starts automatically when the measured pixel values in the center of the camera frame exceed a threshold, i.e. when the beam is switched on. For the DMLC measurements described in this paper image acquisition was started manually, since with the sliding window technique the pixels in the center of the image are blocked by the leaves when the irradiation starts. The procedure is discussed in detail in another paper [116].

Due to sagging of the EPID structure the field center can shift slightly. To correct the image for this shift the position of the field center was derived using the position of the field borders in an EPID image of a (static) square field, which is stored in a lookup table. The raw EPID images of 512×256 pixels were then resampled to arrays of 64×64 elements; each element represents a region of interest with an area of 0.5×0.5 cm^2 projected at isocenter. Conversion of these arrays into absolute dose distributions was performed in three steps. Acquired images were first corrected for the non-linear response of the system [116, 125]. Subsequently, the image was corrected for the optical 'cross talk' by deconvolving it with a point spread function [61, 116]. Finally, the resulting array was divided by an array that accounts for relative EPID sensitivity [116]. The system was calibrated once. The observed day-to-day variation of the EPID response per unit of delivered dose is 0.4% (1 σ) [61]. Due to radiation damage to the CCD chip the EPID response gradually decreases ($\sim$ 3%/year) [122]. This decrease was carefully monitored and corrected for using the daily acquired images for the quality control of the absolute output and field flatness of the scanning photon beams of the MM50 [39] and the two weekly output checks with an ionization chamber.

Dose measurements were also performed with a N31002 ionization chamber (PTW, Freiburg, Germany). The ionization chamber was inserted in a polystyrene mini phantom [115] at a depth of 2.0 cm for the 10 MV beam and at 2.5 cm for the 25 MV beam. For those depths it was experimentally found that the variations in the on-axis response of the EPID (EPID pixel value/portal dose measured with the ionization chamber (G/D_p)) were minimal for field sizes ranging from 3×3 up to 18×18 cm^2 and polystyrene absorber thicknesses ranging from zero up to 35 cm. For a 25 MV photon beam the mean of the standard deviations of the EPID response for all field sizes was 0.4% [116]. The mini phantom was scanned in an empty RFA-300 water phantom (Scanditronix Medical AB, Uppsala, Sweden) with the center of the ionization chamber positioned at a distance of 160 cm from the focus, which is equal to the fixed focus to fluorescent screen distance of the EPID.

8.2.2 Calculation of the dose distribution at the detector

Starting point for the calculation of the dose distribution at the fluorescent screen of the detector is the optimized beam fluence $F_{\text{opt}}(x, y)$ (in MU) to be delivered at position (x, y), which is the result of a computer optimization or inverse treatment planning. A fluence of 1 MU corresponds to the fluence due to an irradiation that results in a dose delivery of 1 cGy at a depth of dose maximum in water with a source surface distance (SSD) of 100 cm in a static 10×10 cm^2 field. Using an iterative algorithm described by Dirkx *et al.* leaf trajectories are then calculated taking into account collimator scatter and the effective leaf transmission, which is the sum of the transmission through the leaves and the extra focal radiation under the moving leaves [38]. The algorithm fully avoids tongue-and-groove underdosage effects [162]. Generally less than 10 iterations are necessary to minimize the difference between optimized ($F_{\text{opt}}(x, y)$) and realized fluence profiles ($F(x, y)$), which are used for calculation of the final dose distribution in the patient with the CadPlan 3D TPS (Varian-Dosetek, Espoo, Finland).

The expected absolute dose distribution in the plane of the fluorescent screen of the EPID, $D_{p,0}(x, y)$, is calculated from the realized fluence profile using the pencil beam algorithm as implemented in the CadPlan TPS [142, 143]. In the current implementation (CadPlan v2.7.9) the penumbra width is a linear function of the SSD. As a result the predicted dose distributions would become inaccurate for the SSD of the detector (160 cm), which is much larger than the SSDs clinically used. Therefore, the dose distribution is calculated at 100 cm from the focus by enlarging the field with a factor of 1.6 (160/100). The dose distribution is then normalized using the calculated on axis dose in a static 16×16 cm^2 field for 150 MU. Finally, the absolute dose distribution is calculated using the measured cGy/MU value at the detector for a 10×10 cm^2 field. Dose calculations and the calibration measurement are performed at a water depth of 2 cm for the 10 MV photon beam and at a depth of 2.5 cm for the 25 MV beam, equal to the effective measuring depths of the EPID, as discussed in the previous section.

8.2.3 Realization and verification of fluence profiles

Measured and predicted dose distributions $D_{p,0}(x, y)$ were compared for the 10 and 25 MV photon beams of the MM50 racetrack microtron (Scanditronix Medical AB, Uppsala, Sweden). The dose rate was 200 MU min^{-1} for the 10 MV beam and 300 MU min^{-1} for the 25 MV beam. The microtron produces 200 radiation pulses per second (pps). The unit is equipped with a double-focused multileaf collimator with 32 leaf pairs. Projected at isocenter the leaf width is 1.25 cm. The maximum leaf speed is 1 cm s^{-1}. For all measurements the leaves moved from left to right parallel to the x-axis. During DMLC, every 50 ms the accelerator control system compares the actual leaf positions, measured with potentiometers, with the prescribed positions. If the deviation between a prescribed and a measured position is more than 0.2 cm during three subsequent checks, the irradiation is interrupted. Realization of IM fluence profiles with this unit is discussed in detail elsewhere [38].

The developed method was tested for a range of fluence profiles, both model cases and real clinical cases were studied. Calculated absolute dose distributions (section 8.2.2) were compared with dose distributions derived from EPID images and with dose profiles measured with an ionization chamber (section 8.2.1). The axes for comparisons in the leaf direction were chosen at the center of each leaf pair ($y = \pm 0.6, \pm 1.9, \pm 3.1, ..$). Throughout the paper positions and distances are defined at the plane normal to the beam axis at 100 cm from

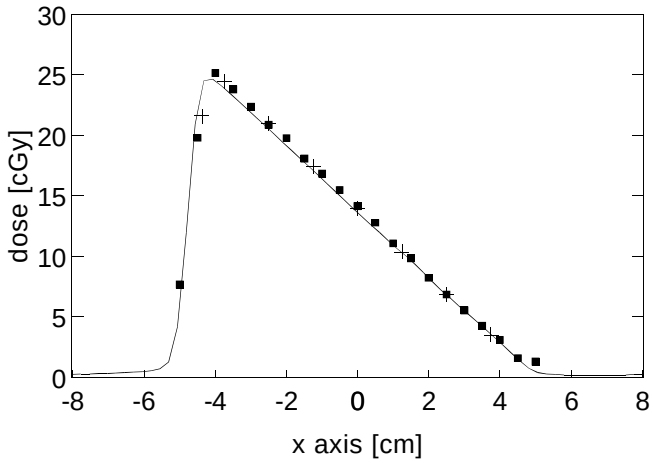

Figure 8.1. Predicted (line) and measured absolute dose (■ EPID, + ionization chamber) along the $y = 0.6$ cm axis for a wedge profile produced with DMLC using the 10 MV photon beam.

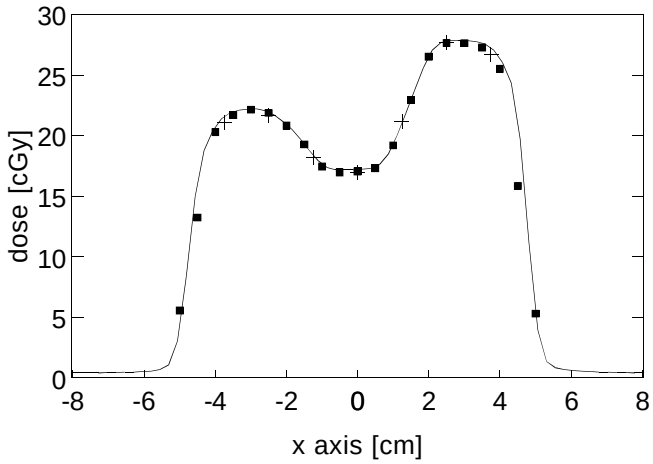

Figure 8.2. Predicted (line) and measured absolute dose (■ EPID, + ionization chamber) along the $y = 0.6$ cm axis for an IM 10 MV beam.

the focus. The reported differences are the mean deviation in percent and the corresponding standard deviation in percent (mean $\pm$ 1 σ[%]).

8.3 Results

In figures 8.1 and 8.2 data are presented for intensity modulated 10 MV beams. Within the treatment field the leaf trajectories were identical for all leaf pairs; the presented data are for $y = 0.6$ cm. Outside the penumbra, there is an excellent agreement between EPID and ionization chamber measurements ((EPID-ionization chamber)/ionization chamber) for both

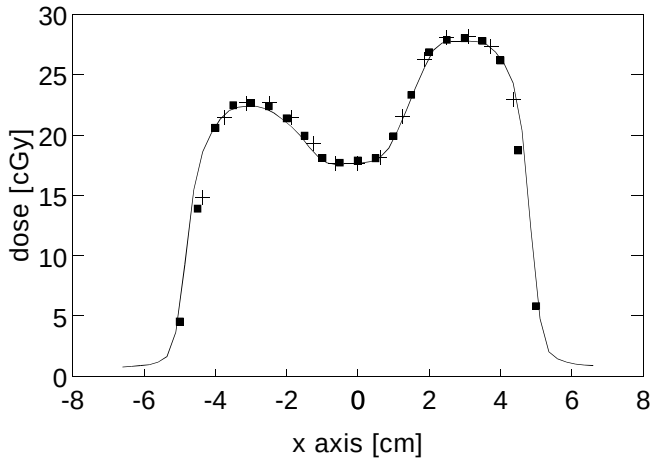

Figure 8.3. Predicted (line) and measured absolute dose (■ EPID, + ionization chamber) along the $y = 0.6$ cm axis for an IM 25 MV beam.

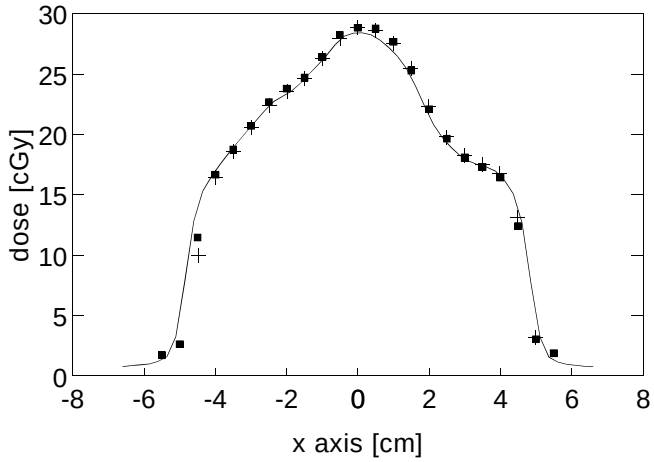

Figure 8.4. Predicted (line) and measured absolute dose (■ EPID, + ionization chamber) along the $y = 0.6$ cm line for an IM 25 MV beam.

beams: $0.3 \pm 0.6\%$ (figure 8.1) and $0.1 \pm 0.8\%$ (figure 8.2). The actual agreement may even be slightly better, since each ionization chamber measurement required the complete irradiation to be repeated. The short term reproducibility of the absolute dose delivery with DMLC at the MM50 racetrack microtron is 0.2% [40]. The deviations between the calculated dose profile and the profile measured with the EPID are $-2.1 \pm 1.2\%$ and $0.9 \pm 0.8\%$, respectively.

The data presented in figure 8.3 are for a beam *fluence* profile that was also used to generate the data in figure 8.2, but now realized with the 25 MV beam. Again deviations between EPID and ionization chamber measurements are small: $-0.2 \pm 1.3\%$. The deviation between the predicted dose profile and the profile measured with the EPID is $-1.0 \pm 0.7\%$. Similar results were found for the profile presented in figure 8.4: $0.2 \pm 1.0\%$ and $-1.0 \pm 1.4\%$, respectively.

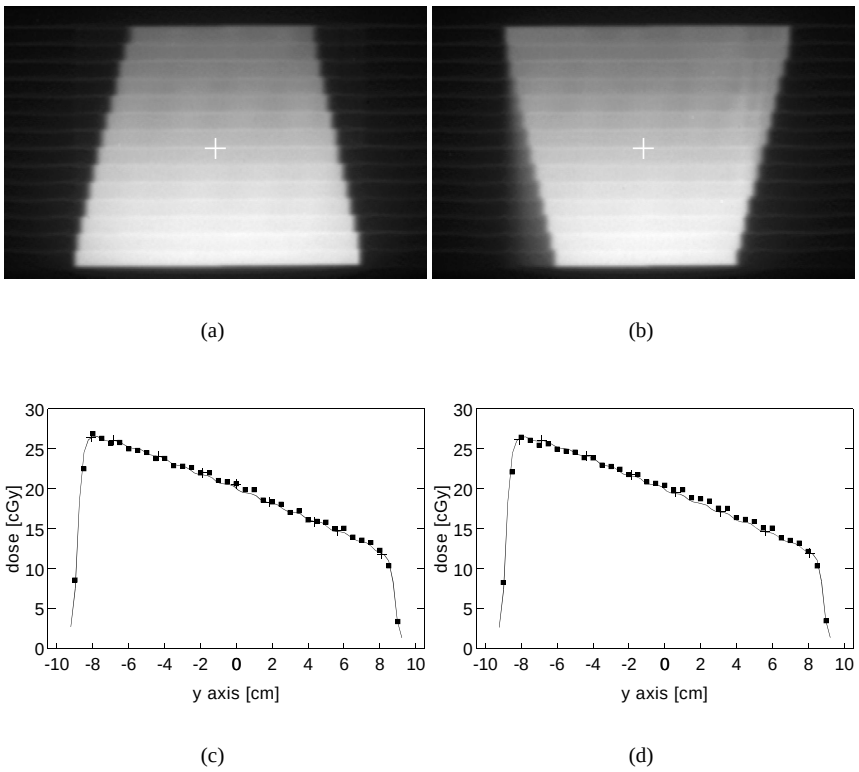

Figure 8.5. Raw EPID images of IM 25 MV photon beams are shown in (a) and (b). In (c) and (d) the corresponding measured (■ EPID, + ionization chamber) and predicted (line) absolute dose profiles along the *y*-axis (normal to the axis along which the leaves move) are shown.

In figures 8.5a and b acquired EPID images (512 × 256 pixels) for two non-square IM 25 MV beams are shown. The fluence decreases in the *y*-direction; the dose at the top of the image is a factor of 2.2 lower than at the bottom. Due to the synchronization of leaf trajectories of adjacent leaves, underdosage (lower pixel values) do not occur in the overlap regions [162]. The small overdosage (higher pixel values) in the overlap regions of adjacent leaves are due to the interleaf leakage of about 2% [38]. These overdosages can be avoided using partial synchronization [170]. Figures 8.5c and d show cross sections along the *y*-axis (normal to the axis along which the leaves move) of the two-dimensional dose profile derived from the EPID images shown in figures 8.5a and b. Corresponding predicted dose profiles and dose profiles measured with an ionization chamber are included. For the first field (figure 8.5a) the deviation between EPID and ionization chamber measurements was $0.2 \pm 1.1\%$ and for the second field (figure 8.5b) $0.4 \pm 2.0\%$. The deviations between the predicted profile and the EPID measurements were $-0.9 \pm 1.7\%$ and $-1.4 \pm 1.7\%$, respectively. Standard deviations are slightly increased due to the interleaf leakage that was measured but not taken into account in the calculations. Under the center of the leaves the deviations are $-0.7 \pm 1.2\%$ and $-0.4 \pm 1.6\%$,

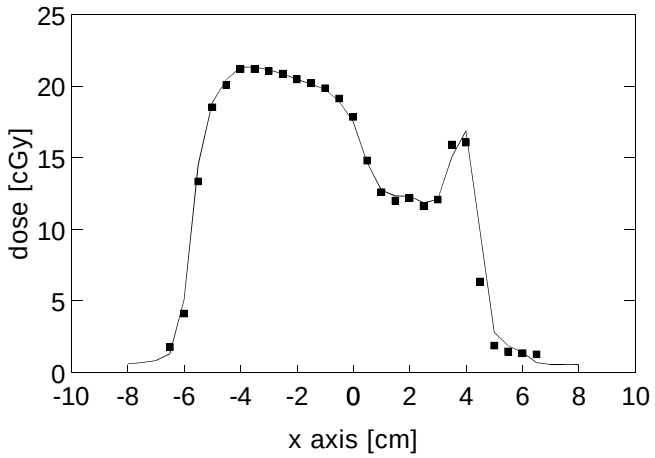

Figure 8.6. Predicted (line) and with the EPID measured (■) absolute dose profile along the y=-1.9 cm axis of a lateral IM 25 MV photon beam for a prostate cancer patient.

respectively.

In figure 8.6 results are presented for a two-dimensional IM profile designed for treatment of a prostate cancer patient. The deviation between the predicted profile and the profile measured with the EPID is $0.5 \pm 1.1\%$.

8.4 Discussion and conclusions

A procedure for pretreatment verification of absolute beam fluence profiles realized with DMLC was developed and tested. The time required to verify an IM beam is about 2 minutes, which is much shorter than any other dosimetric technique. The EPID system only has to be calibrated once. The agreement between calculations and EPID measurements and between EPID and ionization chamber measurements was within 2% (1 σ). The procedure allows an overall verification of (i) the leaf trajectory calculation (including the models to incorporate collimator scatter and leaf transmission), (ii) the correct transfer of the leaf sequencing file to the treatment machine and (iii) the mechanical and dosimetrical performance of the treatment unit. It is not always possible to distinguish between these types of errors using only portal images. Previously published DMLC verification methods with EPIDs only verified leaf motion [5, 112] or relative dose profiles [96]. The excellent agreement between EPID and ionization chamber measurements in all cases, shows that the read out time of 80 ms (during which no signal is collected) has no detectable effect; the data acquisition rate is sufficiently high [96].

In the near future the developed method will be extended to enable verification of DMLC during patient treatment. Acquisition of portal images suitable for dosimetric verification of DMLC can be fully integrated into existing imaging routines for patient set-up verification, without introducing an increase in the overall treatment time [84]. Preliminary results on measurements of portal dose images (PDI), i.e. the dose distribution behind a patient in a plane normal to the beam axis, in an IM beam have been reported [116]. The calculation of a PDI for a patient irradiated with an IM beam is a relatively simple extension of existing methods [115]. The relation is $D_p(x, y) = D_{p,0}(x, y)\ T(x, y)$, with $D_p(x, y)$ the predicted portal dose at

position (x, y) beneath the patient, $D_{p,0}(x, y)$ the predicted portal dose in absence of the patient (as described in section 8.2.2), and $T(x, y)$ the predicted transmission through the patient using the planning CT-data. The method for calculation of these transmission functions has been described elsewhere. A potential problem is to distinguish between deviations in predicted and measured PDIs due to machine faults and differences due to deviations between the patient anatomy during acquisition of the planning CT scan and during treatment. For prostate cancer patients we have observed that deviations in patient anatomy introduce large local differences between predicted and measured PDIs [84]. Machine faults are likely to produce a constant difference over the whole irradiation field. In case of malfunctioning of a single leaf, the difference will be limited to the beam's eye view of that leaf.

Acknowledgments

The authors would like to thank Gert-Jan van de Pol for his help with the measurements. This work was financially supported by the Dutch Cancer Society (Grants DDHK 94-848 and 98-1681).

Chapter 9

Discussion

9.1 Introduction

The main objective of this study was to develop techniques for dosimetric treatment verification using a fluoroscopic electronic portal imaging device (EPID). Therefore we determined the dosimetric characteristics of the EPID (Chapter 2 [61]) and developed a method to derive portal dose images (PDIs) from measured EPID images (Chapter 3 [116]). A separate algorithm was developed for accurate prediction of these PDIs, based on the planning CT data of the patient, the irradiation geometry and the calculated number of monitor units, as determined in the treatment planning process (Chapter 4 [115]). In a pilot study with ten prostate cancer patients, good on-axis agreement agreement between measured and predicted portal doses was found (Chapter 5 [84]). However, off-axis comparisons revealed large deviations for the lateral field, due to variations in rectal filling that resulted in variations in the actual position of the prostate in the treatment beams ('internal organ motion'). Comparison of a measured PDI with a corresponding predicted PDI cannot reveal an error in the monitor unit (MU) calculation of the beam. Therefore we also developed a method to derive the on-axis patient dose at 5 cm depth from the portal dose measured with the EPID. For 115 prostate cancer patients this patient dose was compared with the intended dose, derived from the relative dose distribution calculated by the TPS and the prescribed isocenter dose (Chapter 6 [122]). Finally, we also developed methods for pretreatment verification of intensity modulated beams generated with compensators (Chapter 7 [124]) or dynamic multileaf collimation (DMLC) (Chapter 8 [113]).

9.2 Dosimetric characteristics of EPIDs

Already in 1986, Leong investigated the dosimetric properties of his video based EPID [89]. In 1991, Morton *et al.* reported on the dosimetric characteristics of an EPID based on a linear array of 128 scintillation crystals [106]. In recent years, several other groups have also studied the properties of their EPIDs for dosimetric measurements. Most studies were performed for two commercial systems, the fluoroscopic, CCD camera based Philips SRI-100 [61, 80, 81, 116, 125] and the Varian PortalVision liquid-filled matrix ion chamber system [9, 11, 43, 44, 173, 176].

9.2.1 The liquid-filled EPID

The liquid-filled EPID was developed at the Antoni van Leeuwenhoek Hospital in Amsterdam by van Herk and Meertens [160] and is commercially available as the PortalVision system (Varian Inc., Palo Alto, CA). It consists of a matrix of 256×256 liquid-filled ionization chambers located in a sensitive area of 32×32 cm^2. The matrix with supporting electronics is mounted on a (computerized) retractable arm. The focus-detector distance can be varied between 105 and 180 cm. Successively, rows of 256 chambers are read out by applying a high voltage on the ionization chambers to measure the ionization currents with 256 electrometers. In the normal, non-smoothed sampling mode (standard acquisition mode) the sampling time for one row is 20 ms and the image scan time is 5.6 s [43]. Due to this (relatively long) read out time, this device can only measure dose rate. To derive absolute doses a conversion of the measured dose rate image is necessary, which requires a continuous read out of the monitor chamber signal of the accelerator during image acquisition and the number of MU given during the irradiation fraction [9].

The dosimetric characteristics of this EPID have been investigated by several groups [9, 11, 43, 44, 111, 173, 176]. The main results are: (i) the reproducibility of EPID signals is 1% (1 SD) [44, 176], (ii) the doserate-response of the EPID can be described accurately by an equation with a term proportional to the square root of the doserate and another term linear to the doserate [44] or a power law [9], (iii) images have to be corrected for the side scatter in the EPID (which is lacking in the cylindrical mini phantom used to calibrate the system) using a deconvolution filter [44] and (iv) images have to be corrected for the differences in relative sensitivity of each individual ionization chamber - electrometer combination [44]. Boellaard *et al*. investigated the buildup required to obtain electronic equilibrium in the detector [11]. The standard buildup layer in front of the liquid has a water equivalent thickness of 8 mm. They found that for a 25 MV beam an additional buildup of 28 mm polystyrene was required. This adds a weight of 4.5 kg to the detector. Due to the extra layer the image quality deteriorates. Whether the images can still be used for patient setup verification has not yet been described in the literature.

So far no results have been published for dosimetric application of the liquid filled EPID in intensity modulated beams produced with DMLC. Maximum leaf speeds during DMLC on various treatment machines are between 1 and 3 cm s^{-1} at isocenter. In the fastest acquisition mode the read-out time of the matrix is 1.6 s (at full resolution) [158]. This seams too low to acquire enough snap shots of the beam to accurately reconstruct arbitrary intensity profiles produced with DMLC. Intensity modulated beams can also be produced with the 'step-and-shoot' technique by superpositioning a number of partially overlapping, static, irregularly shaped fields produced with the MLC [16]. The liquid filled EPID may be suited for controlling the delivery of a sequence of these static fields.

9.2.2 The fluoroscopic SRI-100 EPID

The SRI-100 was developed in a collaboration between the former Philips Radiotherapy Systems, the former Laboratory for Space Research in Leiden and the Daniel den Hoed Cancer Center (DDHCC) [164]. This EPID was used in our studies. The SRI-100 basically consists of a fluorescent screen, two mirrors and a CCD camera. The EPID has a fixed focus to fluorescent screen distance of 160 cm. The fluorescent screen is a 1.65 mm thick stainless steel plate

coated with a layer of gadolinium oxysulfide. X-ray photons which hit the detector screen generates visible light in the fluorescent layer, which is viewed by a CCD camera using two 45^o tilted mirrors. A limitation of fluoroscopic systems is the light collecting efficiency of the optical chain. Because the light is highly scattered within the phosphor screen, the light is emitted from the rear of the screen in all directions. Only those light photons that are emitted within a small cone subtended by the lens of the camera can generate a signal on the CCD chip. Much of the effort in the development of fluoroscopic EPIDs has been to improve the light collection in the optical chain, by increasing the light output of the fluorescent screen, a lens that collects more light or camera's with a higher light-quantum efficiency [munro95]. An advantage of CCD camera based systems over scanning systems is the high data acquisition rate and capability to measure simultaneously in all points of the treatment field, which makes it an ideal tool for verification of DMLC [5, 96, 112–114, 116].

We have investigated the dosimetric characteristics of this EPID in a 6 MV and a 25 MV photon beam [61, 116]. To reduce the detection of high energy electrons generated in the patient, we mounted an additional 1 mm thick stainless steel slab on top of the standard fluorescent screen. The added slab hardly affects the image quality [85]. The acquired images may be used both for patient setup verification and for *in vivo* dosimetry [84]. We found that: (i) the day-to-day variation of the EPID response per unit of delivered dose is only 0.4% (1 SD), (ii) the EPID response is non-uniform (related to the 45^o tilted mirror), (iii) the EPID response as function of the transmitted dose measured with an ionization chamber is not linear, due to non-linear electronics and a difference in spectral sensitivity of the EPID and the ionization chamber and (iv) visible photons produced by the x-ray beam in a point of the fluorescent screen do not only generate a signal in the corresponding pixel of the EPID image, but also cause an increased signal at all other pixels due to light scatter from components of the EPID structure onto the CCD chip (optical 'cross talk').

To convert measured EPID images into absolute dose distributions a three steps procedure was developed. Acquired images are first corrected for the non-linear response of the system [116, 125]. Then, the image is corrected for the optical 'cross talk' by deconvolving it with a point spread function [61, 116]. Finally, the resulting array is divided by an array that accounts for variations in local EPID sensitivity [116]. The accuracy of the method was assessed by comparing PDIs measured with the EPID with PDIs measured with a scanning ionization chamber in a mini phantom, located at the same position as the fluorescent screen. For irradiations in open, wedged and intensity modulated 25 MV photon beams (produced with DMLC) EPID and ionization chamber measurements agreed to within 1% (1 SD) [116].

9.2.3 Flat panel imager

Recently, prototypes of a new type of EPID have been developed by Antonuk *et al.* [3]: the active matrix flat-panel imager (AMFPIs). It basically consist of a large area light sensor which is placed in direct contact with a fluorescent screen. The high optical transfer efficiency of these devices compared to that of camera based systems, leads to significantly improved image quality, which is important for patient setup verification. They are also less bulky than the present camera based systems. For transmission dosimetry these systems have the potential advantage over CCD camera based systems that they do not suffer from optical 'cross talk' [108]. Disadvantages of these systems are the high costs, the complex electronics that are required and the sensitivity of the detector and the supporting electronics for radiation damage.

A detailed study of the dosimetric properties of the first prototypes have not yet been reported. A Monte Carlo model of the detector [77] may be useful to understand and to improve the dosimetric properties of these new devices.

9.2.4 Conclusions

With respect to the PortalVision and the SRI-100 the following conclusions can be drawn. (i) Both systems are very stable and allow reproducible, quantitative measurements in static beams. (ii) For both systems methods have been developed for accurate derivation of portal doses from measured images. (iii) The SRI-100 is operated fully independent of the linear accelerator. Dosimetry with the PortalVision system is performed using a read out of the monitor chamber system of the accelerator during image acquisition and the number of monitor units given during the irradiation fraction [9]. (iv) The SRI-100 is an area detector, visualizing the whole radiation field and allowing simultaneous absolute dose measurements in all points of the field, making it suitable for use in intensity modulated beams produced with DMLC. The PortalVision system is a scanning system making it less suitable for dose measurements in these fields.

9.3 Dosimetric applications of EPIDs

Several studies on dosimetric applications of EPIDs have been performed. Kirby *et al.* have evaluated possibilities of the SRI-100 EPID for the routine, off-line check of the field profile of a treatment unit [81]. In our institution, this EPID is in daily use for quality control of the absolute output and field flatness of the 10 MV and 25 MV photon beams of a MM50 Racetrack Microtron [39].

Evans *et al.* have studied the use of their EPID for determination of so-called pseudo-CT slices for breast cancer patients for derivation of tissue compensators to obtain a homogeneous dose distribution in the target [49–51]. Yin [174] and Roback [131] have studied the design of missing tissue compensators, yielding a constant transmission dose distribution as measured with their EPID. Low *et al.* have developed a system for verification of milled compensators, prior to irradiation of the patient, using their EPID. They compared the fluence measured with an EPID with corresponding fluences calculated using the intended filter shape [95]. We have developed a method to determine the 2D *thickness* profile of a compensator, prior to clinical application, with an accuracy of 0.5 mm (1 SD) [123, 124]. An error of 0.5 mm in thickness corresponds to a change in transmitted dose of 1% for a 10 MV beam.

A number of groups has performed studies on anthropomorphic phantoms and/or clinical pilot studies (maximum number of patients: 12) to evaluate the use of EPIDs for dosimetric quality control of treatments (*in vivo* dosimetry) [43, 44, 59–61, 80, 81, 84, 85, 98, 99, 118, 144, 176] Recently, a larger study with 115 patients was completed in our institute (chapter 6).

Several approaches for *in vivo* dosimetry with an EPID have been proposed. Kirby *et al.* have studied a method for estimation of the on-axis patient exit dose from measured SRI-100-signals, using a set of calibration measurements for homogeneous, flat water-equivalent absorbers [80, 81]. Heijmen *et al.* pointed at an inherently limited accuracy of this method, when applied in the thorax region of patients or in case of the use of (strongly) intensity modulated beams [61].

Van Dam and Fiorino have investigated the use of portal films to measure 2-dimensional exit dose profiles [52, 155]. Huyskens *et al.* have described a method to determine midplane

dose distributions from on-axis measured entrance and exit doses, using semiconductors [71], and an exit dose profile derived from portal film. For twelve lung cancer patients, Essers *et al.* have measured exit dose rate profiles with a PortalVision system that was positioned as close as possible to the exit side of the patient (usually at a distance of 12 cm) [44]. They used diodes to convert relative dose rate profiles into absolute dose profiles.

Leong and Wong have proposed to compare predicted portal dose images (PDIs) - i.e. dose distributions behind patients in a plane perpendicular to the beam axis - with PDIs measured during treatment [89, 172]. For a ^{60}Co beam, Wong *et al.* have assessed the accuracy of the Delta Volume method for prediction of PDIs in a plane close behind the patient [172]. In our institution, a method has been developed for accurate prediction of PDIs, using the planning CT-data of the patients [64, 115, 117, 126]. For each beam quality, the calculations are based on a set of input functions - such as attenuation curves for primary radiation, and radial scatter point spread functions describing the scatter from the patient onto the EPID - that have been derived from a limited set of measured beam data.

Hansen *et al.* derived the primary fluence from a measured PDI and back projected that fluence through the patient to yield the primary fluence distribution in the patient. This distribution was then convoluted with dose deposition kernels to derive the dose distribution in the patient [58, 60]. Results were presented for a humanoid phantom and a pelvic patient. McNutt *et al.* developed an iterative convolution/superposition algorithm, based on precalculated Monte Carlo data, to reconstruct dose distributions in patients from exit dose measurements with an EPID and showed results for three phantoms [98]. The method does not allow a fully independent verification of the patient dose description a the convolution/superposition algorithm is both used for designing the treatment plan and verification of the patient dose distribution. We have proposed to use predicted transmissions $T(x, y)$ of the high energy photon beam through the patient to derive the two-dimensional beam fluence profile entering the patient, from the measured EPID image. Transmissions $T(x, y)$ are calculated using the planning CT-data. The derived beam fluence profiles can be used for a forward calculation of the patient dose distribution. All three methods require that the patient geometry during treatment is known, i.e. that the planning CT-scan closely represents the patient anatomy during treatment. In the method of Ying *et al.*, a deviating patient anatomy at the time of treatment is accounted for in an iterative procedure that modifies the planning CT-data [175].

Boellaard *et al.* have developed a convolution model to convert measured PDIs into exit dose distributions [12, 13]. Later the model was extended to derive the midplane dose in the patient, which than can be compared with the dose calculated by the TPS [10]. The model takes into account patient inhomogeneities using the radiological path length to the patient. The radiological path length is derived from the transmission through the patient measured with the EPID (which requires an extra measurement without the patient in the beam). The planning CT data of the patient is not used. It is assumed that inhomogeneities are distributed symmetrically around the midplane, which is not always correct. A clinical pilot study was performed for 5 larynx cancer patients, 2 breast cancer patients, 5 lung cancer patients and 10 prostate cancer patients [14]. Generally, the calculated and backprojected dose agreed within 2.5% (1 SD), for a few of the prostate and long cancer patients larger local differences were found due to differences between the actual patient anatomy and the planning CT-data; e.g. as a result of variable rectum filling and anatomical changes in the lung.

In a pilot study with ten prostate cancer patients we encountered the problem of deviating

patient anatomies due to internal organ motion [84, 85, 118]. Comparison of predicted PDIs with PDIs measured during treatment with the EPID often revealed large differences in transmitted doses in those parts of the PDI that, according to the planning CT-scan, corresponded to raylines that should pass the rectum, the posterior part of the prostate, or the seminal vesicles. The observed differences - that were attributed to variations in rectal filling - pointed at shifts in anterior-posterior direction of the prostate and seminal vesicles.

Comparing a measured PDI with a predicted PDI cannot reveal an error in the MU calculation, since the calculated number of MU is both used for treatment (and thus affects the PDI measurement) and for PDI prediction. Therefore, we developed a method that enables 'in vivo' verification of the MU calculation of the treatment beams by comparing the intended on-axis patient dose at 5 cm depth (D_5), as determined from the relative dose distribution calculated by the TPS and the prescribed isocenter dose (2 Gy), with D_5 as derived from the portal dose D_p measured with the EPID. The method was evaluated clinically for 115 prostate cancer patients. It allowed accurate verification of the MU calculation. Deviations for the lateral beams were 2.4% (1 SD) and for the anterior-posterior (AP) beam 3.4% (1 SD). The standard deviations for the AP beam are larger since variations in radiological thickness have relatively more effect on the transmitted dose and the central rayline in the AP beam passes both the rectum and the bladder, whereas the central rayline in the lateral fields does not pass through organs with variable filling.

Intensity modulated radiotherapy (IMRT), especially with DMLC, is a rapidly evolving field and the first patient has already been treated [93]. DMLC is complex and requires extensive quality assurance. CCD camera based EPIDs are an ideal tool for verification of DMLC due to their high data acquisition rate and capability to measure simultaneously in all points of the treatment field [5, 96, 112, 113, 116]. Balter *et al.* showed preliminary results of a method to derive leaf positions in each camera frame acquired during treatment and to compare them with a table of prescribed leaf positions [5]. Leaf positions could be determined with an accuracy of 0.6 mm and a duty cycle of less than 1 s. A similar approach was implemented by Partridge *et al.* [112]. Ma *et al.* calculated normalized reference images from MLC leaf sequencing files and compared these with normalized images measured with a fluoroscopic beam imaging system (BIS, Wellhöfer Dosimetrie, Schwarzenbruck, Germany) for a 6 MV photon beam [96]. They were able to detect uncertainties of less than 0.5 mm in leaf position during DMLC.

The above described methods to verify leaf motion cannot be used to check whether the calculated leaf trajectories do indeed generate the absolute beam fluence profiles used in treatment planning. Therefore we have developed an accurate method for a pretreatment verification of the intensity modulated beams. For each beam, 2D dose distributions are measured with the EPID and compared with predicted dose distributions [113]. The method verifies: (i) the leaf trajectory calculation (including the models to incorporate collimator scatter and leaf transmission), (ii) the correct transfer of the leaf sequencing file to the treatment machine and (iii) the mechanical and dosimetrical performance of the treatment unit. Predictions and EPID measurements for 10 and 25 MV photon beams agreed within 2% (1 SD).

9.4 Future investigations

Treatment verification with an EPID (*in vivo*) is still in its infancy. Only one large clinical study (N=115) and a few pilot studies have been performed with very small numbers of patients (2-

12) and methods are still under development. New tumor sites need to be included in the investigations and the developed methods must be tested, optimized and evaluated in large clinical studies. For all sites guide lines for clinical application have to be established including action levels.

Comparison of predicted PDIs with PDIs measured with an EPID can reveal internal organ motion, i.e. the patient anatomy at the time of treatment differs from the anatomy as recorded in the planning CT-scan [84]. To use of EPIDs for detection of internal motion needs to be further investigated. Currently a study is performed based on multiple CT data [146]. For each patient, changes in the anatomy as indicated by the planning CT-scans will be correlated with changes in the calculated, i.e. simulated, PDIs that would have been measured with the EPID during treatment.

Obviously, *in vivo* dosimetry with an EPID could also greatly contribute to the daily, quality control of dynamic treatments. As described in this thesis methods have been developed for fast and accurate pretreatment verification of beams produced with DMLC (Chapter 8 [113]) using an EPID. The developed method will be extended to enable verification of DMLC during patient treatment. Acquisition of portal images suitable for dosimetric verification of DMLC can be fully integrated into existing imaging routines for patient setup verification, without introducing an increase in the overall treatment time [84].

9.5 Conclusions

This thesis describes the development and clinical implementation of models to use a fluoroscopic, CCD camera based EPID for *in vivo* dosimetry. It has been shown that the developed procedures for measurement and prediction of PDIs allow accurate dosimetric quality control of the treatment of prostate cancer patients and that comparison of measured PDIs with predicted PDIs can reveal internal organ motion. Furthermore, an accurate method for verification of the MU calculation of an x-ray beam using EPID measurements has been developed. The method allows to discriminate on errors that are due to changes in patient anatomy and errors due to a deviating cGy/MU-value. With a CCD camera based EPID dosimetric information is simultaneously obtained over the whole beam area and not only in a single or a few points. Therefore, portal dosimetry with this EPID is a valuable tool for verification of DMLC. Due to the necessarily small number of detectors, full verification of treatments delivered with DMLC is not possible with conventional *in vivo* dosimetry using diodes or Thermoluminescence Dosimetry (TLD). It can be concluded that *in vivo* dosimetry with a fluoroscopic EPID is efficient tool for two-dimensional *in vivo* dosimetry.

Summary

Radiotherapy is with surgery and chemotherapy one of the three main modalities for treating patients with cancer. The aim of curative radiation therapy is to deliver as high dose to diseased tissue as needed or as possible without causing unacceptable side effects to the patient. The treatment usually consists of irradiation of the patient from different directions with a high energy photon or electron beam. Beam directions are chosen such that the radiation damage to critical organs and healthy tissues is minimized. In conformal radiotherapy the beam shapes and, increasingly also beam intensity patterns, are optimized to further improve conformity of the high dose volume to the tumor volume.

All (complex) procedures involved in the planning and execution of (conformal) radiotherapy treatments do contribute to the overall uncertainty in the delivered dose distributions. As dose response curves for tumors and normal tissues may be steep, verification of dose delivery is mandatory. Treatment verification while the patient is being irradiated can be split into geometrical and dosimetrical verification. Portal imaging with film or with an electronic portal imaging device (EPID) is applied to evaluate the patient setup during treatment and thermoluminescence dosimetry (TLD) or diodes are used to measure the dose at the entrance and/or at the exit side of the patient. A drawback of this approach is that dosimetric information is only obtained in a single or a few points. Moreover, the use of different equipment for geometrical and dosimetrical verification results in extra costs, extra maintenance work and increased treatment times. The aim of this study was therefore to develop techniques for integrated geometrical and dosimetric treatment verification using an EPID.

In chapter 2 the dosimetric characteristics of the in this study applied fluoroscopic EPID (SRI-100, Philips Medical Systems, Crawley, UK) are described. This EPID basically consists of a fluorescent screen, mirrors and a CCD camera. Image acquisition for portal dose measurement was performed with a special procedure, written in the command language that comes with the system. For a 6 MV beam, the observed day-to-day variation in local EPID responses, i.e. measured pixel value (EPID signal) per unit of delivered portal dose, is 0.4% (1 SD); day-to-day variations in *relative* EPID responses (e.g. normalized to the on-axis response) are within 0.2% (1 SD). Measured pixel values are linearly proportional to transmitted portal doses with a proportionality constant which is independent of the thickness of a flat, waterequivalent absorber in the beam, but which does significantly depend on the size of the applied x-ray beam. It was shown that the observed increase in EPID response with increasing field size is mainly due to contributions to the EPID signals from scattered light: Visible photons produced by the x-ray beam in a point of the fluorescent screen do not only generate a signal in the corresponding point of the EPID image, but do also lead (due to scatter from components of the EPID structure onto the CCD chip) to an increased pixel value in all

other points of the image. A point spread function, derived from measured data and describing the increase in EPID response at the beam axis due to off-axis irradiation of the fluorescent screen, was successfully applied to connect portal doses with pixel values measured with the EPID.

In chapter 3 a method is presented to accurately measure portal dose images (PDIs) with the SRI-100 EPID. The method accounts for (i) the optical 'cross talk' within the EPID structure (see chapter 2), (ii) the spatially non-uniform EPID response and (iii) the observed non-linearity of the EPID response (mainly due to non linear electronics). It is based on a deconvolution algorithm. Measurement of the required input data is straightforward. The accuracy of the method was assessed by comparing PDIs measured with the EPID with PDIs measured with a scanning ionization chamber in a mini phantom, located at the same position as the fluorescent screen. For irradiations in open, wedged and intensity modulated 25 MV photon beams (produced with dynamic multileaf collimation) EPID and ionization chamber measurements agreed to within 1% (1 SD).

A method for prediction of these PDIs in open (non wedged) beams is described in chapter 4. The following equation for calculation of PDIs is used $D_p(x, y) = T(x, y) \cdot D_{p,0}(x, y)$, with $D_p(x, y)$ the portal dose in point (x, y) of the PDI, $T(x, y)$ a function describing the transmission of the high energy photon beam through the patient and $D_{p,0}(x, y)$ the portal dose that would have occurred in (x, y) in the absence of the patient. For the calculation of the dose distributions $D_{p,0}(x, y)$ in the detector plane of the EPID, we have slightly modified an algorithm that was developed in our institute for dose calculations in water phantoms. The transmission calculations are based on the planning CT-scan of the patient and on the irradiation geometry as determined in the treatment planning process. For each beam quality, the required input data for this algorithm are derived from a limited number of measured beam data. The method was tested for a PDI-plane at 160 cm from the focus, in agreement with the fixed focus-to-detector distance of our fluoroscopic EPIDs. For 6, 23 and 25 MV photon beams good agreement ($\sim$1%) was found between calculated and measured transmissions $T(x, y)$ through anthropomorphic phantoms.

Results of a first clinical evaluation of developed methods for dosimetrical treatment verification are presented in chapter 5. For ten prostate cancer patients, the inter-fraction variation within measured PDIs was assessed and measured PDIs were compared with corresponding predicted PDIs, based on the planning CT scan of the patient. For the lateral fields, the average standard deviation in the measured *on-axis* portal doses during the course of a treatment was 0.9%; for the anterior-posterior (AP) fields this standard deviation was 2.2%. The difference between the average on-axis measured portal dose and the predicted portal dose was 0.3 $\pm$ 2.1% (1 SD) for the lateral fields and 0.7 $\pm$ 3.4% (1 SD) for the AP fields. *Off-axis* differences between measured and predicted portal doses for the lateral fields were regularly much larger (up to 15%) and were caused by frequently occurring gas pockets inside the rectum of the patients during treatment or during acquisition of the planning CT scan. The detected gas pockets did sometimes extend into the gross tumor volume (GTV) area as outlined in the planning CT scans, implying a shift of the anterior rectum wall and prostate in anterior direction (internal organ motion). This clinical study has shown that the developed procedures for measurement and prediction of PDIs allow accurate dosimetric quality control of the treatment of prostate cancer patients and that comparing measured PDIs with predicted PDIs can reveal internal organ motion.

However, comparisons of PDIs can not reveal errors in the MU calculation of a beam, since

the calculated number of MU is both used for treatment (and thus affects the PDI measurement) and for PDI prediction. In chapter 6 a method is presented that enables *in vivo* verification of the MU calculation of the treatment beams. The method is based on comparison of the intended on-axis patient dose at 5 cm depth, D_5, with D_5 as derived from the portal dose D_p measured with an EPID. The developed method was evaluated clinically for a group of 115 prostate cancer patients. The on-axis patient dose D_5 was derived from the measured portal dose using (i) the predicted beam transmission calculated with the planning CT data of the patient (see chapter 4) and (ii) an empirical relation between portal doses D_p and patient doses D_5. Derived patient doses D_5 were compared with intended doses D_5 which were determined from the relative dose distribution calculated by the treatment planning system and the prescribed isocenter dose (2 Gy). For interpretation of observed differences, the corresponding on-axis measured portal doses D_p were also compared with predicted portal doses. For the three open beams, in total 7828 images were analyzed. The mean difference between the predicted patient dose and the patient dose derived from the average measured portal dose was: $0.4 \pm 3.4\%$ (1 SD) for the AP beam and $-1.5 \pm 2.4\%$ (1 SD) for the lateral beams. For 7 patients the difference between the predicted portal dose and the average measured portal dose for the AP beam and the corresponding difference in patient dose D_5 were both greater than 5%. All these patients had relatively large gas pockets (3-3.5 cm in AP direction) in the rectum during acquisition of the planning CT, which were not present during (most) treatments. The developed methods allow to discriminate on errors that are due to changes in patient anatomy and errors due to a deviating cGy/MU-value.

Dose distributions can often be significantly improved by modulating the two-dimensional intensity profile of the individual x-ray beams. At the Daniel den Hoed Cancer Center two techniques are used for generating these intensity modulated beams; compensators and dynamic multileaf collimation (DMLC). The EPID is suitable for fast and accurate pretreatment verification of intensity modulated beams generated with these techniques as shown in the next two chapters.

In chapter 7 a method is presented for verification of compensator thicknesses. The method is based on the measured transmission $T(x, y)$ through the compensator, defined by the ratio of the portal dose with the compensator in the beam and the portal dose without the compensator in the beam. The compensator transmission is determined with the EPID by dividing two images, acquired with and without compensator inserted, which are only corrected for the non-linear response of the SRI-100 system (see chapter 3). The transmission has a primary and a scatter component. The primary component is derived from the measured transmission by subtracting the predicted scatter component. The primary component for each point is only related to the thickness of the compensator along the ray line between the focus and that point. Compensator thicknesses are derived from the primary components taking into account off-axis variations in beam quality. The developed method was tested for various compensators made of a granulate of stainless steel. The compensator thicknesses could be determined with an accuracy of 0.5 mm (1 SD), corresponding to a change in the transmitted dose of about 1% for a 10 MV beam. The method is fast, accurate and insensitive to long-term output and beam profile fluctuations of the linac.

In chapter 8 a method is presented for a pretreatment dosimetric verification of intensity modulated beams generated with DMLC. In the absence of the patient EPID images are acquired for all beams produced with DMLC. These images are then converted into 2D dose distributions and compared with predicted dose distributions. The predictions are performed

with the same pencil beam algorithm as implemented in our commercially available treatment planning system, using the same absolute beam fluence profiles as used for calculation of the patient dose distribution. The method verifies: (i) the leaf trajectory calculation (including the models to incorporate collimator scatter and leaf transmission), (ii) the correct transfer of the leaf sequencing file to the treatment machine and (iii) the mechanical and dosimetrical performance of the treatment unit. The method was tested for intensity modulated 10 and 25 MV photon beams; both model cases and real clinical cases were studied. Dose profiles measured with the EPID were also compared with ionization chamber measurements. In all cases both predictions and EPID measurements and EPID and ionization chamber measurements agreed within 2% (1 SD). The study has demonstrated that the proposed method allows fast and accurate pretreatment verification of DMLC.

In the final chapter the developed methods for dosimetric treatment verification with an EPID are evaluated and compared with other methods. Furthermore, the dosimetric characteristics of the fluoroscopic EPID are compared with those of an EPID system consisting of a matrix of liquid filled ionization chambers. The overall result of this study is that the developed techniques allow accurate dosimetric quality control of the treatment of prostate cancer patients and that comparison of measured PDIs with predicted PDIs can reveal internal organ motion.

Samenvatting

Radiotherapie is met chirurgie en chemotherapie een van de drie belangrijkste modaliteiten voor het behandelen van patiënten met kanker. Het doel van curatieve radiotherapie is het afgeven van een zo hoog mogelijke dosis als nodig of mogelijk aan aangetast weefsel zonder onacceptabele neveneffecten te veroorzaken bij de patiënt. De behandeling bestaat gewoonlijk uit bestraling van de patiënt uit verschillende richtingen met een hoog energetische fotonen of electronen bundel. De bundelrichtingen worden zo gekozen dat de stralingsschade aan gezond weefsel wordt geminimaliseerd. In conformatie radiotherapie worden de bundel vorm en, in toenemende mate ook het bundel intensiteitsprofiel, geoptimaliseerd om het hoge dosis volume verder te conformeren rond het tumor volume.

Alle (complexe) procedures die gebruikt worden tijdens de planning en uitvoering van een (conformatie) radiotherapie behandeling dragen bij aan de totale onzekerheid in de afgegeven dosisverdeling. Omdat dosis respons curven voor zowel tumor als gezond weefsel steil kunnen zijn is verificatie van de dosisverdeling noodzakelijk. Verificatie van behandelingen terwijl de patiënt wordt bestraald kan worden gesplitst in geometrische en dosimetrische verificatie. Megavolt afbeeldingen van de patiënt in de bundel kunnen worden gemaakt met film of een electronisch Megavolt Afbeelding (MVA) systeem en worden gebruikt om de positionering van de patiënt in de bundel te verifiëren. Thermoluminescentie dosimetrie chips (TLDs) of diodes kunnen worden gebruikt om de dosis aan het in- of uittree vlak van de patiënt te meten. Een nadeel van deze benadering is dat dosimetrische informatie alleen wordt verkregen in een enkel of een paar punten. Ook leidt het gebruik van verschillende apparatuur voor positie en dosimetrische verificatie tot hogere kosten, extra onderhoudswerk en extra behandeltijd. Het doel van de in dit proefschrift beschreven studie was het ontwikkelen van technieken voor geïntegreerde geometrische en dosimetrische verificatie met behulp van een MVA systeem.

In hoofdstuk 2 worden de dosimetrische eigenschappen van het in deze studie gebruikte fluorescopisch MVA systeem (Philips SRI-100, Philips Medical Systems, Crawley, UK) beschreven. Dit systeem bestaat uit een fluorescerend scherm, twee 45^{o} spiegels en een CCD camera. Het opnemen van beelden voor transmissiedosis metingen werd gedaan met een speciale procedure, geschreven in de macro taal die bij het systeem geleverd wordt. Opgenomen beelden kunnen zowel voor geometrische als voor dosimetrische verificatie worden gebruikt. Voor een 6 MV fotonen bundel is de dag-tot-dag variatie in lokale MVA respons, m.a.w. de gemeten pixel waarde (MVA signaal) per eenheid van afgeleverde dosis, 0.4% (1 SD); de dag-tot-dag variatie in *relatieve* MVA respons (genormeerd op de respons op de bundelas) is kleiner dan 0.2%. Gemeten pixel waardes hangen lineair af van de transmissiedosis met een constante die onafhankelijk is van de dikte van een vlak waterequivalent fantoom in de bundel, maar die significant afhangt van de grootte van de gehanteerde fotonenbundel. Het is aangetoond dat de geobserveerde toename in MVA respons met toenemende veldgrootte voornamelijk komt door

bijdragen aan het MVA signaal van gereflecteerd licht: licht fotonen geproduceerd door de megavolt fotonen in een punt van het fluorescentie scherm genereren niet alleen een signaal in het overeenkomstige punt van het MVA beeld, maar ook (door licht reflecties van componenten van de MVA systeem op de CCD chip) tot een toename van de pixel waarde in alle andere punten van het MVA beeld. Een punt spreid functie, afgeleid uit gemeten data die de MVA respons toename op de bundelas beschrijft door een bestraling van het fluorescentie scherm elders, is met succes gebruikt om de relatie te beschrijven tussen transmissiedosis en pixel waardes gemeten met het MVA systeem.

In hoofdstuk 3 wordt een methode gepresenteerd om nauwkeurig transmissiedosis-verdelingen met het SRI-100 MVA systeem te meten. De methode verrekent de (i) optische 'overspraak' binnen de EPID structuur (zie hoofdstuk 2), (ii) de ruimtelijke niet uniforme MVA gevoeligheid en (iii) de gevonden niet lineaire MVA respons (voornamelijk door niet lineaire electronica). De methode is gebaseerd op een deconvolutie algoritme. Er is een beperkte gemeten dataset nodig. De nauwkeurigheid van de methode is bepaald door het vergelijken van transmissiedosisverdelingen gemeten met het MVA systeem met dosisverdelingen gemeten met een scannende ionisatie kamer in een mini meetfantoom in hetzelfde vlak als het fluorescerend scherm. Voor bestralingen in open, wig en intensiteits gemoduleerde 25 MV bundels (geproduceerd met dynamische multileaf collimatie) komen MVA en ionisatie kamer metingen overeen binnen 1% (1 SD).

Een methode voor voorspelling van deze transmissiedosisverdelingen in open (zonder wig) velden wordt beschreven in hoofdstuk 4. De formule die wordt gebruikt voor het berekenen van de transmissiedosisverdeling is $D_p(x, y) = T(x, y)D_{p,0}(x, y)$, met $D_p(x, y)$ de transmissiedosis in punt (x, y) van het detectorvlak, $T(x, y)$ de transmissie van de bundel door de patiënt en $D_{p,0}(x, y)$ de transmissiedosis die zou zijn opgetreden in (x, y) zonder patiënt in de bundel. Voor de berekening van $D_{p,0}(x, y)$ in het detectorvlak van het MVA systeem, hebben we een algoritme aangepast dat in ons instituut is ontwikkeld voor berekeningen in waterfantomen. De berekening van de transmissie is gebaseerd op de planning CT scan van de patiënt en de bestralingsgeometrie zoals bepaald tijdens de planning. Voor iedere bundelenergie wordt de vereiste invoerdata voor dit algoritme afgeleid uit een beperkte set meetdata. De methode is getest voor een transmissiedosis vlak op 160 cm van het focus, in overeenstemming met de vaste focus detector afstand van onze fluorescopische MVA systemen. Voor 6, 23 en 25 MV fotonen bundels is er goede overeenstemming (binnen 1%) gevonden tussen gemeten en berekende transmissies.

Resultaten van een eerste klinische evaluatie van de ontwikkelde methodes voor dosimetrische behandel verificatie worden gepresenteerd in hoofdstuk 5. Voor tien prostaatkanker patiënten is de variatie in gemeten transmissiedosisverdelingen tussen behandel fracties vastgesteld en zijn gemeten transmissiedosisverdelingen vergeleken met transmissiedosisverdelingen berekend met behulp van de planning CT van de patiënt. Voor de laterale velden was de gemiddelde standaard deviatie (SD) 0.9%, voor de anterior-posterior (AP) bundel was deze standaard deviatie 2.2%. De verschillen tussen de gemiddelde op de bundelas gemeten transmissie dosis en de voorspelde transmissiedosis was $0.3 \pm 2.1\%$ (1 SD) voor de laterale velden en $0.7 \pm 3.4\%$ (1 SD) voor de anterior posterior velden. Naast de bundelas zijn verschillen tussen gemeten en voorspelde transmissiedosis voor de laterale velden veel groter (tot 15%). Deze verschillen werden veroorzaakt door regelmatig optredende gasbellen in de endeldarm van de patiënt. De gedetecteerde gasbellen liepen soms door tot in het in de planning CT scan ingetekende tumorvolume (gross target volume;

GTV), hetgeen een verschuiving van de anterior wand van de endeldarm en de prostaat in anterior richting impliceert (interne orgaan beweging). Deze studie heeft aangetoond dat de ontwikkelde procedure voor het meten en voorspellen van transmissiedosisverdelingen geschikt is voor nauwkeurige dosimetrische kwaliteitsbewaking van de behandeling van prostaatkanker patiënten en dat met het vergelijken van gemeten en voorspelde transmissiedosisverdelingen interne orgaanbeweging kan worden aangetoond.

Het vergelijken van transmissiedosisverdelingen kan echter geen fouten in de Monitor Eenheden (ME) berekening van een bundel aantonen, omdat het berekende aantal ME zowel voor de behandeling (en dus de meting) als voor de voorspelling wordt gebruikt. In hoofdstuk 6 wordt een methode gepresenteerd die *in vivo* verificatie van de ME berekening van de verschillende bundels mogelijk maakt. De methode is gebaseerd op het vergelijken van de geplande dosis in de patiënt op de bundelas op 5 cm diepte, D_5, met D_5 afgeleid van de transmissiedosis D_p gemeten met een MVA systeem. De ontwikkelde methode is klinisch getest voor 115 prostaatkanker patiënten. De patiëntdosis op de bundelas D_5 wordt afgeleid van de gemeten transmissiedosis gebruik makend van (i) de bundel transmissie berekend aan de hand van de planning CT data van de patiënt (zie hoofdstuk 4) en (ii) een empirische relatie tussen transmissiedosis D_p en patiëntdosis D_5. De afgeleide patiëntdosis D_5 is vergeleken met de geplande dosis D_5 welke bepaald werd aan de hand van de relatieve dosisverdeling berekend door het planning systeem en de voorgeschreven isocentrum dosis van 2 Gray (Gy). Voor interpretatie van de geobserveerde verschillen is de gemeten transmissiedosis op de bundelas ook vergeleken met de voorspelde transmissiedosis. Voor de drie open bundels zijn in totaal 7828 beelden geanalyseerd. Het gemiddelde verschil tussen de voorspelde patiënt dosis en de patiëntdosis afgeleid uit de gemiddelde gemeten transmissiedosis was 0.4±3.4% (1 SD) voor de AP bundel en -1.5±2.4% (1 SD) voor de laterale bundels. Voor 7 patiënten was het verschil tussen de voorspelde en de gemiddelde gemeten transmissiedosis voor de AP bundel en het corresponderende verschil in patiëntdosis D_5 groter dan 5%. Al deze patiënten hadden relatief grote gasbellen in de endeldarm tijdens het maken van de planning CT, hetgeen tijdens de meeste behandelingen niet het geval was. De ontwikkelde methode maakt onderscheid mogelijk tussen fouten door veranderingen in de patiënt anatomie en verschillen door een afwijkende cGy/ME waarde.

Dosisverdelingen kunnen vaak aanzienlijk verbeterd worden door het moduleren van het twee-dimensionale intensiteitprofiel van de individuele fotonenbundels. In de Daniel den Hoed Kliniek worden twee technieken gebruikt voor het genereren van deze intensiteits gemoduleerde bundels; compensatoren en dynamische multileaf collimatie (DMLC). Het MVA systeem is geschikt voor snelle en nauwkeurige verificatie van bundels gegenereerd met deze technieken zoals aangetoond wordt in de volgende twee hoofdstukken.

In hoofdstuk 7 wordt een methode gepresenteerd voor verificatie van compensator diktes. De methode is gebaseerd op de gemeten transmissie $T(x, y)$ door de compensator, gedefinieerd als de ratio van de transmissie dosisverdeling met de compensator in de bundel en de dosisverdeling zonder compensator in de bundel. De compensator transmissie wordt bepaald met het MVA systeem door het delen van twee beelden, opgenomen met en zonder compensator in de bundel, die uitsluitend gecorrigeerd worden voor de niet lineaire respons van de SRI-100 (zie hoofdstuk 3). De transmissie heeft een primaire en een scatter component. De primaire component wordt afgeleid van de gemeten transmissie door het aftrekken van een voorspelde scatter component. De primaire component voor elk punt is alleen afhankelijk van de dikte van de compensator langs de rayline van het focus naar dat punt. Compensator dikte

wordt afgeleid van de primaire component waarbij rekening wordt gehouden met het verloop in bundel hardheid als functie van de afstand tot de bundelas. De ontwikkelde methode is getest voor verschillende compensatoren gemaakt van roestvrijstalen korrels. De compensator diktes konden worden afgeleid met een nauwkeurigheid van 0.5 mm (1 SD), hetgeen voor een 10 MV bundel overeenkomt met verandering in transmissie dosis van 1%. De methode is snel, nauwkeurig en ongevoelig voor lange termijn output en bundel fluctuaties van de versneller.

In hoofdstuk 8 wordt een methode gepresenteerd voor dosimetrische verificatie van intensiteits gemoduleerde bundels gegenereerd met DMLC. Zonder de patiënt in de bundel worden MVA beelden opgenomen voor alle bundels gegenereerd met DMLC. Deze beelden worden dan geconverteerd naar twee-dimensionale dosisverdelingen en vergeleken met voorspelde dosisverdelingen. De voorspellingen worden gedaan met hetzelfde algoritme als geïmplementeerd in een commercieel verkrijgbaar planningssysteem, gebruik makend van de absolute bundelprofielen die ook gebruikt worden voor berekening van de patiëntdosisverdeling. De methode verifieert: (i) de berekening van de leaf beweging (inclusief de modellen voor het verrekenen van collimator scatter en leaf transmissie), (ii) de correcte overdracht van de leaf beweging file naar de behandel machine en (iii) de correcte mechanische en dosimetrische werking van het toestel. De methode is getest voor intensiteits gemoduleerde 10 en 25 MV fotonen bundel; zowel test gevallen als klinische bundels zijn gebruikt. Dosisprofielen gemeten met het MVA systeem zijn vergeleken met ionisatiekamer metingen. In alle gevallen klopten zowel voorspellingen en MVA metingen als MVA metingen en vat metingen binnen 2% (1 SD). Deze studie heeft aangetoond dat de voorgestelde methodes snelle en nauwkeurige verificatie van DMLC voor de patiënt behandeling mogelijk maken.

In het laatste hoofdstuk worden de ontwikkelde methodes voor dosimetrische behandel verificatie met een MVA systeem geëvalueerd en vergeleken met andere methodes. Verder worden de dosimetrische karakteristieken van het fluorescopische MVA systeem vergeleken met die van een MVA systeem bestaand uit een matrix van vloeistof gevulde ionisatiekamers. Het uiteindelijke resultaat van deze studie is dat met de ontwikkelde technieken nauwkeurige dosimetrische verificatie van bestralingen van prostaatkankerpatiënten mogelijk is en dat met het vergelijken van gemeten en berekende transmissiedosisverdelingen interne orgaanbeweging kan worden aangetoond.

Dankwoord

Het is zover! Na een periode van vijf jaar voltooi ik met het schrijven van dit dankwoord mijn proefschrift. In de afgelopen jaren hebben veel mensen een bijdrage geleverd aan het tot stand komen van dit boek. Graag wil ik op deze plaats een aantal van hen bedanken voor hun bijdrage, of omdat ze op een andere manier deze periode zeer de moeite waard hebben gemaakt.

Ten eerste wil ik Ben Heijmen bedanken voor de enthousiaste steun en begeleiding van dit project. Met name de eerste jaren heb je er veel tijd ingestopt en dat heeft geresulteerd, nadat we wat lastige technische problemen hadden overwonnen, in een goed draaiend project. Het feit dat de Nederlandse Kankerbestrijding het vervolg project heeft goedgekeurd, geeft aan dat we op de goede weg zijn.

Marco Kroonwijk, jou programeervaardigheid heeft veel (klinische)data opgeleverd die de basis vormen voor dit proefschrift. Meer dan honderd shell scripts, IDL en Fortran routines heb je geschreven om alle metingen en berekeningen om te toveren in overzichtelijke figuren en tabellen. Eén van die figuren heeft zelfs de cover van *Int. J. Radiat. Oncol. Biol. Phys.* gehaald. Ook heb je de koppeling tussen het planningssyteem, de CT data en onze software tot stand gebracht. Verder heb je vier jaar lang aan iedere meetavond deelgenomen, soms tot diep in de nacht. Dit alles heeft tot een mooie reeks publicaties geleid, die in dit proefschrift zijn samengebracht. Hoofdstuk 5 is door jou geschreven.

Peter Levendag, bedankt voor het in goede banen leiden van de promotie. De correspondentie met de EUR vult inmiddels een aardige ordner, maar de commissie is dan ook precies zo samengesteld als de bedoeling was.

Ook wil ik enkele (ex-)kamergenoten, (ex-)collega's en stagiaires bedanken voor hun bijdrage aan dit boek en de gezelligheid tijdens de afgelopen vijf jaar. Hans de Boer, Maarten Dirkx, Joep Stroom, Erik van Dieren en Sandra Quint, uit het feit dat jullie co-auteur zijn van de artikelen die ten grondslag liggen aan dit proefschrift blijkt jullie bijdrage. Andries Visser bedankt voor de verbeteringen in de manuscripten. Ook dank aan de MM50 laboranten die ruim 7800 EPID beelden hebben opgenomen die zijn gebruikt voor de hoofdstukken 5 en 6. De klinisch fysisch medewerkers Leo van Battum, Norman Driver, Dirk Binnekamp en Erik Loeff, met name voor het helpen met de nukken van de RFA-300. De stagiaires en afstudeerders die stukjes van de puzzel hebben aangedragen: Sander van der Straaten, Onno van Beusekom, Jeroen Udo, Dennis de Held, Martin Opdam, Gert-Jan van de Pol en Roeland Aeijelts Averink.

Onontbeerlijk, maar meer op de achtergrond waren de bijgedragen van enkele mensen die ik ook wil bedanken. Hans Vuik van het Audiovisueel Centrum voor de dia's ten behoeve van congressen, het digitaliseren van de foto op pagina 3 en de hulp bij het printen van de kleurenfiguren. Philip Verlinde de CadPlan goeroe. I also want to express my gratitude to Pekka Aalto from Varian/Dosetek for his support. Bert van der Leije en Bart Kanis voor het in

de lucht houden van het netwerk, IVO en de PC's.

Hoewel niet verbonden met de Daniel hebben andere mensen op hun eigen manier een bijdrage geleverd. Ten eerste mijn paranimfen: Sander van Vliet en Marc Weeber. Dr Van, ik waardeer het zeer dat je voor mijn promotie een week uit Boston overkomt. Marc, bijna doctor en ook nog eens zweefvlieger, bedankt voor de vele LaTeX tips en E-mails. Floor, met plezier denk ik terug aan de fijne jaren die we samen gedeeld hebben. Bedankt voor de steun en het nalezen van verschillende onderdelen. Leven is meer dan werken alleen, daarom ook dank aan mijn zweefvliegcollega's. Met een kleine groep een paar honderd kilometer overlandvliegen, soms op euforische hoogtes dan weer knokkend met de elementen, om vervolgens (op de goede dagen) met 250 km/u op boomtop hoogte weer terug te komen op Malden; een betere ontspanning kan ik me niet voorstellen.

Tot slot het thuisfront: Tjip en Stefan, bij deze voeg ik een millimeter of 8 toe aan de "familie-boekenkast".

Curriculum vitae

De auteur van dit proefschrift werd geboren op 5 oktober 1968 te Nijmegen. Daar behaalde hij in 1988 het diploma Atheneum β aan het Dukenburg College. In datzelfde jaar begon hij zijn studie Natuurkunde aan de Katholieke Universiteit Nijmegen. Het afstudeeronderzoek vond plaats bij de afdeling Medische en Biofysica. In 1994 studeerde hij af in de informatische fysica en trad in dienst als onderzoeker in opleiding bij de Erasmus Universiteit Rotterdam. Hij werd gedetacheerd bij de afdeling Klinische Fysica van de Daniel den Hoed Kliniek. Daar heeft hij onderzoek verricht naar toepassingen van een megavolt afbeeldingssysteem voor in vivo dosimetrie en dosimetrische verificatie van intensiteits gemoduleerde bundels in het kader van een door de Nederlandse Kankerbestrijding (NKB) gefinancierd project. De resultaten van dit onderzoek zijn beschreven in dit proefschrift. Sinds augustus 1998 is hij als postdoc werkzaam op dezelfde afdeling op een door het NKB gefinancierd vervolgproject. Tevens is hij in opleiding voor klinische fysicus radiotherapie. Naast zijn werk is de auteur een actief zweefvlieger, hij heeft 360 vlieguren en een veertigtal overlandvluchten gemaakt.

List of publications

B J M Heijmen, K L Pasma, M Kroonwijk, V G M Althof, J C J de Boer, A G Visser, and H Huizenga. Portal dose measurement in radiotherapy using an electronic portal imaging device (EPID). *Phys. Med. Biol.*, 40:1943-1955, 1995.

K L Pasma, B J M Heijmen, M Kroonwijk, and A G Visser. Portal dose image (PDI) prediction for dosimetric treatment verification in radiotherapy I: An algorithm for open beams. *Med. Phys.*, 25:830-840, 1998.

K L Pasma, M Kroonwijk, J C J de Boer, A G Visser, and B J M Heijmen. Accurate portal dose measurement with a fluoroscopic electronic portal imaging device (EPID) for open and wedged beams and for dynamic multileaf collimation. *Phys. Med. Biol.*, 43:2047-2060, 1998.

M Kroonwijk, K L Pasma, S Quint, P C M Koper, A G Visser, and B J M Heijmen. In vivo dosimetry for prostate cancer patients using an electronic portal imaging device (EPID); detection of internal organ motion. *Radiother. Oncol.*, 49:125-132, 1998.

K L Pasma, M Kroonwijk, S Quint, A G Visser, and B J M Heijmen. Transit dosimetry with an electronic portal imaging device (EPID) for 115 prostate cancer patients. *Int. J. Radiat. Oncol. Biol. Phys.*, 1999. submitted.

K L Pasma, M Kroonwijk, E B van Dieren, A G Visser, and B J M Heijmen. Verification of compensator thicknesses using a fluoroscopic electronic portal imaging device. *Med. Phys.*, 1999. in press.

K L Pasma, M L P Dirkx, M Kroonwijk, A G Visser, and B J M Heijmen. Dosimetric verification of intensity modulated beams produced with dynamic multileaf collimation using an electronic portal imaging device. *Med. Phys.*, 1999. submitted.

J C J de Boer, B J M Heijmen, K L Pasma, and A G Visser. Characterization of a high elbow, fluoroscopic electronic portal imaging device for portal dosimetry. *Phys. Med. Biol.*, 1999. submitted.

J C Stroom, M Kroonwijk, K L Pasma, E B van Dieren, P C M Koper, and B J M Heijmen. Detection of internal organ movement in prostate cancer patients using portal images. *Med. Phys.*, 1999. submitted.

References

[1] A Adeyemi and J Lord. An audit of radiotherapy patient doses measured with *in vivo* semiconductor detectors. *The British Journal of Radiology*, 70:399–408, 1997.

[2] V G M Althof, J C J de Boer, H Huizenga, J C Stroom, A G Visser, and B N Swanenburg. Physical characteristics of a commercial electronic portal imaging device. *Med. Phys.*, 23:1845–1855, 1996.

[3] L E Antonuk, Y El-Mohri, W Huang, K W Jee, J H Siewerdsen, W Huang, M Maolinbay, V E Scarpine, H Sandler, and J Yorkston. Initial performance evaluation of an indirect-detection, active matrix flat-panel imager (amfpi) prototype for megavoltage imaging. *Int. J. Radiat. Oncol. Biol. Phys.*, 42:437–452, 1998.

[4] J M Balter, K L Lam, H M Sandler, J F Littles, R L Bree, and R K Ten Haken. Automated localization of the prostate at the time of treatment using implanted radiopaque markers: Technical feasibility. *Int. J. Radiat. Oncol. Biol. Phys.*, 33:1281–1286, 1995.

[5] J M Balter, D L McShan, J Kim, and B A Fraass. Automated on-line verification of dynamic multileaf collimator configuration using a megavoltage imager and a computer controlled radiotherapy system. *Med. Phys.*, 24:1002, 1997.

[6] J M Balter, H M Sandler, K Lam, R L Bree, A S Lichter, and R K Ten Haken. Measurement of prostate movement over the course of routine radiotherapy using implanted markers. *Int. J. Radiat. Oncol. Biol. Phys.*, 31:113–118, 1995.

[7] C J Beard, P Kijewski, M Bussière, R Gelman, D Gladstone, K Shaffer, M Plunkett, P Costello, and C N Coleman. Analysis of prostate and seminal vesicle motion: Implications for treatment planning. *Int. J. Radiat. Oncol. Biol. Phys.*, 34:451–458, 1996.

[8] A Bel, P H Vos, P T R Rodrigus, C L Creutzberg, A G Visser, J C Stroom, and J V Lebesque. High-precision prostate cancer irradiation by clinical application of an off-line patient set-up verification procedure, using portal imaging. *Int. J. Radiat. Oncol. Biol. Phys.*, 35:321–332, 1996.

[9] R Boellaard. *In vivo dosimetry with a liquid-filled electronic portal imaging device*. PhD thesis, Free University, Amsterdam, April 1998.

[10] R Boellaard, M Essers, M van Herk, and B J Mijnheer. New method to obtain the midplane dose using portal in vivo dosimetry. *Int. J. Radiat. Oncol. Biol. Phys.*, 41:465–474, 1998.

[11] R Boellaard, M van Herk, and B J Mijnheer. The dose response relationship of a liquid-filled electronic portal imaging device. *Med. Phys.*, 23:1601–1611, 1996.

[12] R Boellaard, M van Herk, and B J Mijnheer. A convolution model to convert transmission dose images to exit dose distributions. *Med. Phys.*, 24:189–199, 1997.

[13] R Boellaard, M van Herk, H Uiterwaal, and B J Mijnheer. Two-dimensional exit dosimetry using a liquid-filled electronic portal imaging device and a convolution model. *Radiother. Oncol.*, 44:149–159, 1997.

[14] R Boellaard, M van Herk, H Uiterwaal, and B J Mijnheer. First clinical tests using a liquid-filled electronic portal imaging device and a convolution model for the verification of the midplane dose. *Radiother. Oncol.*, 47:303–312, 1998.

[15] T Bortfeld, J Bürkelbach, R Boesecke, and W Schlegel. Methods of image reconstruction from projections applied to conformation radiotherapy. *Phys. Med. Biol.*, 35:1423–1443, 1990.

[16] T R Bortfeld, D L Kahler, T J Waldron, and A L Boyer. X-ray field compensation with multileaf collimators. *Int. J. Radiat. Oncol. Biol. Phys.*, 28:723–730, 1994.

[17] A Brahme. Dosimetric precision requirements in radiation therapy. *Acta Radiol Oncol*, 23:379–391, 1984.

[18] A Brahme. Accuracy requirements and quality assurance of external beam therapy with photons and electrons. *Acta Oncologica*, suppl. nr. 1, Chapter 2:9–15, 1988.

[19] A Brahme. Optimization of stationary and moving beam radiation therapy techniques. *Phys. Med. Biol.*, 12:129–140, 1988.

[20] A Brahme, J E Roos, and I Lax. Solution of an integral equation encountered in rotation therapy. *Phys. Med. Biol.*, 27:1221–1229, 1982.

[21] The British Institute of Radiology, 36 Portland Place, London. *Supplement 25: Central Axis Depth Dose Data for Use in Radiotherapy*, 1996.

[22] C Burman, C S Chui, G Kutcher, S Leibel, M Zelefsky, T LoSasso, S Spirou, Q Wu, J Yang, J Stein, R Mohan, Z Fuks, and C C Ling. Planning, delivery, and quality assurance of intensity-modulated radiotherapy using dynamic multileaf collimator: a strategy for larg-scale implementation for the treatment of carcinoma of the prostate. *Int. J. Radiat. Oncol. Biol. Phys.*, 39:863–873, 1997.

[23] J R Cameron, N Suntharalingam, and G N Kenney. *Thermoluminiscent dosimetry*. University Wisconsin Press, Madison, 1968.

[24] J Chavaudra, G Marinello, AM Brule, and J Nguyen. Practical use of lithium borate in thermoluminescent dosimetry. *J Radiol Electrol Med Nucl*, 57:435–445, 1976.

[25] T Chu, K Lee, and P Dunscombe. A technique for the evaluation of a missing tissue compensator system. *Med. Phys.*, 20:713–716, 1993.

[26] M Ciocca, L Landoni, C Italia, P Montanaro, P Canesi, and R Valdagni. Quality control in the conservative treatment of breast cancer: patient dosimetry using silicon detectors. *Radiother. Oncol.*, 22:304–307, 1991.

[27] D J Convery and M E Rosenbloom. The generation of intensity-modulated fields for conformal radiotherapy by dynamic multileaf collimation. *Phys. Med. Biol.*, 37:1359–1374, 1992.

[28] C L Creutzberg, V G M Althof, M de Hoog, A G Visser, H Huizenga, A Wijnmalen, and P C Levendag. A quality control study of the accuracy of patient positioning in irradiation of pelvic fields. *Int. J. Radiat. Oncol. Biol. Phys.*, 34:697–708, 1996.

[29] C L Creutzberg, V G M Althof, H Huizenga, A G Visser, and P C Levendag. Quality assurance using portal imaging: the accuracy of patient positioning in irradiation of breast cancer. *Int. J. Radiat. Oncol. Biol. Phys.*, 25:529–539, 1993.

[30] C L Creutzberg, A G Visser, P M Z R de Porre, J H Meerwaldt, V G M Althof, and P C Levendag. Accuracy of patient positioning in mantle field irradiation. *Radiother. Oncol.*, 23:257–264, 1992.

[31] J M Crook, Y Raymond, D Salhani, H Yang, and B Esche. Prostate motion during standard radiotherapy as assessed by fiducial markers. *Radiother. Oncol.*, 37:35–42, 1995.

[32] J R Cunningham. Scatter-Air Ratios. *Phys. Med. Biol.*, 17:42–51, 1972.

[33] A J Curtin-Savard and E B Podgorsak. Verification of segmented beam delivery using a commercial electronic portal imaging device. *Med. Phys.*, 26:737–742, 1999.

[34] J C J de Boer, K L Pasma, M Kroonwijk, B J M Heijmen, and A G Visser. In vivo dosimetry with an EPID based on the theraview structure. In *Program and Abstract book 5th International Workshop on Electronic Portal Imaging*, pages 120–121. Conference & Logistics Consultants, Inc. Annapolis, MD, 1998.

[35] J C J de Boer, K L Pasma, M Kroonwijk, B J M Heijmen, and A G Visser. Rapid portal dose measurement with a fluoroscopic epid. *Radiother. Oncol.*, 48 (Suppl. 1):p. S109, Abstract 431, 1998.

[36] W de Neve, F van den Heuvel, M Coghe, D Verellen, M de Beukeleer, A Roelstraete, P de Roover, L Thon, and G Storme. Interactive use of on-line portal imaging in pelvic radiation. *Int. J. Radiat. Oncol. Biol. Phys.*, 25:517–524, 1993.

[37] M L P Dirkx, B J M Heijmen, G A Korevaar, M J H van Os, J C Stroom, P C M Koper, and P C Levendag. Field margin reduction using intensity modulated x-ray beams formed with a multileaf collimator. *Int. J. Radiat. Oncol. Biol. Phys.*, 38:1123–1129, 1997.

[38] M L P Dirkx, B J M Heijmen, and J P C van Santvoort. Leaf trajectory calculation for dynamic multileaf collimation to realize optimized fluence profiles. *Phys. Med. Biol.*, 43:1171–1184, 1998.

[39] M L P Dirkx, M Kroonwijk, J C J de Boer, and B J M Heijmen. Daily dosimetric quality control of the MM50 racetrack microtron using an electronic portal imaging device. *Radiother. Oncol.*, 37:55–60, 1995.

[40] M L P Dirkx, K M van Ingen, M Kroonwijk, and B J M Heijmen. Reproducibility of intensity modulated beams generated with dynamic multileaf collimation (DMLC). *Radiother. Oncol.*, 48:S186, 1998.

[41] A Dutreix. When and how can we improve precision in radiotherapy? *Radiother. Oncol.*, 2:275–292, 1984.

[42] M Essers. *In vivo dosimetry in radiotherapy, Development, use and evaluation of accurate patient dose verification methods*. PhD thesis, Free University, Amsterdam, May 1996.

[43] M Essers, R Boellaard, M van Herk, J H Lanson, and B J Mijnheer. Transmission dosimetry with a liquid-filled electronic portal imaging device. *Int. J. Radiat. Oncol. Biol. Phys.*, 34:931–941, 1996.

[44] M Essers, B R Hoogervorst, M van Herk, J H Lanson, and B J Mijnheer. Dosimetric characteristics of a liquid-filled electronic portal imaging device. *Int. J. Radiat. Oncol. Biol. Phys.*, 33:1265–1272, 1995.

[45] M Essers, R Keus, J H Lanson, and B J Mijnheer. Dosimetric control of conformal treatment of parotid gland tumors. *Radiother. Oncol.*, 32:154–162, 1994.

[46] M Essers, J H Lanson, G Leunens, T Schnabel, and B J Mijnheer. The accuracy of CT-based inhomogeneity corrections and in vivo dosimetry for the treatment of lung cancer. *Radiother. Oncol.*, 37:199–208, 1995.

[47] M Essers, J H Lanson, and B J Mijnheer. In vivo dosimetry during conformal therapy of prostatic cancer. *Radiother. Oncol.*, 29:271–279, 1993.

[48] M Essers and B J Mijnheer. In vivo dosimetry during external photon beam radiotherapy. *Int. J. Radiat. Oncol. Biol. Phys.*, 43:245–259, 1999.

[49] P M Evans, E M Donovan, N Fenton, V N Hansen, I Moore, M Partridge, S Reise, B Suter, J R Symonds-Tayler, and J R Yarnold. Practical implementation of compensators in breast radiotherapy. *Radiother. Oncol.*, 49:255–265, 1998.

[50] P M Evans, V N Hansen, W P M Mayles, W Swindell, M Torr, and J R Yarnold. Design of compensators for breast radiotherapy using electronic portal imaging. *Radiother. Oncol.*, 37:43–54, 1995.

[51] P M Evans, V N Hansen, W Swindell, M Torr, W P M Mayles, A J Neal, S Brown, and J R Yarnold. The use of a portal imaging system to design tissue compensators for radiotherapy of the breast. In *Proceedings of the XIth ICCR (International Congress on the use of Computers in Radiation Therapy)*. edited by A R Hounsell, J M Wilkinson and P C Williams (Handley, Stockport, UK, 1994), pp. 118-119.

[52] C Fiorino, A del Vecchio, G M Cattaneo, M Fusca, B Longobardi, P Signorotto, and R Calandrino. Exit dose measurements by portal film dosimetry. *Radiother. Oncol.*, 29:336–340, 1993.

[53] Gocht. Therapeutische Verwendung der Roentgenstrahlen. *Fortschr. Roentgenstr.*, 1:14–22, 1897.

[54] M Goitein. Nonstandard deviations. *Med. Phys.*, 10:709–711, 1983.

[55] M Goossens, F Mittelbach, and A Samarin. *The LaTeX companion*. Addison-Wesley Longman, Inc., 1997.

[56] E Grusell and G Rikner. Evaluation of temperature effects in p-type silicon detectors. *Phys. Med. Biol.*, 31:527–534, 1986.

[57] H Guan and Y Zhu. Feasibility of megavoltage portal CT using an electronic portal imaging device (EPID) and a multi-level scheme algebraic reconstruction technique (MLS-ART). *Phys. Med. Biol.*, 43:2925–2937, 1998.

[58] V N Hansen. *Electronic Portal Imaging for Dosimetric Purposes*. PhD thesis, University of London, 1997.

[59] V N Hansen, P M Evans, and W Swindell. Transit dosimetry - computer generated dose images for verification. In *Proceedings of the XIth ICCR (International Congress on the use of Computers in Radiation Therapy)*. edited by A R Hounsell, J M Wilkinson and P C Williams (Handley, Stockport, UK, 1994), pp. 116-117.

[60] V N Hansen, P M Evans, and W Swindell. The application of transit dosimetry to precision radiotherapy. *Med. Phys.*, 23:713–721, 1996.

[61] B J M Heijmen, K L Pasma, M Kroonwijk, V G M Althof, J C J de Boer, A G Visser, and H Huizenga. Portal dose measurement in radiotherapy using an electronic portal imaging device (EPID). *Phys. Med. Biol.*, 40:1943–1955, 1995.

[62] B J M Heijmen, K L Pasma, M Kroonwijk, and A G Visser. Voorspelling en meting van transmissie-dosisverdelingen achter bestraalde patiënten. *Klinische Fysica*, 2:29–32, 1997.

[63] B J M Heijmen, K L Pasma, M Kroonwijk, A G Visser, and H Huizenga. Prediction of portal dose images for *in vivo* dosimetry in radiotherapy. *Med. Phys.*, 22:992, 1995.

[64] B J M Heijmen, P R M Storchi, and J B van de Kamer. A method for prediction of portal dose images. In *Proceedings of the XIth ICCR (International Congress on the use of Computers in Radiation Therapy)*. edited by A R Hounsell, J M Wilkinson and P C Williams (Handley, Stockport, UK, 1994), pp. 112-113.

[65] B J M Heijmen, J C Stroom, H Huizenga, and A G Visser. Application of a fluoroscopic portal imaging system with a CCD camera for accurate in-vivo dosimetry. *Med. Phys.*, 20:870, 1993.

[66] B J M Heijmen, A G Visser, and H Huizenga. In-vivo dose measurements using an electronic portal imaging device: a feasibility study. *Radiother. Oncol.*, 24 (supplement):S25, 1992.

[67] B M Hesse, L Spies, and B A Groh. Tomotherapeutic portal imaging for radiation treatment verification. *Phys. Med. Biol.*, 43:3607–3616, 1998.

[68] S Heukelom, J H Lanson, and B J Mijnheer. Comparison of entrance and exit dose measurements using ionization chambers and silicon diodes. *Phys. Med. Biol.*, 36:47–59, 1991.

[69] S Heukelom, J H Lanson, and B J Mijnheer. Quality assurance of the simultaneous boost technique for prostatic cancer: dosimetric aspects. *Radiother. Oncol.*, 30:74–82, 1994.

[70] S Heukelom, J H Lanson, G van Tienhoven, and B J Mijnheer. In-vivo dosimetry during tangential breast treatment. *Radiother. Oncol.*, 22:269–279, 1991.

[71] D Huyskens, J Van Dam, and A Dutreix. Midplane dose determination using in vivo dose measurements in combination with portal imaging. *Phys. Med. Biol.*, 39:1089–1101, 1994.

[72] ICRU Report 24. Determination of absorber dose in a patient irradiated by means of X or gamma rays in radiotherapy procedures. Technical report, International Commission on Radiotherapy Units and Measurements, 1976.

[73] ICRU Report 50. Prescribing, recording and reporting photon beam therapy. Technical report, International Commission on Radiotherapy Units and Measurements, Bethesda, 1993.

[74] D A Jaffray, J J Battista, A Fenster, and P Munro. X-ray scatter in megavoltage transmission radiography: Physical characteristics and influence on image quality. *Med. Phys.*, 21:45–60, 1994.

[75] P Källman, B K Lind, and A Brahme. An algorithm for maximizing the probability of complication-free tumour control in radiation therapy. *Phys. Med. Biol.*, 37:871–890, 1992.

[76] P Källman, B K Lind, A Eklöf, and A Brahme. Shaping of arbitrary dose distributions by dynamic multileaf collimation. *Phys. Med. Biol.*, 33:1291–1300, 1988.

[77] H Keller, M Fix, and P Ruegsegger. Calibration of a portal imaging device for high-precision dosimetry: a Monte Carlo study. *Med. Phys.*, 25:1891–1902, 1998.

[78] F M Khan. *The Physics of Radiation Therapy*, pages 239–245. Williams & Wilkins, 428 East Preston Street, Baltimore, USA, 1984.

[79] F M Khan. *The Physics of Radiation Therapy*, pages 420–423. Williams & Wilkins, 428 East Preston Street, Baltimore, USA, 1984.

[80] M C Kirby and P C Williams. Measurement possibilities using an electronic portal imaging device. *Radiother. Oncol.*, 29:237–243, 1993.

[81] M C Kirby and P C Williams. The use of an electronic portal imaging device for exit dosimetry and quality control measurements. *Int. J. Radiat. Oncol. Biol. Phys.*, 31:593–603, 1995.

[82] T Knöös, L Ahlgren, and M Nilsson. Comparison of measured and calculated absorbed doses from tangential irradiation of the breast. *Radiother. Oncol.*, 7:81–88, 1986.

[83] P C M Koper, W L J v Putten, J C Stroom, G A Korevaar, B J M Heijmen, A J Wijnmaalen, P P Jansen, P E J Hanssens, C Griep, S Krol, M J Samson, and P C Levendag. Acute morbidity reduction using 3DCRT for prostate carcinoma: A randomised phase III study. *Int. J. Radiat. Oncol. Biol. Phys.*, 39(suppl.):191, 1997.

[84] M Kroonwijk, K L Pasma, S Quint, P C M Koper, A G Visser, and B J M Heijmen. In vivo dosimetry for prostate cancer patients using an electronic portal imaging device (EPID); detection of internal organ motion. *Radiother. Oncol.*, 49:125–132, 1998.

[85] M Kroonwijk, K L Pasma, S Quint, A G Visser, and B J M Heijmen. Development and clinical implementation of in-vivo dosimetry using an electronic portal imaging device. In *Proceedings of the XIIth ICCR (International Congress on the use of Computers in Radiation Therapy)*. edited by D D Leavitt and G Starkschall (Medical Physics Publishing, Madison, WI, 1997), pp. 276-278.

[86] T Lahtinen, H Puurunen, P Simonen, A Pekkarinen, and A Väänänen. In vivo dose measurements with new linear accelerators. In *Dosimetry in radiotherapy*, pages 259–273. International Atomic Energy Agency, Vienna, 1988.

[87] J V Lebesque, A M Bruce, A P G Kroes, A Touw, T Shouman, and M van Herk. Variation in volumes, dose-volume histograms and estimated normal tissue complication probabilities of rectum and bladder during conformal radiotherapy of T3 prostate cancer. *Int. J. Radiat. Oncol. Biol. Phys.*, 33:1109–1119, 1995.

[88] P C Lee, J M Sawicka, and G P Glasgow. Patient dosimetry quality assurance program with a commercial diode system. *Int. J. Radiat. Oncol. Biol. Phys.*, 29:1175–1182, 1994.

[89] J Leong. Use of digital fluoroscopy as on-line verification device in radiation therapy. *Phys. Med. Biol.*, 31:985–992, 1986.

[90] G Leunens, J van Dam, A Dutreix, and E van der Schueren. Quality assurance in radiotherapy by in vivo dosimetry. 1. Entrance dose measurements, a reliable procedure. *Radiother. Oncol.*, 17:141–151, 1990.

[91] G Leunens, J van Dam, A Dutreix, and E van der Schueren. Quality assurance in radiotherapy by in vivo dosimetry. 2. Determination of the target absorbed dose. *Radiother. Oncol.*, 19:73–87, 1990.

[92] G Leunens, J Verstraete, J van Dam, A Dutreix, and E van der Schueren. In vivo dosimetry for tangential breast irradiation: role of the equipment in the accuracy of dose delivery. *Radiother. Oncol.*, 22:285–289, 1991.

[93] C C Ling, C Burman, C S Chui, G J Kutcher, S A Leibel, T LoSasso, R Mohan, T Bortfeld, L Reinstein, S Spirou, X H Wang, Q Wu, M Zelefsky, and Z Fuks. Conformal radiation treatment of prostate cancer using inversely-planned intensity-modulated photon beams produced with dynamic multileaf collimation. *Int. J. Radiat. Oncol. Biol. Phys.*, 35:721–730, 1996.

[94] T LoSasso, C S Chui, and C C Ling. Physical and dosimetric aspects of a multileaf collimation system used in the dynamic mode for implementing intensity modulated radiotherapy. *Med. Phys.*, 25:1919–1927, 1998.

[95] D A Low, Z Li, and E E Klein. Verification of milled two-dimensional photon compensating filters using an electronic portal imaging device. *Med. Phys.*, 23:929–938, 1996.

[96] L Ma, P B Geis, and A L Boyer. Quality assurance for dynamic multileaf collimator modulated fields using a fast beam imaging system. *Med. Phys.*, 24:1213–1220, 1997.

[97] T R Mackie, T Holmes, S Swerdloff, P Reckwerdt, J O Deasy, J Yang, B Paliwal, and T Kinsella. Tomotherapy: A new concept for the delivery of dynamic conformal radiotherapy. *Med. Phys.*, 20:1709–1719, 1993.

[98] T R McNutt, T R Mackie, P Reckwerdt, and B R Paliwal. Modeling dose distributions from portal dose images using the convolution/superposition method. *Med. Phys.*, 23:1381–1392, 1996.

[99] T R McNutt, T R Mackie, P Reckwerdt, N Papanikolaou, and B R Paliwal. Calculation of portal dose using the convolution/superposition method. *Med. Phys.*, 23:527–535, 1996.

[100] Y Mejaddem, I Lax, and A K Shamsuddin. Procedure for accurate fabrication of tissue compensators with high-density material. *Phys. Med. Biol.*, 42:415–421, 1997.

[101] E Melian, G J Kutcher, S A Leibel, M Zelefsky, B Baldwin, and Z Fuks. Variation in prostate position: quantification and implications for three-dimensional conformal treatment planning. *Int. J. Radiat. Oncol. Biol. Phys.*, 27:137, 1993.

[102] E Melian, G S Mageras, Z Fuks, S A Leibel, A Niehaus, H Lorant, M Zelefsky, B Baldwin, and G J Kutcher. Variation in prostate position quantification and implications for three-dimensional conformal treatment planning. *Int. J. Radiat. Oncol. Biol. Phys.*, 38:73–81, 1997.

[103] S Midgley, R M Millar, and J Dudson. A feasibility study for megavoltage cone beam CT using a commercial EPID. *Phys. Med. Biol.*, 43:155–169, 1998.

[104] B J Mijnheer, J J Battermann, and A Wambersie. What degree of accuracy is required and can be achieved in photon and neutron therapy? *Radiother Oncol*, 8:237–252, 1987.

[105] C Mitine, G Leunens, J Verstraete, N Blanckaert, J Van Dam, A Dutreix, and E van der Schueren. Is it necessary to repeat quality control procedures for head and neck patients? *Radiother. Oncol.*, 21:201–210, 1991.

[106] E J Morton, W Swindell, D G Lewis, and P M Evans. A linear array, scintillation crystal-photodiode detector for megavoltage imaging. *Med. Phys.*, 18:681–691, 1991.

[107] M A Mosleh-Shirazi, P M Evans, W Swindell, S Webb, and M Partridge. A cone-beam megavoltage CT scanner for treatment verification in conformal radiotherapy. *Radiother. Oncol.*, 48:319–328, 1998.

[108] P Munro and D C Bouius. X-ray quantum limited portal imaging using amorphous silicon flat-panel arrays. *Med. Phys.*, 25:689–702, 1998.

[109] B Nilsson, B I Rudén, and B Sorcini. Characteristics of silicon diodes as patient dosemeters in external radiation therapy. *Radiother. Oncol.*, 11:279–288, 1988.

[110] A Noel, P Aletti, P Bey, and L Malissard. Detection of errors in individual patients in radiotherapy by systematic in vivo dosimetry. *Radiother. Oncol.*, 34:144–151, 1995.

[111] H Parsaei, E el Khatib, and R Rajapakshe. The use of an electronic portal imaging system to measure portal dose and portal dose profiles. *Med. Phys.*, 25:1903–1909, 1998.

[112] M Partridge, P M Evans, A Mosleh-Shirazi, and D Convery. Independent verification using portal imaging of intensity-modulated beam delivery by the dynamic MLC technique. *Med. Phys.*, 25:1872–1879, 1998.

[113] K L Pasma, M L P Dirkx, M Kroonwijk, A G Visser, and B J M Heijmen. Dosimetric verification of intensity modulated beams produced with dynamic multileaf collimation using an electronic portal imaging device. *Med. Phys.*, 1999. submitted.

[114] K L Pasma, M L P Dirkx, M Kroonwijk, A G Visser, and B J M Heijmen. Dosimetric verification of intensity modulated fields produced with dynamic multileaf collimation using an Electronic Portal Imaging Device (EPID). *Radiother. Oncol.*, 51 (Supplement 1):S33, 1999.

[115] K L Pasma, B J M Heijmen, M Kroonwijk, and A G Visser. Portal dose image (PDI) prediction for dosimetric treatment verification in radiotherapy I: An algorithm for open beams. *Med. Phys.*, 25:830–840, 1998.

[116] K L Pasma, M Kroonwijk, J C J de Boer, A G Visser, and B J M Heijmen. Accurate portal dose measurement with a fluoroscopic electronic portal imaging device (EPID) for open and wedged beams and for dynamic multileaf collimation. *Phys. Med. Biol.*, 43:2047–2060, 1998.

[117] K L Pasma, M Kroonwijk, B J M Heijmen, H Huizenga, and A G Visser. Prediction of transmissions of open and wedged photon beams through patients for in-vivo dosimetry with an EPID. In *Program and Abstract book 4th International Workshop on Electronic Portal Imaging*, page 45. Medical Faculty, Free University, Amsterdam, The Netherlands, 1996.

[118] K L Pasma, M Kroonwijk, S Quint, A G Visser, and B J M Heijmen. Integrated patient positioning verification and in vivo dosimetry with an EPID: first clinical data. *Radiother. Oncol.*, 40:S88, 1996.

[119] K L Pasma, M Kroonwijk, S Quint, A G Visser, and B J M Heijmen. Clinical application of in-vivo dosimetry with a fluoroscopic EPID for prostate cancer patients (N=115). In *Program and Abstract book 5th International Workshop on Electronic Portal Imaging*, pages 118–119. Conference & Logistics Consultants, Inc. Annapolis, MD, 1998.

[120] K L Pasma, M Kroonwijk, S Quint, A G Visser, and B J M Heijmen. Derivation of delivered patient doses from EPID images for 100 prostate cancer patients. *Radiother. Oncol.*, 48 (Suppl. 1):p. S205, Abstract 809, 1998.

[121] K L Pasma, M Kroonwijk, S Quint, A G Visser, and B J M Heijmen. Derivation of patient dose from portal dose images measured with an EPID. *Med. Phys.*, 25:A162, 1998.

[122] K L Pasma, M Kroonwijk, S Quint, A G Visser, and B J M Heijmen. Transit dosimetry with an electronic portal imaging device (EPID) for 115 prostate cancer patients. *Int. J. Radiat. Oncol. Biol. Phys.*, 1999. submitted.

[123] K L Pasma, M Kroonwijk, E B van Dieren, A G Visser, and B J M Heijmen. Simple and accurate verification of compensator thicknesses using an Electronic Portal Imaging Device (EPID). *Radiother. Oncol.*, 51 (Supplement 1):S25, 1999.

[124] K L Pasma, M Kroonwijk, E B van Dieren, A G Visser, and B J M Heijmen. Verification of compensator thicknesses using a fluoroscopic electronic portal imaging device. *Med. Phys.*, 1999. in press.

[125] K L Pasma, M Kroonwijk, A G Visser, and B J M Heijmen. Portal dose measurements with a video-based electronic portal imaging device using a deconvolution algorithm. In *Proceedings of the XIIth ICCR (International Congress on the use of Computers in Radiation Therapy)*. edited by D D Leavitt and G Starkschall (Medical Physics Publishing, Madison, WI, 1997), pp. 282-284.

[126] K L Pasma, M Kroonwijk, A G Visser, and B J M Heijmen. Prediction of transmission of wedged photon beams through patients for in vivo dosimetry with an EPID. *Radiother. Oncol.*, 40:S89, 1996.

[127] K L Pasma, M Kroonwijk, A G Visser, and B J M Heijmen. Accurate portal dose measurements with a video-based electronic portal imaging device. In *Abstract book of the world congress on medical physics and biomedical engineering*, volume 35, part 2, page 1081, Nice, September 1997.

[128] G Rikner. *Silicon diodes as detectors in relative dosimetry of photon, electron and proton radiation fields*. PhD thesis, Uppsala University, Sweden, 1983.

[129] G Rikner and E Grusell. General specifications for silicon semiconductors for use in radiation dosimetry. *Phys. Med. Biol.*, 32:1109–1117, 1987.

[130] A Rizzotti, C Compri, and G F Garusi. Dose evaluation to patients irradiated by ^{60}Co beams, by means of direct measurement on the incident and on the exit surfaces. *Radiother. Oncol.*, 3:279–283, 1985.

[131] D M Roback and B J Gerbi. Evaluation of electronic portal imaging device for missing tissue compensator design and verification. *Med. Phys.*, 22:2029–2034, 1995.

[132] J C Roeske, J D Forman, C F Mesina, T He, C A Pelizzari, E Fontenla, S Vijayakumar, and G T Y Chen. Evaluation of changes in the size and location of the prostate, seminal vesicles, bladder, and rectum during a course of external beam radiation therapy. *Int. J. Radiat. Oncol. Biol. Phys.*, 33:1321–1329, 1995.

[133] W C Röntgen. Ueber eine neue Art von Strahlen. *Annalen der Physik und Chemie*. Neue Folge, Band 64, No 1, 1895.

[134] B -I Rudén. Evaluation of the clinical use of TLD. *Acta Radiol. Ther. Phys. Biol.*, 15:447–464, 1976.

[135] R W Schafer, R M Mersereau, and M A Richards. Constrained Iterative Restoration Algorithms. In *Proceedings of the IEEE*, volume 69, pages 432–450, 1981.

[136] A Sen, E I Parsai, S W McNeeley, and K M Ayyangar. Quantitative assessment of beam perturbations caused by silicon diodes used for in vivo dosimetry. *Int. J. Radiat. Oncol. Biol. Phys.*, 36:205–211, 1996.

[137] G W Sherouse, K Novins, and E L Chaney. Computation of digitally reconstructed radiographs for use in radiotherapy treatment design. *Med. Phys.*, 18:651–658, 1990.

[138] S Södertröm and A Brahme. Optimization of the dose delivery in a few field techniques using radiobiological objective functions. *Med. Phys.*, 20:1201–1209, 1993.

[139] S V Spirou and C S Chui. Generation of arbitrary intensity profiles by dynamic jaws or multileaf collimators. *Med. Phys.*, 21:1031–1041, 1994.

[140] J Stein, T Bortfeld, B Dörschel, and W Schlegel. Dynamic X-ray compensation for conformal radiotherapy by means of multi-leaf collimation. *Int. J. Radiat. Oncol. Biol. Phys.*, 32:163–173, 1994.

[141] P Storchi and E Woudstra. Calculation models for determining the absorbed dose in water phantoms in off-axis planes of rectangular fields of open and wedged photon beams. *Phys. Med. Biol.*, 40:511–527, 1995.

[142] P Storchi and E Woudstra. Calculation of the absorbed dose distribution due to irregularly shaped photon beams using pencil beam kernels derived from basic input data. *Phys. Med. Biol.*, 41:637–656, 1996.

[143] P Storchi, E Woudstra, P Verlinde, K Johansson, and A Samuelsson. Calculation of the absorbed dose distributions from dynamic wedges. *Phys. Med. Biol.*, 43:1497–1506, 1998.

[144] J C Stroom, B J M Heijmen, A G Visser, and H Huizenga. In vivo dose measurements using the SRI-100 imaging device: first clinical experience. In *Book of abstracts Second Biennial ESTRO Meeting on Physics in Clinical Radiotherapy*, page 35, 1993.

[145] J C Stroom, G A Korevaar, P C M Koper, A G Visser, and B J M Heijmen. Multiple 2-Dimensional versus 3-Dimensional PTV definition in treatment planning for conformal radiotherapy. *Radiother. Oncol.*, 47:297–302, 1998.

[146] J C Stroom, M Kroonwijk, K L Pasma, P C M Koper, E B van Dieren, P Levendag, and B J M Heijmen. Detection of internal prostate movement using portal images. *Radiother. Oncol.*, 48 (Suppl. 1):S108, abstract 429, 1998.

[147] J C Stroom and P R M Storchi. Automatic calculation of three-dimensional margins around treatment volumes in radiotherapy planning. *Phys. Med. Biol.*, 42:745–755, 1997.

[148] R Svensson, P Källman, and A Brahme. An analytical solution for the dynamic control of multileaf collimators. *Phys. Med. Biol.*, 39:37–61, 1994.

[149] W Swindell. Transit dosimetry. *Brit J. Radiol.*, 66:1077, 1993.

[150] W Swindell and P M Evans. Scattered radiation in portal images: A Monte Carlo simulation and a simple physical model. *Med. Phys.*, 23:1–11, 1995.

[151] J R Symonds-Tayler, M Partridge, and P M Evans. An electronic portal imaging device for transit dosimetry. *Phys. Med. Biol.*, 42:2273–2283, 1997.

[152] R K Ten Haken, J D Forman, D K Heimburger, A Gerhardsson, D L McShan, C Perez-Tamayo, S L Schoeppel, and A S Lichter. Treatment planning issues related to prostate movement in response to differential filling of the rectum and bladder. *Int. J. Radiat. Oncol. Biol. Phys.*, 20:1317–1324, 1991.

[153] J Troccaz, Y Menguy, M Bolla, P Cinquin, P Vassal, N Laieb, L Desbat, A Dusserre, and S Dal Soglio. Conformal external radiotherapy of prostatic carcinoma: requirements and experimental results. *Radiother. Oncol.*, 29:176–183, 1993.

[154] N A van Bree, L J van Battum, H Huizenga, and B J Mijnheer. Three-dimensional dose distribution of tangential breast treatment: a national dosimetry intercomparison. *Radiother. Oncol.*, 22:252–260, 1991.

[155] J Van Dam, C Vaerman, N Blanckaert, G Leunens, A Dutreix, and E van der Schueren. Are port films reliable for in vivo exit dose measurements? *Radiother. Oncol.*, 25:67–72, 1992.

[156] J van de Steene, F van den Heuvel, A Bel, D Verellen, J fe Mey, M Noppen, M de Beukeleer, and G Storme. Electronic portal imaging with on-line correction of setup error in thoracic irradiation: clinical evaluation. *Int. J. Radiat. Oncol. Biol. Phys.*, 40:967–976, 1998.

[157] E B van Dieren, P J C M Nowak, O Wijers, J R van Sörnsen de Koste, B J M Heijmen, and P C Levendag. Beam intensity modulation for treatment of the neck. In *Abstract book of the world congress on medical physics and biomedical engineering*, volume 35, part 2, page 921, Nice, September 1997.

[158] M van Herk, B Boellaard, M Brugmans, and A van Dalen. Feasibility of the portalvision system for verification of dynamic therapy. In *Program and Abstract book 4th International Workshop on Electronic Portal Imaging*, page 53. Medical Faculty, Free University, Amsterdam, The Netherlands, 1996.

[159] M van Herk, A Bruce, A P G Kroes, T Shouman, A Touw, and J V Lebesque. Quantification of organ motion during conformal radiotherapy of the prostate by three dimensional image registration. *Int. J. Radiat. Oncol. Biol. Phys.*, 33:1311–1320, 1995.

[160] M van Herk and H Meertens. A matrix ionization chamber for on-line patient setup verification during radiotherapy. *Radiother. Oncol.*, 11:369–378, 1988.

[161] J P C van Santvoort, D Binnekamp, B J M Heijmen, and P C Levendag. Granulate of stainless steel as compensator material. *Radiother. Oncol.*, 34:78–80, 1995.

[162] J P C van Santvoort and B J M Heijmen. Dynamic multileaf collimation without 'tongue-and-groove' underdosage effects. *Phys. Med. Biol.*, 41:2091–2105, 1996.

[163] E Vigneault, J Pouliot, J Laverdière, J Roy, and M Dorion. Electronic portal imaging device detection of radio-opaque markers for the evaluation of prostate position during megavoltage irradiation: A clinical study. *Int. J. Radiat. Oncol. Biol. Phys.*, 37:205–212, 1997.

[164] A G Visser, H Huizenga, V G M Althof, and B N Swanenburg. Performance of a prototype fluoroscopic radiotherapy imaging system. *Int. J. Radiat. Oncol. Biol. Phys.*, 18:43–50, 1990.

[165] X Wang, S Spirou, T LoSasso, J Stein, C S Chui, and R Mohan. Dosimetric verification of intensity-modulated fields. *Med. Phys.*, 23:317–327, 1996.

[166] S Webb. Optimization of conformal radiotherapy dose distributions by simulated annealing. *Phys. Med. Biol.*, 34:1349–1370, 1989.

[167] S Webb. Optimization by simulated annealing of three-dimensional, conformal treatment planning for radiation fields defined by a multileaf collimator: II. Inclusion of two-dimensional modulation of the x-ray intensity. *Phys. Med. Biol.*, 37:1689–1704, 1992.

[168] S Webb. Optimizing the planning of intensity-modulated radiotherapy. *Phys. Med. Biol.*, 39:2229–2246, 1994.

[169] S Webb. *The physics of conformal radiotherapy*. IOP Publishing Ltd, London, 1997.

[170] S Webb, T Bortfeld, J Stein, and D Convery. The effect of stair-step leaf transmission on the 'tongue-and-groove problem' in dynamic radiotherapy with a multileaf collimator. *Phys. Med. Biol.*, 42:595–602, 1997.

[171] J W Wong, A Y Cheng, W R Binns, J W Epstein, J Klarmann, and C A Perez. Development of a second-generation fiber-optic on-line image verification system. *Int. J. Radiat. Oncol. Biol. Phys.*, 26:311–320, 1993.

[172] J W Wong, E D Slessinger, R E Hermes, C J Offutt, T Roy, and M W Vannier. Portal dose images I: Quantitative treatment plan verification. *Int. J. Radiat. Oncol. Biol. Phys.*, 18:1455–1463, 1990.

[173] F-F Yin, M C Schell, and P Rubin. Input/output characteristics of a matrix ion-chamber electronic portal imaging device. *Med. Phys.*, 21:1447–1454, 1994.

[174] F-F Yin, M C Schell, and P Rubin. A technique of automating compensator design for lung inhomogeneity correction using an electronic portal imaging device. *Med. Phys.*, 21:1729–1732, 1994.

[175] X Ying, L Y Geer, and J W Wong. Portal dose images II: Patient dose estimation. *Int. J. Radiat. Oncol. Biol. Phys.*, 18:1465–1475, 1990.

[176] Y Zhu, X-Q Jiang, and J van Dyk. Portal dosimetry using a liquid ion chamber matrix: Dose response studies. *Med. Phys.*, 22:1101–1106, 1995.

Production notes

This book was typeset by the author on a pentium PC using the Y&Y TeX system. The typeface used for the main text is MathTime 1.1 10pt designed by Michael D. Spivak. All references to figures, sections and pages were generated by LaTeX using the basis commands: `\label`, `\ref` and `\pageref`. The reference list was prepared with BibTeX, using a bibliography data base (.bib file) and the `\cite`-commando.

Most figures were generated with Harvard Graphics 3.0 and exported to PostScript files (∗.ps) using a Lexmark Optra C PS2 printer driver. GSview was used to convert the resulting files to encapsulated PostScript files (∗.eps). Some figures (e.g. the histograms in chapter 6) were generated using Microsoft Excel. Since Microsoft doesn't support exporting to PostScript, this required a copy and paste special (picture) procedure of each figure to Word97, afterwhich each figure was printed using the WinSlide95 printer driver. The resulting PostScript file was then converted to encapsulated PostScript using GSView. The color figure (figure 5.3) was generated with an IDL 5.1 application written by Marco Kroonwijk. The shaded surface plots of the compensators (figures 7.3 and 7.6) were also produced with IDL.

Several LaTeX 2_ε packages were used, the most important ones were: `dvips`, `citesort`, `subfigure`, `afterpage`, `caption2`, `xspace`, `fancyhea`, `enumerate` and `ulem`. All these are available on the internet (`www.dante.de/cgi-bin/ctan-index`).

Chapters 2,3,4 and 5 were originally typeset using WordPerfect 5.1 and later converted into LaTeX 2_ε using a converter provided in the 4AllTeX distribution of the Dutch TeX user group. The final version of this thesis was produced with a single LaTeX job. The original positioning of some of the figures by LaTeX had to be overruled to prevent drifting of figures to the end of the chapters, but the rest of the layout was left to LaTeX. The resulting camera-ready PostScript file was only 15 Mbyte in size. A detailed overview of the visible and not-so-visible beauties of LaTeX can be found in "The LaTeX Companion", by Goossens, Mittelbach, and Samarin [55].